

# Proračun opterećenja vjetra na plutajući pučinski objekt

---

Jovan, Ivica

Master's thesis / Diplomski rad

2018

*Degree Grantor / Ustanova koja je dodijelila akademski / stručni stupanj:* **University of Zagreb, Faculty of Mechanical Engineering and Naval Architecture / Sveučilište u Zagrebu, Fakultet strojarstva i brodogradnje**

*Permanent link / Trajna poveznica:* <https://urn.nsk.hr/urn:nbn:hr:235:496991>

*Rights / Prava:* [In copyright](#)/[Zaštićeno autorskim pravom.](#)

*Download date / Datum preuzimanja:* **2025-04-01**

*Repository / Repozitorij:*

[Repository of Faculty of Mechanical Engineering and Naval Architecture University of Zagreb](#)



UNIVERSITY OF ZAGREB  
Faculty of Mechanical Engineering and Naval Architecture

# **MASTER'S THESIS**

**Ivica Jovan**

Zagreb, 2018

UNIVERSITY OF ZAGREB  
Faculty of Mechanical Engineering and Naval Architecture

**WIND LOAD COMPUTATIONS OF A OFFSHORE  
FLOATING OBJECT**

Supervisor:  
Prof. Hrvoje Jasak, PhD

Student:  
Ivica Jovan

Zagreb, 2018

I hereby declare that this thesis is entirely the result of my own work except where otherwise indicated. I have fully cited all used sources and I have only used the ones given in the list of references

I would like to express my sincere gratitude to Professor Hrvoje Jasak for allowing me to pursue and accomplish this thesis.

I am truly thankful to Inno Gatin for his time, patience and valuable advice. Without his knowledge and experience this thesis would not be possible.

I would also like to thank my friends and colleagues for all the support and encouragement during the work on the thesis. Special thanks goes to my colleagues from the 8th floor for the positive work environment with numerous discussions and plenty of fun times. It was my pleasure to be a part of the 8th floor CFD group.

Finally I would like to thank to my family for all the support they have provided me over the years. Thank you for your patience and for being of such great support.

Thank you all,  
Ivica Jovan



SVEUČILIŠTE U ZAGREBU  
FAKULTET STROJARSTVA I BRODOGRADNJE



Središnje povjerenstvo za završne i diplomske ispite  
Povjerenstvo za diplomske ispite studija strojarstva za smjerove:  
procesno-energetski, konstrukcijski, brodstrojarski i inženjersko modeliranje i računalne simulacije

Sveučilište u Zagrebu	
Fakultet strojarstva i brodogradnje	
Datum 17-01-2018	Prilog
Klasa: 602-04/18-6/3	
Ur. broj: 15-1703-18-6	

## DIPLOMSKI ZADATAK

Student: **Ivica Jovan**

Mat. br.: 0035190837

Naslov rada na hrvatskom jeziku: **Proračuni opterećenja vjetra na plutajući pučinski objekt**

Naslov rada na engleskom jeziku: **Wind Load Computations of a Offshore Floating Object**

Opis zadatka:

Large floating offshore objects encountered in the oil and gas industry endure severe wind loads during hurricanes. It is necessary to assess these loads in order to determine the dynamic response of the floating object. Given the highly nonlinear nature of turbulent air flow around the intricate geometry of a offshore object, Computational Fluid Dynamics (CFD) is the only method available for predicting the wind loads accurately and without the need for any experimental measurements. In this study, the candidate should conduct the simulations of wind loads for a realistic floating offshore structure using the CFD software foam-extend.

The candidate shall perform the following tasks within this project:

- perform a literature survey regarding wind load calculation using CFD,
- investigate different turbulence modelling techniques for assessing the wind loads accurately,
- define a realistic wind velocity profile in the atmospheric boundary layer and compare to wind tunnel measurements,
- conduct a validation study by comparing the results to experimental measurements reported in SNAME OC-8.

The Thesis shall list the bibliography and any assistance received during this study.

Zadatak zadan:

16. studenog 2017

Datum predaje rada:

18. siječnja 2017.

Predviđeni datum obrane:

24., 25. i 26. siječnja 2018.

Zadatak zadao:

Prof. dr. sc. Hrvoje Jasak

Predsjednica Povjerenstva:

Prof. dr. sc. Tanja Jurčević Lulić

# Table of Contents

<b>List of Figures</b>	<b>IV</b>
<b>List of Tables</b>	<b>V</b>
<b>Nomenclature</b>	<b>VI</b>
<b>Abbreviations</b>	<b>VII</b>
<b>Abstract</b>	<b>VIII</b>
<b>Sažetak</b>	<b>IX</b>
<b>Prošireni sažetak (Extended Abstract in Croatian)</b>	<b>XXIV</b>
<b>1 Introduction</b>	<b>1</b>
<b>2 Mathematical model</b>	<b>3</b>
2.1 Introduction . . . . .	3
2.2 Governing equations of fluid flow . . . . .	3
2.3 Turbulence modelling . . . . .	4
2.3.1 Reynolds Averaged Navier-Stokes Equations . . . . .	5
2.3.2 $k - \omega$ SST Turbulence model . . . . .	7
2.3.3 Large Eddy Simulation . . . . .	9
2.4 Boundary Conditions . . . . .	10
2.5 Closure . . . . .	10
<b>3 Influence of wind on engineering structures</b>	<b>11</b>
3.1 Introduction . . . . .	11
3.2 Atmospheric Boundary Layer (ABL) . . . . .	11
3.3 Distribution of pressure caused by wind load . . . . .	13
3.4 Closure . . . . .	14
<b>4 Geometry and Numerical Domain</b>	<b>15</b>
4.1 Introduction . . . . .	15
4.2 Houston Offshore Engineering (HOE) Paired column (PC)-Semi Submersible Platform Models . . . . .	15
4.3 Computational mesh . . . . .	17
4.4 Closure . . . . .	21

---

<b>5</b>	<b>Numerical Results</b>	<b>22</b>
5.1	Introduction . . . . .	22
5.2	Boundary Conditions . . . . .	22
5.3	Simulation Setup . . . . .	23
5.4	Comparison of Atmospheric Boundary Layer . . . . .	24
5.5	Test D results . . . . .	28
5.6	Test J results . . . . .	38
5.7	Comparison of Test D and Test J results . . . . .	48
5.8	Comparison with experimental results . . . . .	50
5.9	Closure . . . . .	51
<b>6</b>	<b>Conclusion</b>	<b>53</b>
	<b>References</b>	<b>54</b>

## List of Figures

1	Raspodjela tlakova uslijed nastrujavanja zraka na kocku. . . . .	XIV
2	Model naftne platforme. . . . .	XV
3	Diskretizacija domene za Test D. . . . .	XVI
4	Mreža u presjeku x-z ravnine za Test D. . . . .	XVI
5	Usporedba razvijenog profila brzine. . . . .	XVII
6	Raspodjela brzine za Test D sa Reynolds Averaged Navier-Stokes Equations (RANS) modelom turbulencije. . . . .	XVIII
7	Raspodjela brzine za Test D sa Large Eddy Simulation (LES) modelom turbulencije. . . . .	XIX
8	Prikaz linija uzorkovanja raspodjele tlakova kod Testa D. . . . .	XIX
9	Raspodjela tlakova na različitim plohama modela za Test D. . . . .	XX
10	Raspodjela tlakova na različitim plohama modela za Test J. . . . .	XXI
2.1	Energy cascade. . . . .	4
3.1	Atmospheric boundary layer. . . . .	12
3.2	Different types of wind profiles. . . . .	12
3.3	Pressure distribution on cube. . . . .	14
4.1	HOE PC-Semi Full model. . . . .	15
4.2	Coordinate systems of model. . . . .	16
4.3	HOE PC-Semi Test D model. . . . .	16
4.4	HOE PC-Semi Test J model. . . . .	17
4.5	Assigned patch ID numbers on Test D. . . . .	18
4.6	Surface mesh discretization for Test D. . . . .	19
4.7	x-z slice of mesh for Test D. . . . .	19
4.8	View of the layer refinement. . . . .	19
4.9	Surface mesh discretization for Test J. . . . .	21
5.1	Location of lines for sampling the vertical velocity profiles. . . . .	24
5.2	Comparison of the inlet velocity profile with the requested velocity profile. . . . .	25
5.3	Velocity profile comparison in the model vicinity with a RANS turbulence model. . . . .	26
5.4	Velocity profile comparison in the model vicinity with a LES turbulence model. . . . .	26
5.5	Velocity profile comparison in undisturbed flow. . . . .	27
5.6	Test D force convergence with RANS turbulence model. . . . .	28
5.7	Test D force convergence with LES turbulence model. . . . .	29
5.8	Test D moment convergence with RANS turbulence model. . . . .	30
5.9	Test D moment convergence with LES turbulence model. . . . .	30
5.10	Model pressure distribution for Test D with RANS turbulence model. . . . .	31
5.11	Model pressure distribution for Test D with LES turbulence model. . . . .	32
5.12	Pressure distribution on plane $z = 0.085\text{m}$ for RANS turbulence model. . . . .	32



5.13	Pressure distribution on plane $z = 0.085\text{m}$ for LES turbulence model. . . . .	33
5.14	Lines pressure distribution for Test D. . . . .	33
5.15	Pressure distribution on different faces for Test D. . . . .	34
5.16	Pressure distribution for Test D with RANS turbulence model. . . . .	35
5.17	Pressure distribution for Test D with LES turbulence model. . . . .	35
5.18	Velocity distribution for Test D with RANS turbulence model. . . . .	36
5.19	Velocity distribution for Test D with LES turbulence model. . . . .	36
5.20	Velocity streamlines at 85% column height for Test D with RANS turbulence model. . . . .	37
5.21	Velocity streamlines at 85% column height for Test D with LES turbulence model. . . . .	37
5.22	Test J force convergence with RANS turbulence model. . . . .	39
5.23	Test J force convergence with LES turbulence model. . . . .	39
5.24	Model pressure distribution for Test J with RANS turbulence model. . . . .	40
5.25	Model pressure distribution for Test J with LES turbulence model. . . . .	40
5.26	Pressure distribution on model for Test J with RANS turbulence model. . . . .	41
5.27	Pressure distribution on model for Test J with LES turbulence model. . . . .	42
5.28	Pressure distribution on plane $z = 0.085\text{m}$ with RANS turbulence model. . . . .	42
5.29	Pressure distribution on plane $z = 0.085\text{m}$ with LES turbulence model. . . . .	43
5.30	Lines pressure distribution for Test J. . . . .	43
5.31	Pressure distribution on different faces for Test J. . . . .	44
5.32	Pressure distribution for Test J with RANS turbulence model. . . . .	45
5.33	Pressure distribution for Test J with LES turbulence model. . . . .	45
5.34	Velocity distribution for Test J with RANS turbulence model. . . . .	46
5.35	Velocity distribution for Test J with LES turbulence model. . . . .	46
5.36	Velocity streamlines at 85% column height for Test J with RANS turbulence model. . . . .	47
5.37	Velocity streamlines at 85% column height for Test J with LES turbulence model. . . . .	47
5.38	Turbulent kinetic energy. . . . .	48
5.39	Flow separation at the front pillar - Test D. . . . .	49
5.40	Flow separation at the flare boom - Test D. . . . .	49
5.41	Flow separation on front pillar - Test J. . . . .	49

## List of Tables

1	Topologija mreže za Test D. . . . .	XV
2	Topologija mreže za Test J. . . . .	XV
3	Metode diskretizacije u foam-extend korištene kod RANS i LES modela turbulencije. . . . .	XVII
4	Vrijednosti sile i momenta za Test D. . . . .	XVIII
5	Vrijednosti sile i momenta za Test J. . . . .	XVIII
6	Računalni resursi i vrijeme trajanja simulacije kod Testa D sa RANS modelom turbulencije. . . . .	XXII
7	Računalni resursi i vrijeme trajanja simulacije kod Testa D sa LES modelom turbulencije. . . . .	XXII
8	Računalni resursi i vrijeme trajanja simulacije kod Testa J sa RANS modelom turbulencije. . . . .	XXII
9	Računalni resursi i vrijeme trajanja simulacije kod Testa J sa LES modelom turbulencije. . . . .	XXII
10	Usporedba koeficijenta sile. . . . .	XXIII
11	Usporedba koeficijenta momenta. . . . .	XXIII
2.1	$k - \omega$ SST turbulence model coefficients. . . . .	8
4.1	Definition of patch topology for Test D. . . . .	18
4.2	Test D mesh topology. . . . .	20
4.3	Test J mesh topology. . . . .	20
4.4	Test D mesh quality. . . . .	20
4.5	Test J mesh quality. . . . .	20
5.1	Imposed boundary condition for simulations. . . . .	23
5.2	Discretization methods in foam-extend for RANS and LES turbulence models. . . . .	24
5.3	Test D forces and moments. . . . .	31
5.4	Test J forces and moments. . . . .	41
5.5	Hardware and computational time for Test D with RANS turbulence model. . . . .	50
5.6	Hardware and simulation time for Test D with LES turbulence model. . . . .	50
5.7	Hardware and simulation time for Test J with RANS turbulence model. . . . .	50
5.8	Hardware and simulation time for Test J with LES turbulence model. . . . .	50
5.9	Force coefficient comparison. . . . .	51
5.10	Moment coefficient comparison. . . . .	51

## Nomenclature

### Greek letters

$\alpha$	Power law exponent	-
$\delta$	Thickness of Atmospheric Boundary Layer (ABL)	m
$\gamma$	Diffusion coefficient	$\text{m}^2 / \text{s}^2$
$\nu$	Kinematic viscosity	$\text{m}^2 / \text{s}^2$
$\nu_t$	Kinematic eddy viscosity	$\text{m}^2 / \text{s}^2$
$\omega$	Specific dissipation rate	$\text{s}^{-1}$
$\phi$	Transported scalar variable	-

### Latin letters

$\mathbf{R}$	Reynolds stress tensor	$\text{m}^2 / \text{s}^2$
$\mathbf{U}(z)$	Target wind profile in $z$ -direction	m/s
$\mathbf{u}$	Velocity vector	m / s
$z$	Height	m
$z_0$	Aerodynamic surface roughness length	m
$z_{ref}$	Reference height	m
$k$	Turbulent kinetic energy	$\text{m}^2 / \text{s}^2$
$p$	Kinematic pressure	$\text{m}^2 / \text{s}$
$q_v$	Volumetric sources and sinks of the scalar field	-
$t$	Time	s
$U_0$	Velocity	m/s
$U_\delta$	Velocity value on the edge of the ABL	m/s

## Abbreviations

<b>CAD</b>	Computer Aided Design
<b>CFD</b>	Computational Fluid Dynamics
<b>RANS</b>	Reynolds Averaged Navier-Stokes Equations
<b>SST</b>	Shear Stress Transport
<b>LES</b>	Large Eddy Simulation
<b>DNS</b>	Direct Numerical Simulation
<b>FVM</b>	Finite Volume Method
<b>SGS</b>	Sub-Grid Scale
<b>ABL</b>	Atmospheric Boundary Layer
<b>HOE</b>	Houston Offshore Engineering
<b>PC</b>	Paired column
<b>RDF</b>	Računalna Dinamika Fluida
<b>DDS</b>	Deep-Draft Semi-Submersible
<b>FVM</b>	Finite Volume Method

## Abstract

Very high and complex structures need to be able to withstand the external loads imposed by nature, at least to the extent that the disastrous damage of natural forces is reduced to acceptable limits. One of such structures are oil platforms that are exposed to the influence of strong winds due to their location on the open sea. Accurate assessment and prediction of wind loads are very important for reducing adverse effects.

The current methods used for studying wind effects around objects are measurements on existing objects and measurements in wind tunnels. However they are complex and expensive. Due to the rapid development of computer technology, the unavoidable segment of complex fluid flow analysis is Computational Fluid Dynamics (CFD) which is becoming an alternative method.

In this thesis, the open source CFD package foam-extend is used to simulate incompressible flow around two different Paired-Column Semi submersible platform models (Test D and Test J). The 3D CAD models were obtained from SNAME OC-8 Comparative Wind Load Study. Numerical simulations are performed for four different cases. Each of the models are simulated with two different approaches of turbulence modelling, RANS and LES.

The results of numerical simulations are presented as images of the flow field for different variables. A comparison of the atmospheric boundary layer obtained from simulations and in the wind tunnel is shown. The values of force coefficient and moment coefficients are also compared with the values obtained in the wind tunnel.

Keywords: CFD, foam-extend, influence of wind, Paired-Column Semi submersible platform

## Sažetak

Vrlo visoke i kompleksne građevine moraju biti u stanju izdržati vremenske uvjete kojima su izložene, barem u mjeri u kojoj su katastrofalna oštećenja svedena na prihvatljivu granicu. Jedne od takvih građevina su naftne platforme koje su zbog smještenosti na otvorenom moru izložene utjecaju jakih vjetrova. Točna procjena i predviđanje opterećenje vjetra vrlo su važni u smanjenju štetnih učinaka.

Dosadašnje metode korištene u proučavanju strujanja vjetra oko objekata su mjerenje na postojećim objektima te mjerenja u zračnim tunelima, koja su zbog kompleksnosti vrlo skupa. Napretkom računalne tehnologije neizostavni segment analize kompleksnih strujanja fluida je Računalna Dinamika Fluida (RDF) (eng. "CFD") koja postaje alternativa dosadašnjim metodama.

U sklopu ovog rada, softver otvorenog koda foam-extend upotrebljen je za simulacije nestlačivog strujanja oko dva različita modela (Test D i Test J) naftne platforme konstruirane sa uparenim stupovima (eng. Paired-Column Semi submersible platform). 3D CAD model naftne platforme dobiven je u sklopu projekta Usporedna istraživanja o utjecaju vjetra. Numeričke simulacije provedene su za četiri slučaja, pri čemu su za svaki od modela korištena dva različita pristupa modeliranja turbulencije: vremenski osrednjene Navier - Stokesove jednadžbe (eng. "Reynolds Averaged Navier - Stokes", skraćeno RANS) i simulacije velikih vrtloga (eng. "Large Eddy Simulations", skraćeno LES).

Rezultati numeričkih simulacija prikazani su u obliku polja značajnih fizikalnih veličina. Izvršena je usporedba atmosferskog graničnog sloja modeliranog u simulacijama sa atmosferskim graničnim slojem dobivenim u zračnom tunelu. Isto tako uspoređene su vrijednosti normalizirane sile i normaliziranog momenta sa vrijednostima dobivenim u zračnom tunelu.

Ključne riječi: Računalna dinamika fluida, foam-extend, utjecaj vjetra na građevine, naftna platforma

## Prošireni Sažetak (Extended Abstract in Croatian)

### Uvod

U sklopu ovog rada provedene su numeričke simulacije nestlačivog strujanja zraka oko naftne platforme s uparenim stupovima te je dana usporedba dobivenih numeričkih rezultata s dostupnim eksperimentalnim podacima. 3D model naftne platforme dobiven je u sklopu projekta Usporedna istraživanja o utjecaju vjetera [1]. Cilj projekta je dati usporedbu između eksperimentalnih rezultata dobivenih u zračnom tunelu, rezultata dobivenih pomoću polu-empirijskih metoda te rezultata dobivenih CFD-om. U radu su provedene simulacije za dva različita modela naftne platforme (Test D i Test J). Da bi stvorili uvjete za provođenje numeričkog proračuna, na temelju 3D CAD modela geometrije potrebno je kreirati prostorno diskretiziranu mrežu konačnih volumena. Prostorna diskretizacija je napravljena pomoću programskog paketa *cfMesh* dok su numerički proračuni provedeni unutar softverskog paketa *foam-extend*, specijaliziranog za računalnu analizu strujanja fluida. Za modeliranje turbulencije korištena su dva pristupa: vremenski osrednjene Navier-Stokesove jednadžbe (eng. "Reynolds Averaged Navier - Stokes", skraćeno RANS) i simulacije velikih vrtloga (eng. "Large eddy simulations", skraćeno LES). Rezultati provedenih numeričkih proračuna za RANS i LES modele turbulencije prezentirani su preko grafičkih prikaza fizikalnih veličina na različitim presjecima unutar domene i na samom modelu, te su vrijednosti sile i momenta uspoređene s eksperimentalnim vrijednostima.

### Matematički model

Matematički model korišten za modeliranje nestlačivog, turbulentnog, viskoznog i jednofaznog strujanja opisan je jednadžbom očuvanja mase te Navier-Stokesovim jednadžbama, koje predstavljaju zakon očuvanja količine gibanja [2]:

$$\nabla \cdot \mathbf{u} = 0, \quad (1)$$

$$\frac{\partial \mathbf{u}}{\partial t} + \nabla \cdot (\rho \mathbf{u} \otimes \mathbf{u}) - \nabla \cdot (\nu \nabla \mathbf{u}) = -\nabla p, \quad (2)$$

gdje je  $\mathbf{u}$  brzina,  $\rho$  je gustoća fluida,  $\nu$  predstavlja koeficijent kinematičke viskoznosti, dok je  $p$  tlak.

Jednadžba 2 sastoji se od:

- vremenskog člana  $\frac{\partial \mathbf{u}}{\partial t}$ ,

- konvektivnog člana  $\nabla \cdot (\rho \mathbf{u} \otimes \mathbf{u})$ ,
- difuzijskog člana  $-\nabla \cdot (\nu \nabla \mathbf{u})$ ,
- izvorskog člana  $-\nabla p$ ,

Turbulentno strujanje je najčešći oblik strujanja u prirodi te se uvijek pojavljuje uz visoke vrijednosti Reynoldsovog broja. Turbulentno strujanje je nestacionarno strujanje, karakterizirano jakim miješanjem fluida na razini velikih i manjih čestica [2]. Za rješavanje turbulentnog strujanja postoji više različitih pristupa:

- Direktna numerička simulacija (eng. "Direct Numerical Simulation", skraćeno DNS),
- Simulacije velikih vrtloga (LES),
- Vremenski osrednjene Navier-Stokesove jednačbe (RANS).

U ovom radu koriste se RANS i LES modeli turbulencije te će njihovi pristupi biti detaljnije opisani.

Sljedeći pristup poznat kao simulacije velikih vrtloga (LES) eksplicitno rješava samo velike vrtloge dok se manji vrtlozi modeliraju [3]. Glavna ideja LES-a je filtrirati Navier-Stokesove jednačbe tako da se odvoje manji vrtlozi koji će se modelirati pomoću tzv. sub-grid modela. Za filtriranje Navier-Stokesove jednačbe osrednjena jednačba definirana je matematički kako slijedi:

$$\bar{\mathbf{u}} = \int G(\mathbf{x}, \mathbf{x}') \mathbf{u}(\mathbf{x}') d\mathbf{x}', \quad (3)$$

gdje  $G(\mathbf{x}, \mathbf{x}')$  predstavlja funkciju filtriranja, koja nakon filtriranja Navier-Stokesove jednačbe daje skup jednačbi vrlo sličnih RANS-u, no s bitnom razlikom:

$$\frac{\partial \bar{\mathbf{u}}}{\partial t} + \nabla \cdot (\overline{\mathbf{u}\mathbf{u}}) - \nabla \cdot (\nu \nabla \bar{\mathbf{u}}) = -\nabla \bar{p} + \nabla \cdot \tau, \quad (4)$$

$$\nabla \cdot \bar{\mathbf{u}} = 0, \quad (5)$$

gdje je zadnji član  $\tau$  izražen kao:

$$\tau = (\overline{\mathbf{u}\mathbf{u}} - \bar{\mathbf{u}}\bar{\mathbf{u}}) + (\overline{\mathbf{u}\mathbf{u}'} + \overline{\mathbf{u}'\mathbf{u}}) + \overline{\mathbf{u}'\mathbf{u}'}, \quad (6)$$



i predstavlja odnos između velikih i malih vrtloga. U ovom radu korišten je One Equation Eddy viskozni sub-grid model koji koristi jednu dodatnu jednadžbu za modeliranje ponašanja turbulentne kinetičke energije  $k$ .

Vremenski osrednjene Navier-Stokesove jednadžbe (RANS) trenutno je najpopularniji način modeliranja turbulencije korišten za rješavanje turbulentnog strujanja. RANS model nestacionarno turbulentno strujanje promatra kao stacionarno u osrednjenim varijablama. Ako se jednadžbe izvedu tako da ovise samo o osrednjenim karakteristikama strujanja, više nije potrebno rješavati tranzijentno strujanje te je omogućeno korištenje grublje proračunske mreže. Polja brzine i tlaka mogu se zapisati kao zbroj vremenski osrednjene i fluktuirajuće komponente:

$$\mathbf{u} = \bar{\mathbf{u}} + \mathbf{u}', \quad (7)$$

$$p = \bar{p} + p', \quad (8)$$

gdje su  $\bar{\mathbf{u}}$  i  $\bar{p}$  osrednjene vrijednosti, dok su  $\mathbf{u}'$  i  $p'$  fluktuirajuće komponente. Uvrštavajući gore navedene jednadžbe ((7) i (8)) u Navier-Stokesove jednadžbe te izbacivanjem članova koji sadrže umnožak osrednjene i fluktuirajuće komponente dobivaju se vremenski osrednjene jednadžbe kako slijedi [2]:

$$\frac{\partial \bar{\mathbf{u}}}{\partial t} + \nabla \cdot (\overline{\mathbf{u}\mathbf{u}}) - \nabla \cdot (\nu \nabla \bar{\mathbf{u}}) = -\nabla \bar{p} + \nabla \cdot (\overline{\mathbf{u}'\mathbf{u}'}), \quad (9)$$

$$\nabla \cdot \bar{\mathbf{u}} = 0. \quad (10)$$

Dodatni član na krajnjoj desnoj strani jednadžbe (9) proizlazi iz nelinearnosti konvekcijskog člana, a zove se Reynoldsov tenzor naprezanja te prema Boussinesqovoj aproksimaciji [4] može se modelirati kako slijedi:

$$\mathbf{R} = \nu_t \frac{1}{2} [\nabla \bar{\mathbf{u}} + (\nabla \bar{\mathbf{u}})^T], \quad (11)$$

pri čemu je  $\nu_t$  turbulentna viskoznost. Da bi mogli procijeniti turbulentnu viskoznost uz transportnu jednadžbu za turbulentnu kinetičku energiju  $k$ , potrebno je poznavati još duljinsku ili vremensku skalu. To se postiže formuliranjem slične transportne jednadžbe za turbulentnu

disipaciju  $\varepsilon$  ili specifičnu disipaciju  $\omega$ . Na takav način nastaju dva najpoznatija modela turbulencije poznatiji kao  $k - \varepsilon$  model i  $k - \omega$  SST model [5], koji je korišten u ovom radu.

## Utjecaj vjetra na građevine

Zgrade, pomorski objekti i ostale građevine moraju biti u stanju izdržati vremenske uvjete kojima su izložene, barem do te mjere kada je šteta svedena na prihvatljivu granicu. Kod takvih objekata točna procjena i predviđanje opterećenja vrlo su važni u smanjenju štetnih učinaka. Trenutno postoji nekoliko različitih pristupa kojima se proučava djelovanje vjetra na objekte [6]:

- mjerenje na stvarnim objektima u stvarnom vremenu,
- mjerenja u zračnim tunelima,
- polu-empirijski modeli,
- Računalna dinamika fluida (RDF).

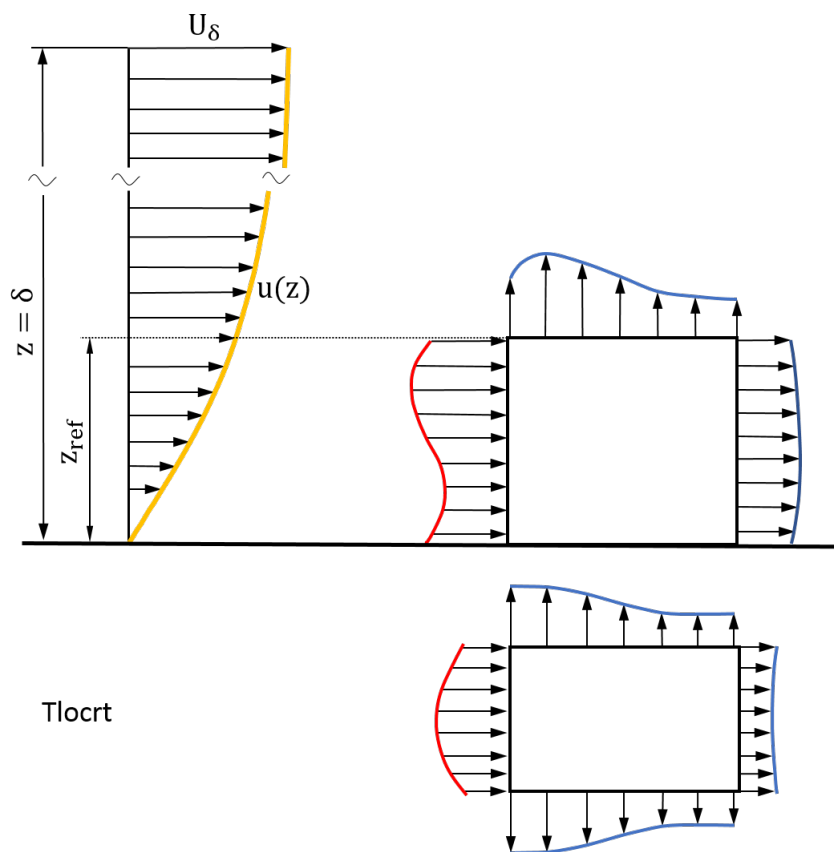
Atmosferski granični sloj predstavlja dio troposfere unutar kojeg nastaje struktura strujanja zraka u direktnoj interakciji s površinom Zemlje. Uslijed trenja su osrednjene vrijednosti brzine na podlozi jednake nuli i rastu do maksimuma na rubu graničnog sloja. Pritom su vrijednosti parametara koji karakteriziraju turbulentnu strukturu graničnog sloja maksimalne u blizini podloge i opadaju s povećanjem udaljenosti od podloge [6]. Kako bi mogli usporediti rezultate dobivene mjerenjem u zračnom tunelu i rezultate dobivene CFD analizom potrebno je definirati atmosferski granični sloj u simulacijama sličan onome koji se razvije u zračnom tunelu. Tako je profil brzine zadan prema sljedećem izrazu [1]:

$$U(z) = U_0 \left[ 1 + C \cdot \ln \left( \frac{z}{z_{ref}} \right) \right], \quad (12)$$

$$C = 0.0573 \cdot (1 + 0.15 \cdot U_0)^{\frac{1}{2}}, \quad (13)$$

pri čemu je  $U(z)$  profil brzine vjetra u m/s,  $z_{ref}$ [m] je aerodinamička duljina hrapavosti, i  $U_0$ [m/s] je brzina na vrhu graničnog sloja [1].

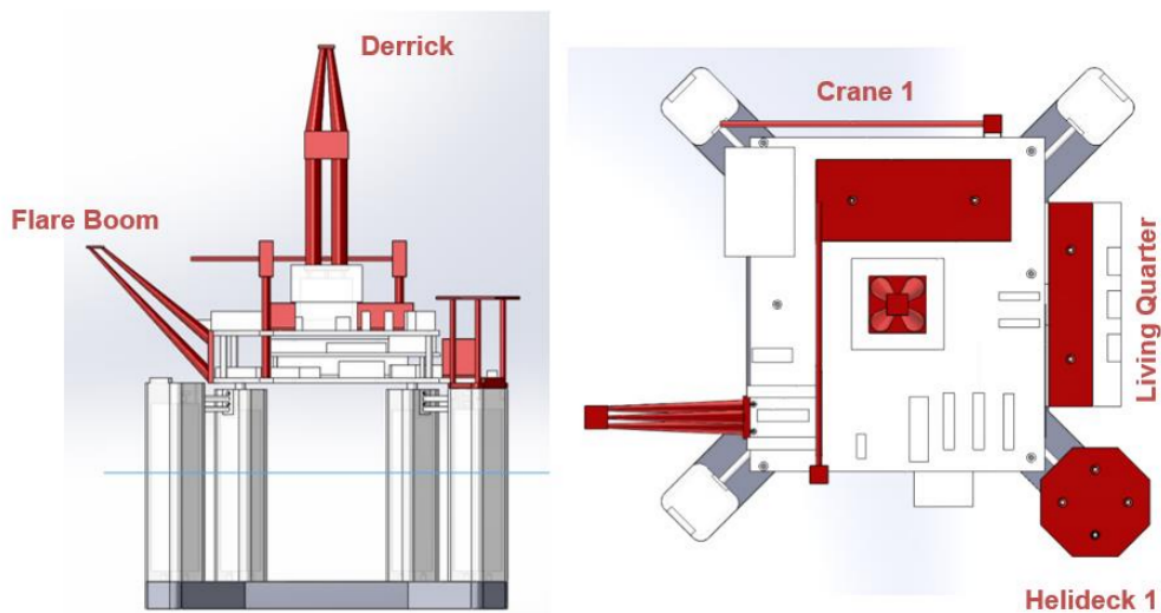
Opterećenje uslijed djelovanja vjetra na objekte koji nisu skloni osjetnom vibriranju proporcionalno je kvadratu brzine. Prilikom nastrojavanja vjetra na objekte, postoje karakteristične raspodjele tlakova koje se javljaju. Na slici 1 prikazane su raspodjele tlakova koje nastaju uslijed nastrojavanja na kocku.



Slika 1: Raspodjela tlakova uslijed nestrujavanja zraka na kocku [6].

## Rezultati simulacija

Simulacije su provedene na dva različita modela naftne platforme. Pomoću programskog paketa *SolidWorks* na glavnom modelu uklonjen je dio "helideck 1" te je u daljnjem tekstu taj model predstavljen kao Test D. Za drugi model uklonjeni su redom dijelovi: "derrick", "flare boom", "crane 1", "living quarters" i "helideck 1" te je taj model predstavljen kao Test J. Na slici 2 prikazan je model naftne platforme sa svim dijelovima.



Slika 2: Model naftne platforme [1].

Na temelju 3D CAD modela generirana je proračunska mreža pomoću programskog paketa *cfMesh*. Mreža je hibridna, odnosno sastoji se od strukturiranih i nestrukturiranih dijelova. U tablici 1 i 2 prikazane su topologije mreže za Test D i Test J.

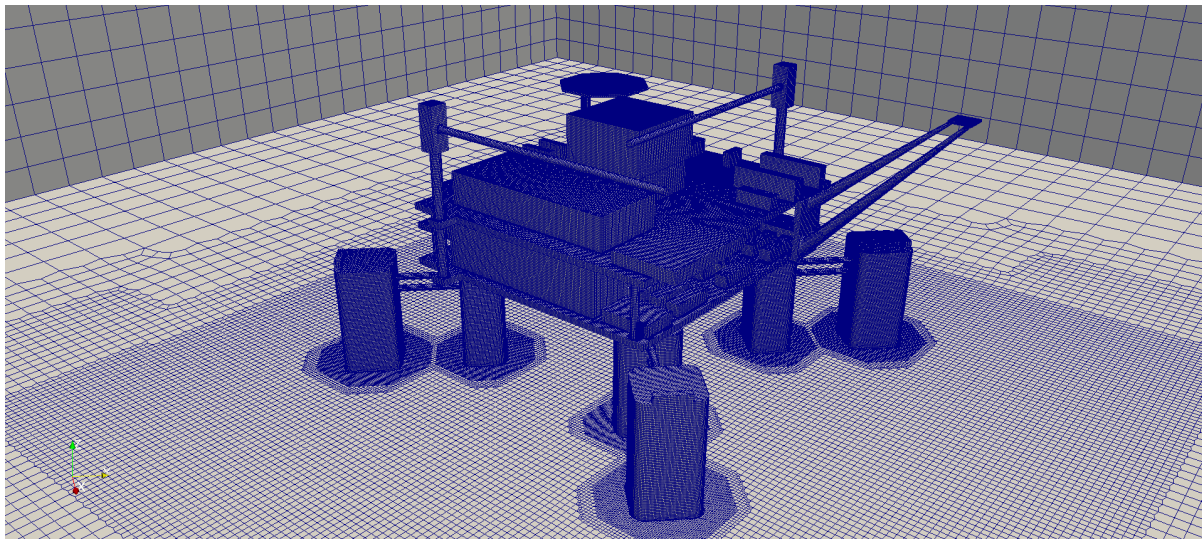
Tablica 1: Topologija mreže za Test D.

Number of cells	
Hexahedra	8 602 872
Prizma	15 540
Piramida	14 303
Tetraedri	10 970
Poliedra	183 055
<b>Ukupno</b>	<b>8 826 740</b>

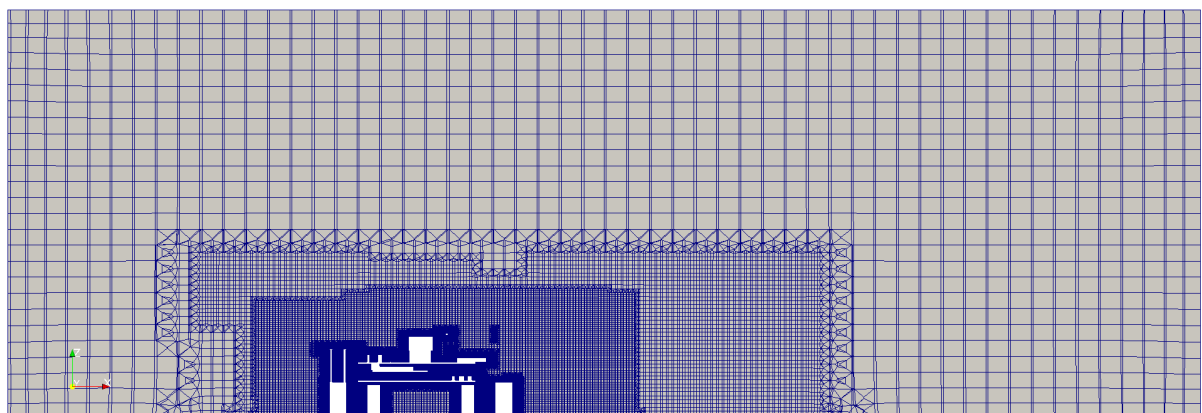
Tablica 2: Topologija mreže za Test J.

Number of cells	
Hexahedra	7 764 173
Prizma	13 306
Piramida	12 803
Tetraedri	9 538
Poliedra	161 057
<b>Ukupno</b>	<b>7 960 877</b>

Kako su modeli u Testu D i Testu J slične geometrije, proračunske domene su slične te je dan prikaz mreže samo za Test D. Slika 3 prikazuje prostornu domenu oko cijelog modela platforme. Na slici 4 vidljiv je prijelaz mreže s finijeg na grublji sloj dobiven presijecanjem domene sa  $x - z$  ravninom.



**Slika 3: Diskretizacija domene za Test D.**



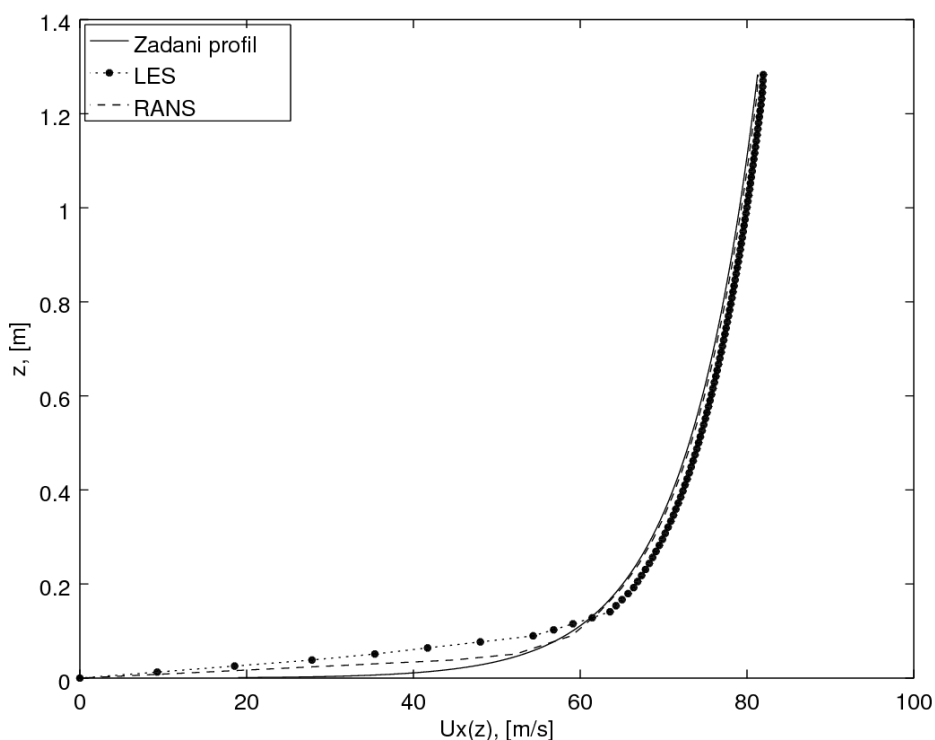
**Slika 4: Mreža u presjeku x-z ravnine za Test D.**

Računalne simulacije provedene su pomoću nestacionarnog rješavača `pimpleFoam` unutar softvera otvorenog koda `foam-extend`. Kako bi se konvergencija rezultata dobila u što kraćem vremenu polja su inicijalizirana prvo s potencijalnim rješavačem `potentialFoam` te nakon toga sa stacionarnim rješavačem `simpleFoam`. Kako je korišten nestacionarni rješavač u obzir je uzeta vrijednost Couranovog broja. Vrijednost Couranovog broja je postavljena da bude manja od 5 ( $Co < 5$ ). Ako bi smanjili dozvoljenu vrijednost Couranovog broja direktno bi utjecali na vrijeme potrebno za provedbu simulacije. Metode diskretizacije korištene u simulacijama za RANS i LES modele turbulencije su jednake te su navedene u tablici 3.

**Tablica 3: Metode diskretizacije u foam-extend korištene kod RANS i LES modela turbulencije.**

Matematički operator	Metoda diskretizacije
Vremenski član	Euler
Konvektivni član	Gauss upwind/ Gauss linear
Difuzijski član	Gauss linear corrected

Na slici 5 je napravljena usporedba profila brzine dobivene u zračnom tunelu s profilima dobivenim CFD analizom. Usporedbom profile brzina s traženim profilom u području potpuno razvijenog profila brzine, vidljivo je kako LES turbulentni model ima puno veća odstupanja u donjem dijelu profila (slika 5). Razlog je taj što je LES turbulentni model osjetljiviji na kvalitetu mreže.

**Slika 5: Usporedba razvijenog profila brzine.**

Vrijednosti sile i momenta dobivenih CFD analizom za Test D prikazani su u tablici 4 dok su za Test J prikazani u tablici 5. S obzirom na to da je smjer strujanja u smjeru osi  $x$ , vrijednost sile u tom smjeru je dominantna te se najveći moment javlja oko osi  $y$ . Isto tako vidi se kako su vrijednosti sile  $F_x$  i momenta  $M_y$  veće za LES turbulentni model pri čemu su srednja odstupanja manja.

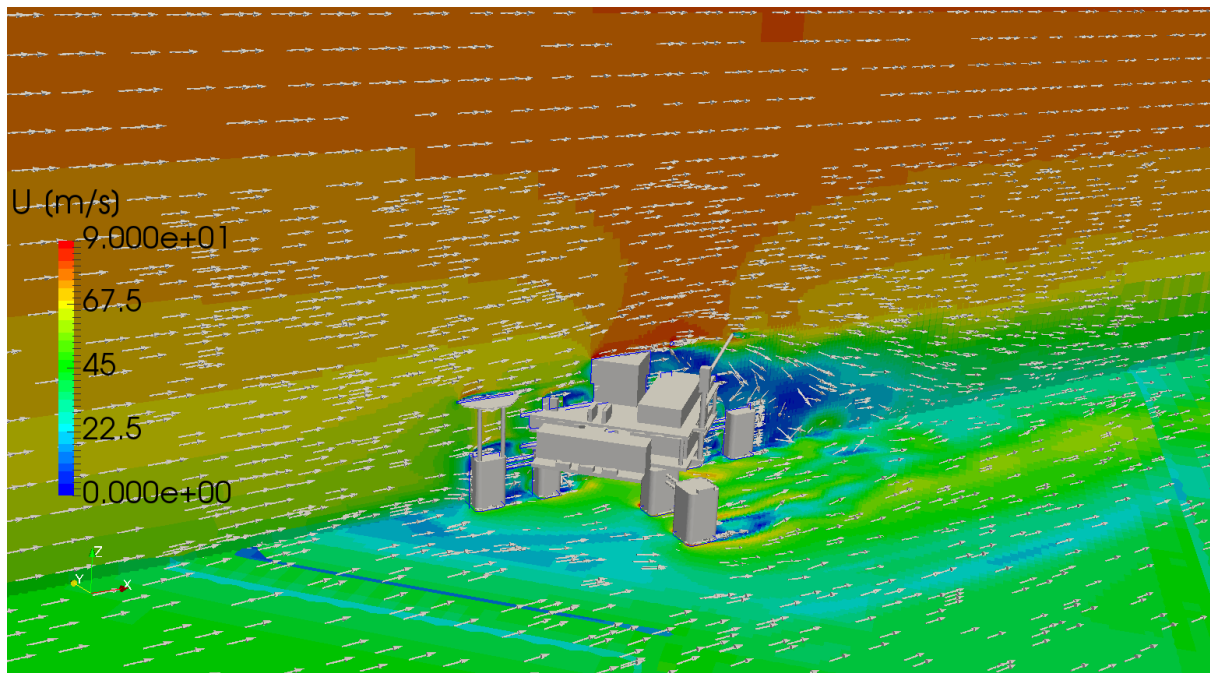
**Tablica 4: Vrijednosti sile i momenta za Test D.**

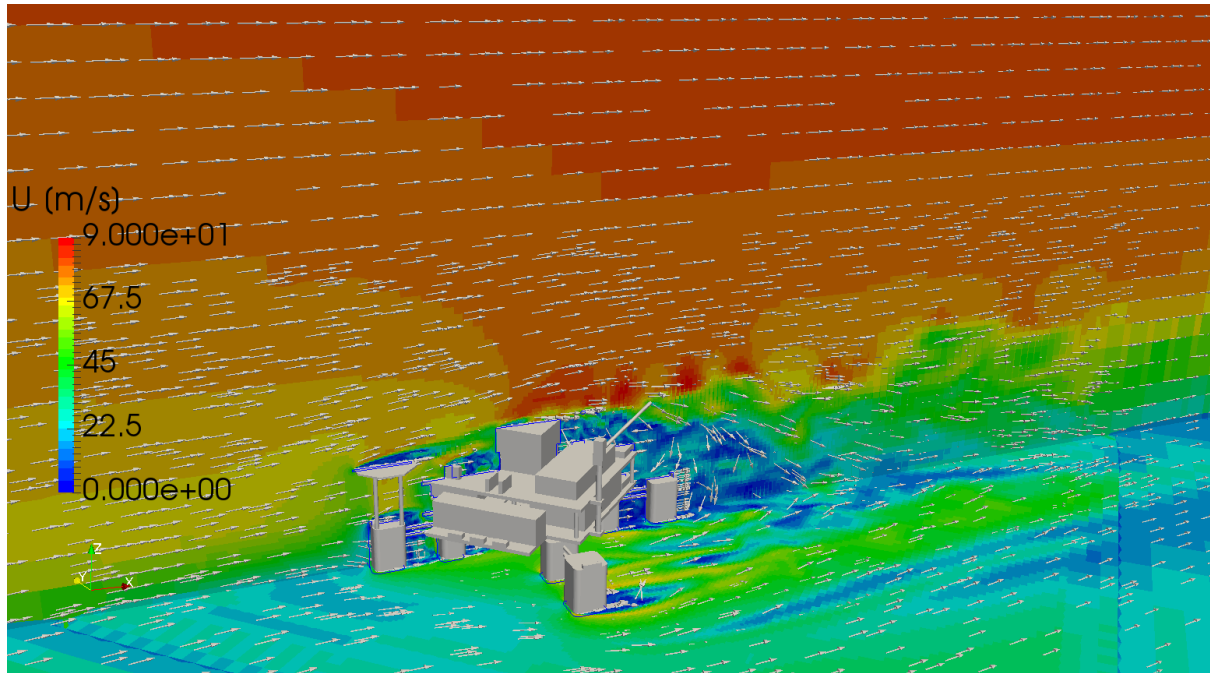
Model Turbulencije	$F_x$ [N]	$F_y$ [N]	$F_z$ [N]	$M_x$ [Nm]	$M_y$ [Nm]	$M_z$ [Nm]
RANS	$132 \pm 4$	$2 \pm 5$	$16 \pm 4$	$0.8 \pm 0.5$	$13.2 \pm 0.4$	$-1.5 \pm 1$
LES	$139.5 \pm 2$	$6 \pm 2$	$20 \pm 3$	$0.55 \pm 0.3$	$14.5 \pm 0.5$	$-1.8 \pm 0.5$

**Tablica 5: Vrijednosti sile i momenta za Test J.**

Model Turbulencije	$F_x$ [N]	$F_y$ [N]	$F_z$ [N]	$M_x$ [Nm]	$M_y$ [Nm]	$M_z$ [Nm]
RANS	$126 \pm 2$	$4 \pm 3$	$5 \pm 5$	$0.5 \pm 0.4$	$10.4 \pm 0.2$	$-1 \pm 1$
LES	$132.5 \pm 2$	$5 \pm 2$	$0 \pm 5$	$0.5 \pm 0.5$	$11.2 \pm 0.2$	$-1 \pm 0.5$

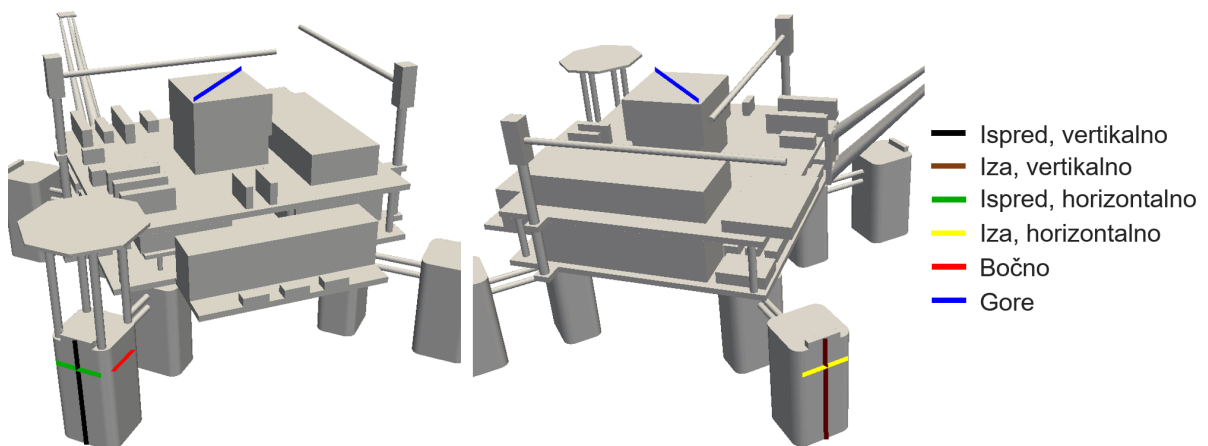
Slika 6 i 7 prikazuju raspodjelu i vektore brzine u presjeku s ravninama  $y = 0$  i  $z = 0$ . Na slikama se može vidjeti kako RANS model turbulencije ima glađu raspodjelu brzine dok kod LES modela turbulencije postoji puno više vrtloženja.

**Slika 6: Raspodjela brzine za Test D sa RANS modelom turbulencije.**



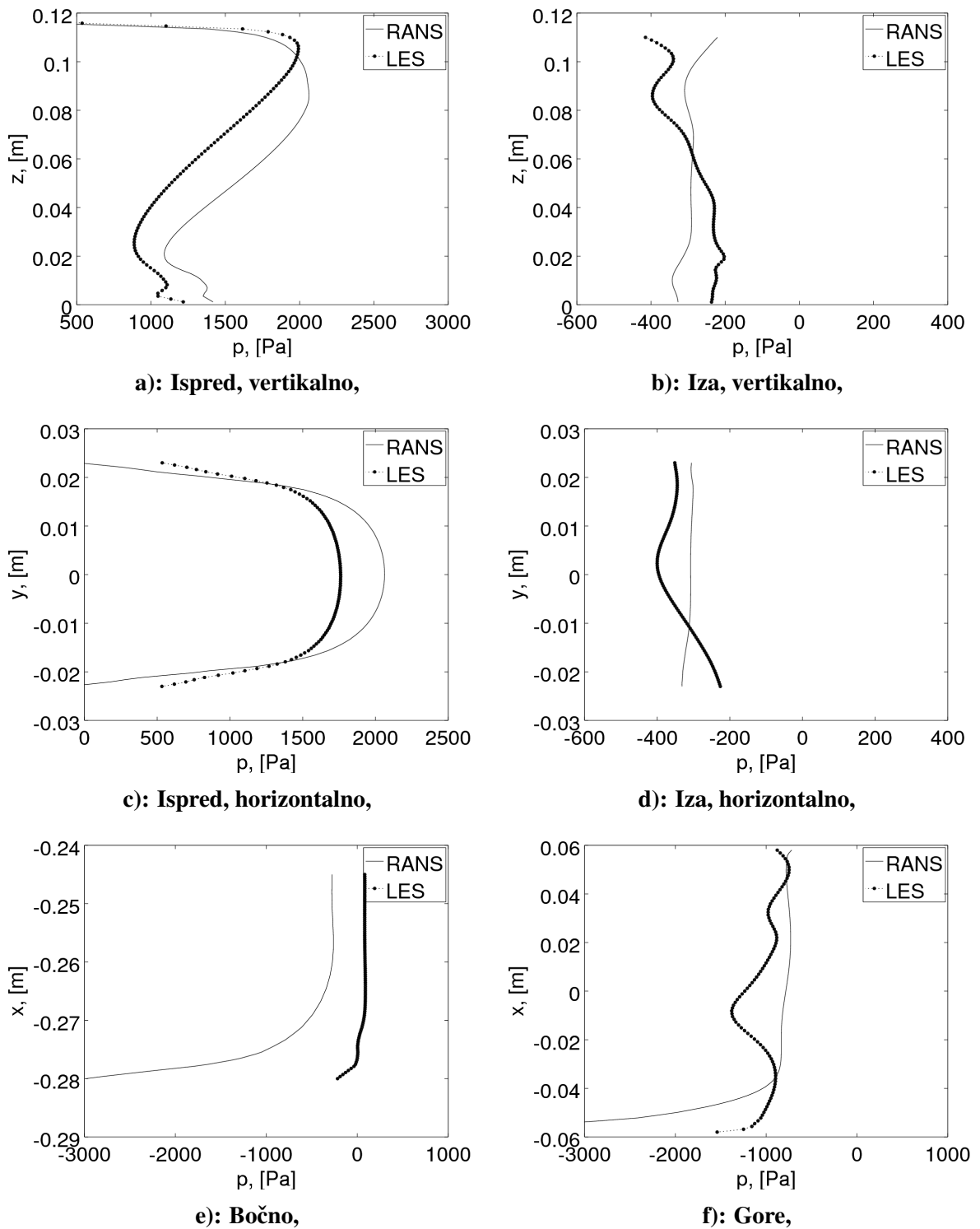
**Slika 7: Raspodjela brzine za Test D sa LES modelom turbulencije.**

Grafovi na slikama 9a - 9f prikazuju raspodjelu tlakova na različitim plohama modela, linije su označene na slici 8. Usporedbom raspodjele tlakova na kocki kao što je prikazano na slici 1 s dijagramima na slici 9, može se uočiti da se raspodjela tlakova po prednjoj plohi najviše poklapa (slika 9a i 9c). Zbog zaobljenih rubova na stupovima dolazi do ranijeg odvajanja strujanja pa to uzrokuje veliki pad tlaka na bočnoj strani što je prikazano na dijagramu 9e. Slično strujanje javlja se na gornjoj plohi gdje zbog "helideck"-a također dolazi do odvajanja strujanja te raspodjela tlakova je jednaka kao na slici 9f. Grafovi sa slike 9b i 9d dobiveni su uzorkovanjem tlaka na stražnjoj plohi zadnjeg stupa.



**Slika 8: Prikaz linija uzorkovanja raspodjele tlakova kod Testa D.**

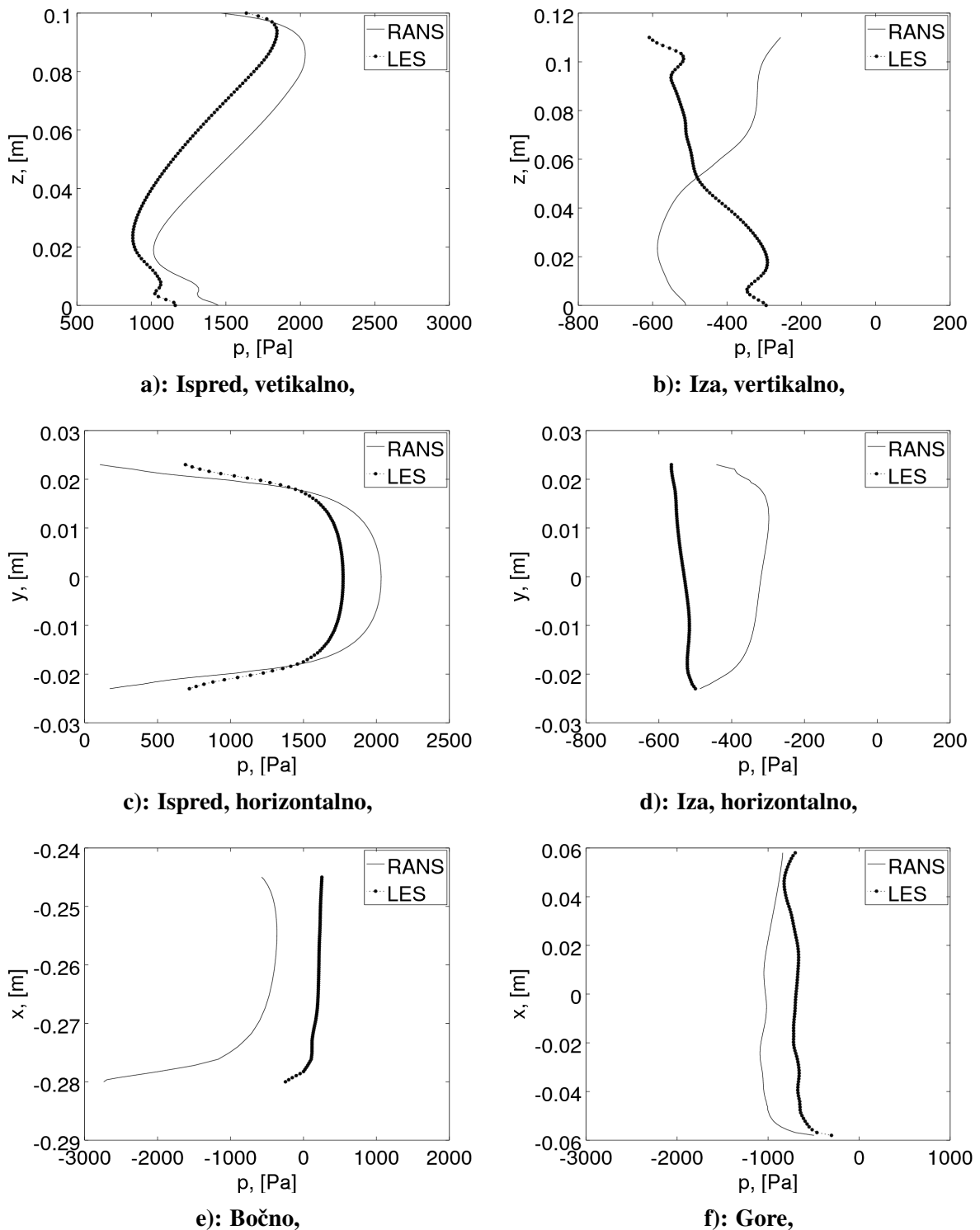




Slika 9: Raspodjela tlakova na različitim plohama modela za Test D.

Kod simulacija za Test J raspodjele tlakova uzorkovane su na identičnim pozicijama kao i za Test D. Na slikama 10a-10f prikazani su grafovi raspodjele tlakova za Test J. Ako usporedimo raspodjelu tlakova između Testa D i Testa J, može se reći da su na prednjem stupu raspodjele poprilično jednake (slike: 10a, 10c i 10e). Razlika se javlja na stražnjoj plohi gdje dolazi do

većeg pada tlaka (slike 10b i 10d) i na gornjoj plohi gdje zbog uklonjenog dijela helideck, sada nema tako jakog odvajanja strujanja te je raspodjela tlaka puno mirnija (slika 10f).



**Slika 10: Raspodjela tlakova na različitim plohama modela za Test J.**

U tablicama 6 - 9 prikazane su informacije o trajanju simulacija te korišteni računalni resursi.

**Tablica 6: Računalni resursi i vrijeme trajanja simulacije kod Testa D sa RANS modelom turbulencije.**

CPU	i7-6800K at 3.4 GHz
Broj jezgri procesora	4
RAM	64 GB DDR4
Vremenski korak [s]	$2.5375 \cdot 10^{-6}$ s
Broj iteracija	38 809
Trajanje simulacije [h]	357.9 sati

**Tablica 7: Računalni resursi i vrijeme trajanja simulacije kod Testa D sa LES modelom turbulencije.**

CPU	i5-4570K at 3.2 GHz
Broj jezgri procesora	4
RAM	32 GB DDR4
Vremenski korak [s]	$2.9956 \cdot 10^{-6}$ s
Broj iteracija	26 842
Trajanje simulacije [h]	621.2 sati

**Tablica 8: Računalni resursi i vrijeme trajanja simulacije kod Testa J sa RANS modelom turbulencije.**

CPU	i5-4570K at 3.2 GHz
Broj jezgri procesora	4
RAM	32 GB DDR4
Vremenski korak [s]	$4.2965 \cdot 10^{-6}$ s
Broj iteracija	10 498
Trajanje simulacije [h]	212.2 sati

**Tablica 9: Računalni resursi i vrijeme trajanja simulacije kod Testa J sa LES modelom turbulencije.**

CPU	i7-6800K at 3.4 GHz
Broj jezgri procesora	4
RAM	64 GB DDR4
Vremenski korak [s]	$4.5549 \cdot 10^{-6}$ s
Broj iteracija	23 174
Trajanje simulacije [h]	244.5 sati

Kod usporedbe rezultata dobivenih CFD proračunima s eksperimentalnim vrijednostima, dobivene sile i momenti prikazani su u normaliziranom obliku podijeljeni s dinamičkim tlakom:

$$C_F \cdot S = \frac{F_x}{q_{ref}} \quad (14)$$

$$C_M \cdot S \cdot L = \frac{M_y}{q_{ref}} \quad (15)$$

gdje  $q_{ref} = \frac{1}{2}\rho U_0^2$  predstavlja referentni dinamički tlak,  $S$  je projicirana površina, dok je  $L$  karakteristična duljina modela. Važno je napomenuti da za dobivanje koeficijenta  $C_F$  i  $C_M$  nije nužno poznavati vrijednost projicirane površine i karakteristične duljine modela.

U tablici 10 prikazane su vrijednosti koeficijenta  $C_{F_{exp}}$  dobivene eksperimentalno u zračnom tunelu i vrijednosti dobivene CFD analizama,  $C_{F_{RANS}}$  i  $C_{F_{LES}}$  te njihova relativna razlika.

**Tablica 10: Usporedba koeficijenta sile.**

Model	eksperiment	CFD RANS	CFD LES	RANS odstupanje	LES odstupanje
	$C_{F_{exp}}$	$C_{F_{RANS}}$	$C_{F_{LES}}$	$ \varepsilon_{C_{F_{RANS}}} [ \% ]$	$ \varepsilon_{C_{F_{LES}}} [ \% ]$
Test D	0.11097	$0.09426 \pm 0.003$	$0.09961 \pm 0.0015$	14.47%	9.61%
Test J	0.0764	$0.08997 \pm 0.0015$	$0.09462 \pm 0.0015$	17.77%	23.84%

U tablici 11 prikazane su vrijednosti koeficijenta  $C_{M_{exp}}$  dobivene eksperimentalno u zračnom tunelu i vrijednosti dobivene CFD analizama  $C_{M_{RANS}}$  i  $C_{M_{LES}}$ , te odstupanje CFD rezultata od eksperimentalnih.

**Tablica 11: Usporedba koeficijenta momenta.**

Model	eksperiment	CFD RANS	CFD LES	RANS odstupanje	LES odstupanje
	$C_{M_{exp}}$	$C_{M_{RANS}}$	$C_{M_{LES}}$	$ \varepsilon_{C_{M_{RANS}}} [ \% ]$	$ \varepsilon_{C_{M_{LES}}} [ \% ]$
Test D	0.00977	$0.00943 \pm 0.0003$	$0.01028 \pm 0.00036$	3.52%	5.24%
Test J	0.00697	$0.00074 \pm 0.00014$	$0.00079 \pm 0.00014$	6.55%	14.74%

## Zaključak

Nakon provedenih simulacija na dva različita modela platforme s dva različita pristupa modeliranju turbulencije i usporedbom rezultata s eksperimentalnim vrijednostima dobivenim mjerenjem u zračnom tunelu, pokazalo se da RANS turbulentni model daje bolje rezultate od LES turbulentnog modela. Ako uzmemo u obzir da dobiveni profil brzine s LES turbulentnim modelom ima znatno veće odstupanje od traženog profila brzine tu dolazi do greške u odnosu na eksperimentalne rezultate. Progušćivanjem mreže odstupanje bi se smanjilo te je potrebno pronaći optimum između kvalitete mreže i vremena potrebnog za provedbu simulacije.

Isto tako pokazano je kako se CFD analizama koje su znatno jeftinije i brže mogu dobro predvidjeti opterećenja nastala djelovanjem vjetra na građevine.

# 1 Introduction

Fluids surround the whole world, so most of the engineering problems are at least in some way related to fluid dynamics. One of such problems is the impact of wind on buildings. Previous research have shown that accurate evaluation and prediction of wind loads is very important in reducing the adverse effects. There are several different approaches to studying the problem of wind impact on objects [6]. One such method is CFD. The development of CFD is closely related to the very rapid development of computers in the previous couple of decades. Presently, companies need to have quick responses to market demands in order to survive. In this CFD stands out in front of other methods. Unlike experimental methods, CFD can offer faster and more cost-effective solutions. For this thesis, the community driven fork of open source CFD software OpenFOAM called `foam-extend` [7] is used to simulate incompressible, single-phase, turbulent and viscous fluid flow [2] around two different PC-Semi submersible platform models.

The PC-Semi submersible platform is a Deep-Draft Semi-Submersible (DDS) designed by Houston Offshore Engineering. It has 8 columns instead of 4 compared to conventional DDS [8]. The origins of semi-submersible floating production systems date back to 1960s. Semi-submersible platforms are widely installed in offshore oil and gas fields all over the world. Wind forces contribute significantly to the total environmental loads on offshore structures, specially during a hurricane. Drag forces are of importance for mooring, dynamic positioning and maneuvering of floating structures. The stability of floating and fixed structures may be affected by overturning moments due to drag and lift forces. Knowledge of these loads is therefore indispensable for the design and operation of such structures [9].

The study was conducted as part of the SNAME OC-8 Comparative Wind Load Study [1] project in which the aim is to show a comparison between results obtained with a semi-empirical model, wind tunnel measurements and CFD analysis. Based on the generated full CAD model obtained from SNAME OC-8 Comparative Wind Load Study, *SolidWorks* program package will be used to remove parts for Test J and Test D model [10]. To create spatial domain discretization, a software package *cfMesh* will be used [11]. This strip-down test is performed according to the simulation guidelines by the SNAME OC-8 committee.

The aim of this thesis is to investigate different turbulence modeling approaches (RANS and LES) for assessing wind loads accurately. The main idea of RANS approach is to decompose the flow field quantities into their mean and fluctuating components, and ignore the influence of instantaneous terms which are not of interest, while the basic philosophy of LES is to resolve larger eddies while the smallest eddies are modeled [4, 3, 12, 2, 5]. In order to compare CFD with the wind tunnel results it is necessary to define a realistic wind velocity profile in the atmospheric boundary layer will be defined and compared to wind tunnel measurements.

For such wind profile, simulations for Test D and Test J should be performed with RANS and LES turbulence models. Finally, a validation study will be performed by comparing the

results to experimental measurements reported in SNAME OC-8 [13].

This thesis is organised as follows: Section 2 serves as an introduction to the governing equations of incompressible fluid flow. Along with the main properties of turbulence models, two approaches to modeling turbulence and boundary conditions are explained. Section 3 presents several different approaches for studying the problem of wind impact on objects and basic properties of atmospheric boundary layer. Section 4 shows the geometry of Houston Offshore Engineering Paired Column-Semi submersible platform and describes the process of spatial discretization of the model geometry. In Section 5 the numerical simulations for four different cases are presented and at the end of this section a comparison with experimental results is shown. Finally, a brief conclusion is given in section 6.

## 2 Mathematical model

### 2.1 Introduction

The purpose of this section is to present the governing equations of incompressible, single-phase, turbulent and viscous fluid flow. The second subsection presents the turbulence models used in simulations. In order for a system of partial differential equations to have an unique solution, boundary conditions are necessary. Three basic categories of numerical boundary conditions as well as two types of specific boundary conditions are described.

### 2.2 Governing equations of fluid flow

Large number of flow-related problems can be solved using different forms of a basic transport equations. In the end, the modeled equations may be more complex, however the basic form is the same. Generic scalar transport equation in its standard and generalized form is expressed as [2] :

$$\underbrace{\frac{\partial \phi}{\partial t}}_{\text{temporal derivative}} + \underbrace{\nabla \cdot (\phi \mathbf{u})}_{\text{convection term}} - \underbrace{\nabla \cdot (\gamma \nabla \phi)}_{\text{diffusion term}} = \underbrace{q_v}_{\text{source term}}, \quad (2.1)$$

where  $\phi$  is a transported scalar variable,  $\mathbf{u}$  is the convective velocity,  $\gamma$  is the diffusion coefficient and  $q_v$  is an arbitrary local volume source or sink of transported scalar  $\phi$ .

The standard transport equation contains four characteristic terms:

- temporal derivative presents the inertia of the system,
- convection term represents the convective transport by the prescribed velocity field  $\mathbf{u}$ . The term is of hyperbolic nature because information comes from vicinity, defined by the direction of the convection velocity,
- diffusion term, which represents gradient transport. Every point in the domain feels the influence of every other point instantaneously, hence this is an elliptic term,
- source and sink terms describe non-transport effects, which means local production and destruction of  $\phi$ .

In this thesis, an incompressible, single-phase and viscous flow model is used and it is described by the Navier-Stokes equations. To thoroughly describe the flow of incompressible viscous fluids, the momentum equation is expanded with mass and energy conservation equations. Since the heat transfer does not exist in this thesis, the energy conservation



equation is neglected. The governing equations for incompressible, isothermal flow are defined as follows:

$$\nabla \cdot \mathbf{u} = 0, \quad (2.2)$$

$$\frac{\partial \mathbf{u}}{\partial t} + \nabla \cdot (\rho \mathbf{u} \otimes \mathbf{u}) - \nabla \cdot (\nu \nabla \mathbf{u}) = -\nabla p, \quad (2.3)$$

where  $\mathbf{u}$  is velocity field,  $\rho$  is density of the fluid,  $\nu$  represents kinematic molecular viscosity, while  $p$  is the kinematic pressure.

### 2.3 Turbulence modelling

Turbulent fluid flow is the most common form of flow in nature, and it always appears at high Reynolds number. It is characterized by irregularity, disorderly, non-stationary, three-dimensional, highly non-linear, irreversible stochastic phenomenon [2] with increased diffusivity and energy dissipation. Turbulence is usually present in a form of vortex dynamics, where the energy distribution across different vortical scales is shown in Figure 2.1

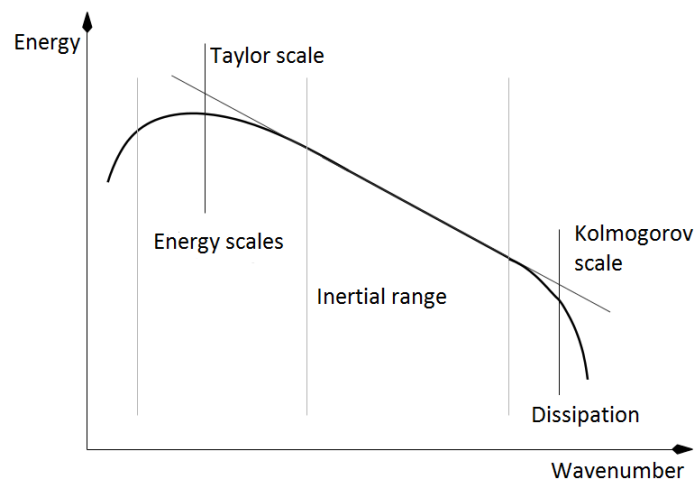


**Figure 2.1: Energy cascade [2].**

Figure 2.1 shows turbulent energy with respect to the wave number of turbulent eddies. The highest amount of turbulent kinetic energy is contained in the largest vortices which are described with Taylor length scale. On the other side, the smallest turbulent vortices contain a small amount of turbulent kinetic energy and its represented with Kolmogorov length-scale. The largest vortices are created by the flow through the domain and they decay because of

vortex stretching into smaller ones, which then decay to even smaller up to the smallest-scale vortices. Through the process of vortex decomposition, turbulent kinetic energy is transmitted from large to small vortices and finally from the smallest vortices the kinetic energy is dissipated in the heat due to viscous effects.

For described turbulent lengths, there are several different modelling approaches for solving turbulent flow:

- Direct Numerical Simulation (DNS),
- Large Eddy Simulation (LES),
- Reynolds Averaged Navier-Stokes Equations (RANS).

When performing Direct Numerical Simulation (DNS), which is not really a model of turbulence, Navier-Stokes equations are solved over the whole range of turbulent scales in the transient flow. In order to perform the simulation well, the requirements on mesh resolution and time-step size put very high demands on the computer resources. Due to the high computational cost, DNS is rarely used for industrial computations but are usually used to solve simple flows to expand knowledge about turbulence.

The second approach is generally known as Large Eddy Simulation (LES). The basic philosophy of LES is to explicitly compute only larger eddies while the smallest eddies are simply modelled [3]. The main idea in LES is to filter the Navier-Stokes equation to determine which scales to keep and which scales to discard. Smaller energy-dissipating vortex scales are modelled using sub-grid scale models, thus reducing the need for spatial resolution. As those scales are approaching homogenous and isotropic turbulence, which is easier to model, LES is becoming ever more important in solving complex turbulent flows.

Raynolds Averaged Navier-Stokes (RANS) is currently the most popular approach for solving industrial turbulent flow problems and is based on solves the averaged Navier-Stokes equations in order to obtain mean values of the flow rate of the field. The main idea of RANS approach is to decompose flow field quantities into their mean and fluctuating components, and ignore the influence of instantaneous terms which are not of interest. A coarser numerical grid can be used as it is no longer necessary to perform transient simulation for equations which depend only on the mean flow characteristics. In this thesis, RANS and LES model are used, hence they will be explained further.

### **2.3.1 Reynolds Averaged Navier-Stokes Equations**

As mentioned above, in the turbulence we are mostly interested in mean components which describe the flow and ignore the fluctuations. Velocity and pressure fields can be expressed as a sum of the mean and fluctuating values [12]:

$$\mathbf{u} = \bar{\mathbf{u}} + \mathbf{u}', \quad (2.4)$$

$$p = \bar{p} + p', \quad (2.5)$$

where  $\bar{\mathbf{u}}$  and  $\bar{p}$  present mean values, while  $\mathbf{u}'$  and  $p'$  are fluctuating parts of velocity and pressure, respectively. By substituting the above (Eq. (2.4) and Eq. (2.5)) into the original Reynolds-Averaged Navier-Stokes equations, and eliminating all terms containing products of mean and fluctuating values, the time-averaged continuity equation are derived:

$$\frac{\partial \bar{\mathbf{u}}}{\partial t} + \nabla \cdot (\bar{\mathbf{u}}\bar{\mathbf{u}}) - \nabla \cdot (\nu \nabla \bar{\mathbf{u}}) = -\nabla \bar{p} + \nabla \cdot (\overline{\mathbf{u}'\mathbf{u}'}), \quad (2.6)$$

$$\nabla \cdot \bar{\mathbf{u}} = 0. \quad (2.7)$$

In Eq. (2.6) and Eq. (2.7) mean velocity is taking place of the instantaneous velocity. The equations obtained have the same form as Eq. (2.2) and Eq. (2.3), except the new term  $\overline{\mathbf{u}'\mathbf{u}'}$  that appears on the right side of the averaged momentum equation. This term is called the Reynolds stress tensor:

$$\mathbf{R} = \overline{\mathbf{u}'\mathbf{u}'}. \quad (2.8)$$

$\mathbf{R}$  is a second rank symmetric tensor which brings six additional unknowns in the system of equations; thus the number of unknowns exceeds the number of equations. In order to close the system, the unknown values need to be described. With reference to the Boussinesq approximation [4], the Reynolds-stress tensor can be modelled as a linear function of an mean strain rate tensor (which represents the gradient of the flow velocity):

$$\mathbf{R} = \nu_t \frac{1}{2} [\nabla \bar{\mathbf{u}} + (\nabla \bar{\mathbf{u}})^T], \quad (2.9)$$

where  $\nu_t$  is turbulent viscosity defined as:

$$\nu_t = Au\nabla, \quad (2.10)$$

where  $A$  is a constant that allows the model to adapt to real physical behavior,  $u$  is the velocity scale and  $\nabla$  represents the length scale. In almost all turbulence models, turbulent kinetic energy  $k$  is used for approximating the velocity scale which is defined according to:

$$k = \frac{3}{2} \mathbf{u}' \mathbf{u}' \quad (2.11)$$

The kinematic eddy viscosity  $\nu_t$  can be evaluated in many different ways, ranging from algebraic relations and local equilibrium assumption to the solution of transport equations. The most popular approach is to express  $\nu_t$  as a "two-equation" model as a function of the turbulent kinetic energy  $k$  and its dissipation rate  $\varepsilon$  or specific dissipation  $\omega$ . Deriving these sets of equations two of the most famous models are formed:  $k - \varepsilon$  and  $k - \omega$ . A combination of the aforementioned models is the  $k - \omega$  SST model [5] used in this thesis.

### 2.3.2 $k - \omega$ SST Turbulence model

The  $k - \omega$  SST model is a combination of the  $k - \varepsilon$  and  $k - \omega$  models. The advantage of  $k - \varepsilon$  model is the low sensitivity of the flow field away from the wall on the boundary conditions, while it is lacking accuracy at high and adverse pressure gradients. On the other hand the  $k - \omega$  model is better at large and opposite pressure gradients. The disadvantage of the  $k - \omega$  model is high sensitivity to the far-field boundary conditions.

The combination of  $k - \varepsilon$  and  $k - \omega$  is so called  $k - \omega$  SST [4] model which has become very popular. Using the  $k - \omega$  formulation for boundary layer allows the application of this model without using damping functions. The model is switched to the  $k - \varepsilon$  behaviour far from the wall and thus avoids the common  $k - \omega$  problem [14].

A transport equation for turbulence kinetic energy  $k$  and the specific dissipation  $\omega$  in the model is as follows [5]:

$$\frac{\partial k}{\partial t} + \nabla \cdot (\mathbf{u}k) - \nabla \cdot ((\nu + \sigma_k \nu_t) \nabla k) = P_k - \beta^* \omega k, \quad (2.12)$$

$$\frac{\partial \omega}{\partial t} + \nabla \cdot (\mathbf{u}\omega) - \nabla \cdot ((\nu + \sigma_\omega \nu_t) \nabla \omega) = \alpha S^2 - \beta \omega^2 + 2\sigma_{\omega 2} (1 - F_1) \frac{1}{\omega} \nabla k \cdot \nabla \omega. \quad (2.13)$$

The kinematic Eddy Viscosity is:

$$\nu_T = \frac{a_1 k}{\max(a_1 \omega, SF_2)}. \quad (2.14)$$

The closure coefficients and auxiliary relations are:

$$F_1 = \tanh \left\{ \left\{ \min \left[ \max \left( \frac{\sqrt{k}}{\beta^* \omega y}, \frac{500\nu}{y^2 \omega} \right), \frac{4\sigma_{\omega 2} k}{CD_{k\omega} y^2} \right] \right\}^4 \right\}, \quad (2.15)$$

$$F_2 = \tanh \left[ \left[ \max \left( \frac{2\sqrt{k}}{\beta^* \omega y}, \frac{500\nu}{y^2 \omega} \right) \right]^2 \right], \quad (2.16)$$

$$P_k = \min (\tau : \nabla \mathbf{u}, 10\beta^* k \omega), \quad (2.17)$$

$$CD_{k\omega} = \max \left( 2\rho\sigma_{\omega 2} \frac{1}{\omega} \nabla k : \nabla \omega, 10^{-10} \right), \quad (2.18)$$

while closure coefficients have values presented in Table 2.1

**Table 2.1:**  $k - \omega$  SST turbulence model coefficients.

$\alpha_1$	$\alpha_2$	$\beta_1$	$\beta_2$	$\alpha_{k1}$	$\alpha_{k2}$	$\gamma_{\omega 1}$	$\gamma_{\omega 2}$	$\beta^*$
$\frac{5}{9}$	0.44	$\frac{3}{40}$	0.0828	0.85	1	0.5	0.856	$\frac{9}{100}$

Unlike the coefficients used in model equations ( $\alpha, \beta, \alpha_k, \alpha_\omega$ ), closure coefficients subscripted with 1 or 2, have a defined value.

The first three terms from the left in Eq. (2.12) and Eq. (2.13) are the temporal derivative, convection and diffusion term. On the right side of this equation there are many source and sink members which point to a stronger local character of this partial differential equations. Values of the coefficients used in the equations are calculated using the blending function  $F_1$ :

$$\chi = \chi_1 F_1 + \chi_2 (1 - F_1), \quad (2.19)$$

where  $\chi$  is the coefficient that is used in model equation, while  $\chi_1$  and  $\chi_2$  stand for closure coefficients.  $y$  in Eq. (2.15) and Eq. (2.16) represents the distance from the wall [5].

### 2.3.3 Large Eddy Simulation

In LES turbulence coherent structures and large-scale turbulence will be simulated, while the small-scale effects will be modelled. For this purpose, the Governing turbulence equation needs to understand scale, which is achieved using equation filtering. For filtering, Navier-Stokes Equations averaging equation is mathematically defined as [2]:

$$\bar{\mathbf{u}} = \int G(\mathbf{x}, \mathbf{x}') \mathbf{u}(\mathbf{x}') d\mathbf{x}', \quad (2.20)$$

where  $G(\mathbf{x}, \mathbf{x}')$  is the localized filter function, which after filtering Navier-Stokes Equations (Eq. (2.2) and Eq. (2.3)) produces equation set very similar to RANS with a considerably difference:

$$\frac{\partial \bar{\mathbf{u}}}{\partial t} + \nabla \cdot (\bar{\mathbf{u}}\bar{\mathbf{u}}) - \nabla \cdot (\nu \nabla \bar{\mathbf{u}}) = -\nabla \bar{p} + \nabla \cdot \boldsymbol{\tau}, \quad (2.21)$$

$$\nabla \cdot \bar{\mathbf{u}} = 0, \quad (2.22)$$

where the last term  $\boldsymbol{\tau}$  is defined as:

$$\boldsymbol{\tau} = \underbrace{(\bar{\mathbf{u}}\bar{\mathbf{u}} - \bar{\mathbf{u}}\bar{\mathbf{u}})}_{\text{Leonard stress}} + \underbrace{(\bar{\mathbf{u}}\mathbf{u}' + \mathbf{u}'\bar{\mathbf{u}})}_{\text{cross term}} + \underbrace{\bar{\mathbf{u}'\mathbf{u}'}}_{\text{backscatter}}, \quad (2.23)$$

- The Leonard stress represents the interaction between two resolved scale eddies to produce small scale turbulence,
- The Cross term describes the interaction between resolved and small scale eddies and can transfer energy in either direction but usually follows the energy cascade,
- The Backscatter represents energy transfer from small to large scales.

Implicit filtering for separation between resolved and unresolved scales depends on mesh resolution. Typical models for Sub-Grid Scale (SGS) which are used are of Smogorinsky model type, with fixed or dynamic coefficients. For LES most of the models work very well, where it is most important to remove the correct amount of energy from resolved scales. In this thesis, the One Equation Eddy Viscosity Model for incompressible flows is used. Eddy viscosity SGS model using a modelled balance equation to simulate the behaviour of turbulent kinetic energy  $k$  [7].

## 2.4 Boundary Conditions

In order for a system of partial differential equations to have a unique solution, it needs to have defined boundary conditions. The role of boundary conditions is to isolate the system from its surroundings [2]. Prescribing boundary conditions requires an understanding of the investigated problem. Generally, boundary conditions can be classified as either numeric or physical boundary conditions. Physical boundary conditions depend on the domain form and are assigned to the characteristic part of a domain boundary. Typical physical boundary conditions used in CFD cases are wall, inlet and outlet. Numerical boundary conditions are imposed at the equation level. They can be classified into:

- Dirichlet boundary condition, which sets a fixed value for the transported variable  $\phi$  on the specified boundary,
- Von Neumann boundary condition specifies the fixed gradient or fixed flux condition of the transported scalar variable  $\phi$  normal to the boundary,
- Mixed boundary condition is a boundary condition that represents a linear combination of the Dirichlet and Von Neumann boundary condition.

Commonly, Dirichlet and von Neumann numerical boundary conditions are used in pair on the same boundary in order to solve Navier-Stokes equations. For example, if the velocity at the inlet is prescribed with a Dirichlet (fixed value) boundary conditions, a von Neumann boundary condition (zero gradient, no flux) is prescribed for the pressure on the same boundary. Additionally, if velocity at the outlet boundary is assigned with a von Neumann boundary condition, then the pressure at the same boundary will be assigned with the Dirichlet boundary condition.

For turbulent flows, the inlet and outlet boundary conditions on turbulence variables ( $k$  and  $\omega$ , for example) are typically assigned to fixed value and zero gradient. The boundary conditions for the turbulence properties on the wall depend on the form of the selected turbulence model and the near-wall treatment [15].

## 2.5 Closure

In this section, an entire CFD mathematical model for solving transient, incompressible, viscous and turbulent flow is presented. Since the realistic fluid flow is turbulent, in this thesis two turbulence models are tested (RANS and LES). To model Reynolds stresses within the RANS approach, a Boussinesq hypothesis of eddy viscosity is introduced along with the  $k - \omega$ SST turbulence model, while for LES approach SGS model for the small eddies is used.

## 3 Influence of wind on engineering structures

### 3.1 Introduction

Buildings, offshore structures and other similar structures must be able to withstand external loads imposed by nature or at least reduce the disastrous damage of natural force to an acceptable limit. Accurate evaluation and prediction of wind loads is very important in reducing the adverse effects of wind on objects. The most important aspect in studying the wind flow around an object is the mean velocity profile of the wind. There are several different approaches to studying the problem of wind impact on objects [6].

- measurements in real-time and on real objects,
- wind tunnel measurements,
- semi-empirical models,
- Computational Fluid Dynamics (CFD).

Test on real objects provide the most complete data, including complexity of occurrence within the Atmospheric Boundary Layer (ABL). The problem is controlling weather conditions which have an important impact for measuring. Further, results obtained by measuring on already executed objects can be used essentially on similar objects that are planned to be built in the future. Testing performed in wind tunnel allow physical modelling of real problem on smaller models. However, wind tunnel testing is time consuming, very expensive and has problems with modelling of the boundary layer and various scaling issues related to similarity across multiple dimensionless groups. Semi-empirical models usually used in practice are Gauss model and the ASHRE model [6]. They are relatively easy to use, however they have limited applicability and accuracy. An additional advantage of CFD is the known flow characteristic throughout the entire domain, but its disadvantages are turbulence modelling, limited close to the wall accuracy and limited computer resources.

### 3.2 Atmospheric Boundary Layer (ABL)

ABL presents the part of the troposphere within which the airflow structure is formed in direct interaction with the surface of Earth. Because of friction, value of velocity on the substrate is zero and grows to the maximum at the edge of the boundary layer, as shown in Figure 3.1.  $\delta$  represent thickness of ABL, while  $U_\delta$  represent velocity value on the edge of the ABL. The parameter values that characterize the turbulent structure of the boundary layer are maximum near the substrate and decrease with increasing the distance from the substrate.



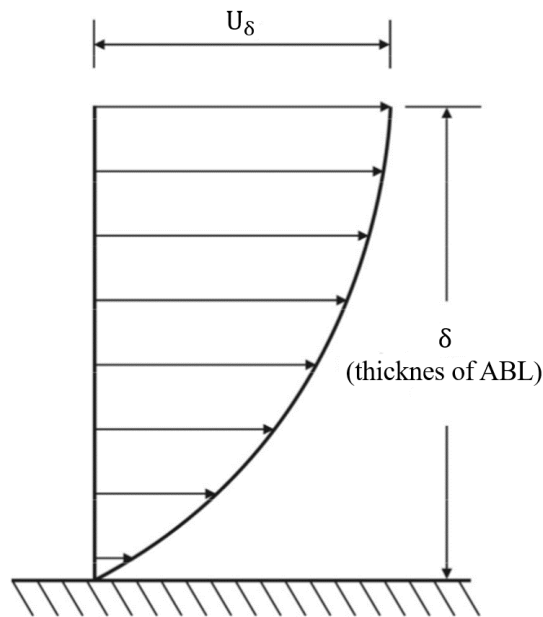


Figure 3.1: Atmospheric boundary layer [6].

The ABL characteristic vary with the conditions of the outfield considered therefore are several types of fields which in turn produce boundary layers of different shapes and thickness as seen in Figure 3.2. Here,  $z_0$  represent aerodynamic roughness length,  $\delta$  represent thickness of ABL and  $\alpha$  is the exponent of power law.

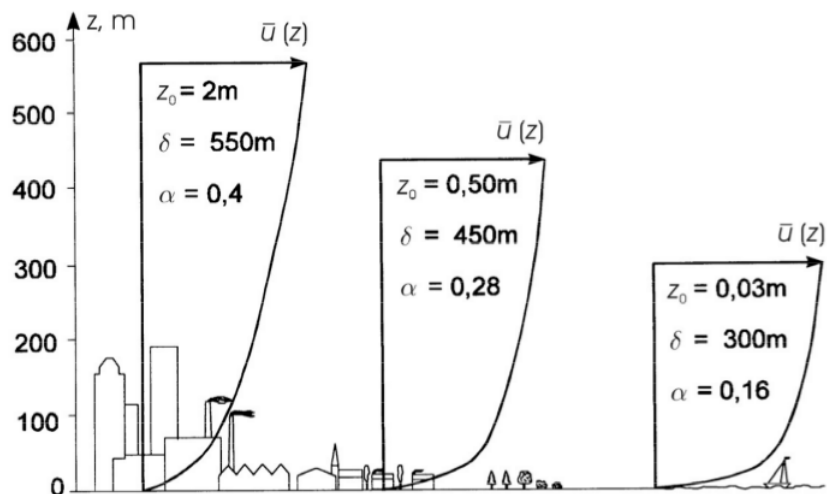


Figure 3.2: Different types of wind profiles [6].

In order to compare wind tunnel measurements and CFD approach it is necessary to define ABL which will be used for the velocity profile. For ABL wind profile given in following Eq. (3.1) the target is a  $\pm 2.5\%$  error band in CFD, which is similar to requirements for wind tunnel [1]:

$$U(z) = U_0 \left[ 1 + C \cdot \ln \left( \frac{z}{z_{ref}} \right) \right], \quad (3.1)$$

$$C = 0.0573 \cdot (1 + 0.15 \cdot U_0)^{\frac{1}{2}}, \quad (3.2)$$

where  $U(z)$  is the target wind profile in m/s,  $z_{ref} = 0.04167$  m is the reference height (model scale), and  $U_0 = 100$  knots = 51.444 m/s is the design velocity for the wind load evaluation at the reference height [1].

### 3.3 Distribution of pressure caused by wind load

The influence of wind force on objects that are not prone to vibration is proportional to the square of velocity. When wind blows into the object, there is a characteristic distribution of pressure. Figure 3.3 shows pressure distribution when wind blows on a cube. On the overflowing surface maximal value of pressure is at about 85 % of overall object height. Approaching to the bottom value of pressure drops. Near the substrate pressure value again grows. On the back side there is a pressure generated by flow separation. On the bottom surface there is a characteristic distribution of pressure. The ground plan also shows specific distribution of the pressure generated by the wind.

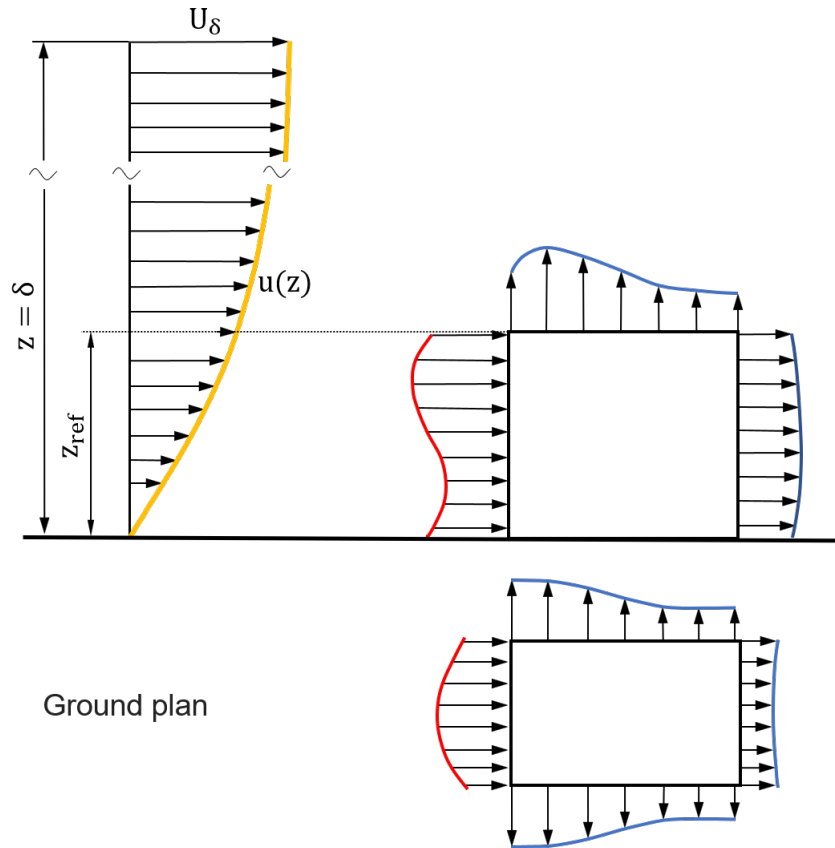


Figure 3.3: Pressure distribution on cube [6].

### 3.4 Closure

In this section several different approaches for studying the problem of wind impact on objects are described. Since the ABL has a huge influence, examples of appearance of boundary layers are given depending on the environment. Due to its importance with respect to pressure loads, ABL profiles are given and explained. At the end, the distribution of pressure on a cubic model is shown.

## 4 Geometry and Numerical Domain

### 4.1 Introduction

The first part of this section introduces CAD model of HOE PC-Semi submersible platform and two models that are geometrically identical to the models tested in the wind tunnel. The first model is constructed without the derrick and in the following text it is referred to Test D. The second model is without the derrick, flare boom, crane 1, living quarters and helideck, it is referred to as Test J. After introducing the geometrical characteristics of Test D and Test J, the process of creating a numerical mesh for a single model is described.

### 4.2 HOE PC-Semi Submersible Platform Models

Figure 4.1 show full model of HOE's PC-Semi submersible platform Model in 1 : 200 scale ratio. All removable parts are indicated.

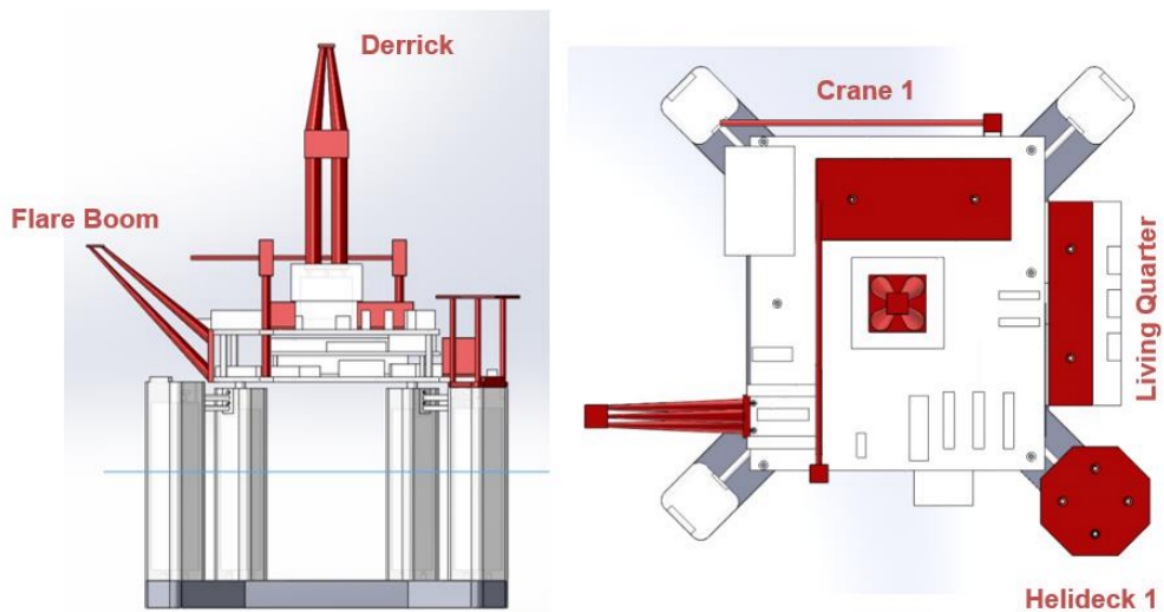
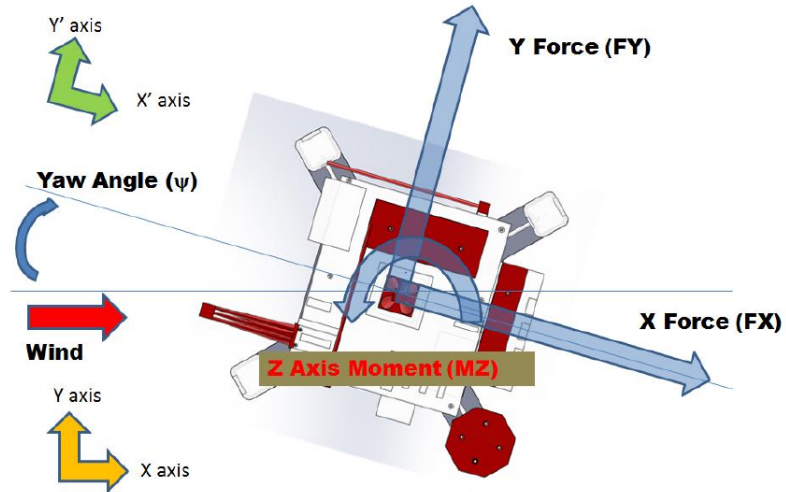


Figure 4.1: HOE PC-Semi submersible platform full model [1].

The coordinate system associated with this CAD model is the body-fixed coordinate system as shown in Figure 4.2. All forces/moments values should be reported in wind coordinate system ( $X - Y$ ). A yaw angle of 135 degrees is simulated in Test J and Test D which orients the helideck in the upwind direction. The system origin is at the center of the columns with  $z = 0$  at the water level.



**Figure 4.2: Coordinate systems of the model [1].**

Figure 4.3 and Figure 4.4 show two separate Computer Aided Design (CAD) models used in Test D and Test J, respectively. Model used in Test D differs from the full model because the derrick is removed. The second model, used in Test J does not contain derrick, flare boom, crane 1, living quarters and helideck. These CAD models are used for mesh generation, where the process of meshing is explained in more detail in the next chapter.

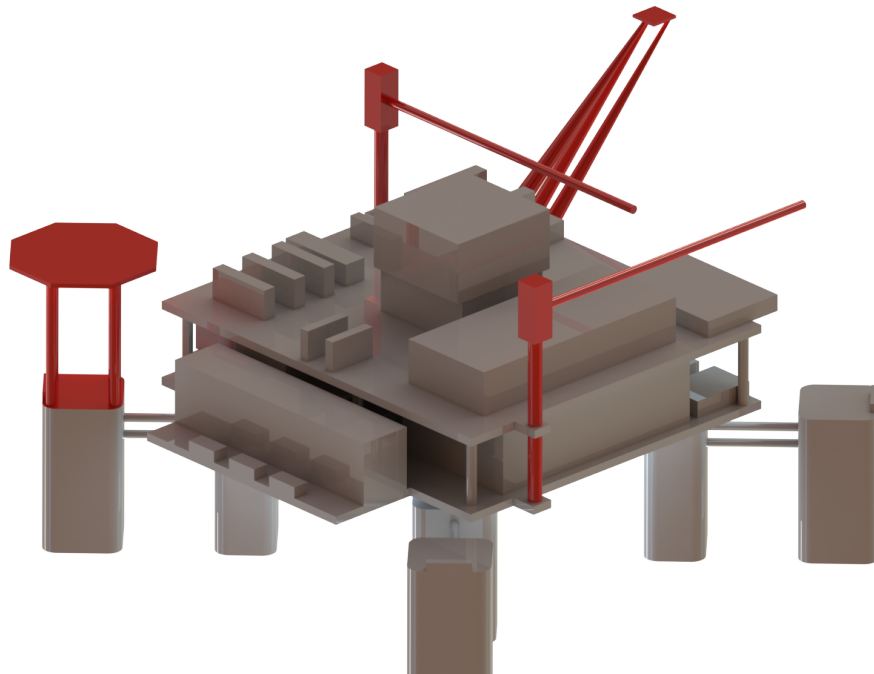


**Figure 4.3: HOE PC-Semi submersible platform Test D model.**

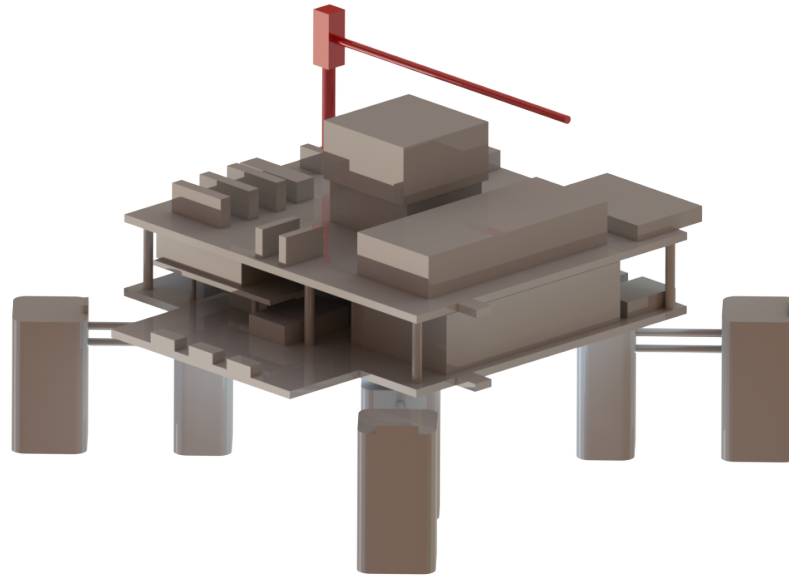


**Figure 4.4: HOE PC-Semi submersible platform Test J model.**

### 4.3 Computational mesh

Spatial domain discretization has a significant influence on the result of a CFD simulation. Spatial domain must be discretized in such a way that it can capture all the relevant flow phenomena. There are three types of numerical mesh. It can be structured or unstructured, or a combination of the two, a hybrid mesh. Constructing a structured mesh is more time consuming than constructing an unstructured mesh. Sometimes, due to complex geometry, it is impossible to construct a fully structured mesh. Unstructured meshes usually have more cells than structured meshes which causes higher computational demands.

Based on the generated full CAD model obtained from SNAME OC-8 Comparative Wind Load Study, *SolidWorks* program package was used to removed parts for Test J and Test D [10]. Generated CAD model was afterwards exported to .stl format to be used by the meshing software. Using this models hybrid meshes are created, meaning that part of it is structured (made of hexahedral volumes) and the rest is unstructured (made of tetrahedral volumes). The mesh is generated with software *cfMesh* [11]. *CfMesh* is a cross-platform library for automatic mesh generation that is build on top of *foam-extend*.

In Figure 4.5 HOE PC-Semi submersible platform Test D model case topology is presented with the assigned boundary numbers. Corresponding boundary numbers which represent boundaries of the generated geometry and numerical domain are presented in the Table 4.1.

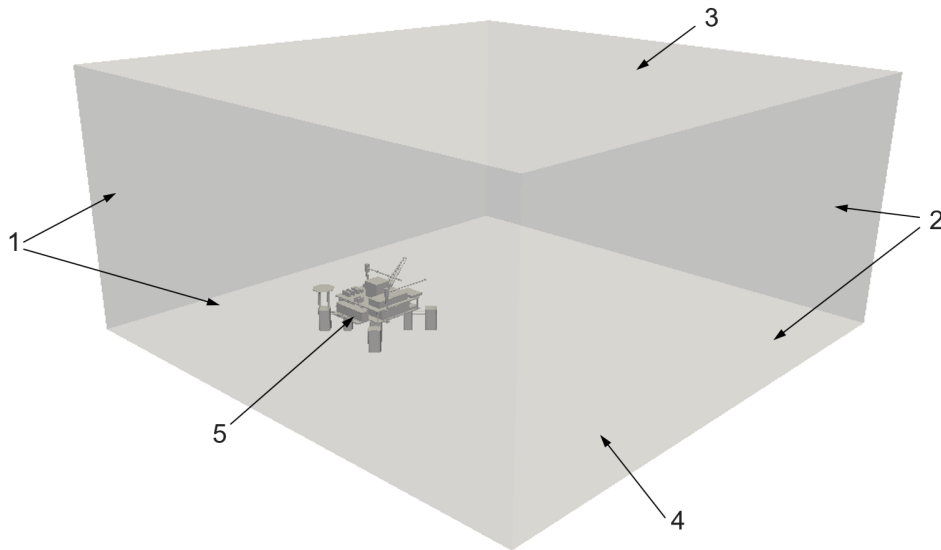


**Figure 4.5: Assigned patch ID numbers on Test D.**

**Table 4.1: Definition of patch topology for Test D.**

Boundary No.	Boundary
1	inlet
2	outlet
3	lowerWall
4	top
5	model

In order to generate the mesh with *CfMesh* it is necessary to set basic parameters such as maximum cell size, refinement at the surface, refinements of certain parts and thickness of the boundary layer.

Figure 4.6 shows the mesh generated for Test D. In Figure 4.7, a cross-section in the  $x-z$  plane is shown, where the transition from finer to coarser mesh is visible. Numbers of layers along the wall boundary is 5 and this part of the mesh is structured. At the transition between finer and coarser regions unstructured mesh is used. As there are no major differences in the geometry between Test D and Test J, the process of mesh generation is the same. Figure 4.9 shows the generated mesh for Test J, where it is apparent that the mesh is very similar.

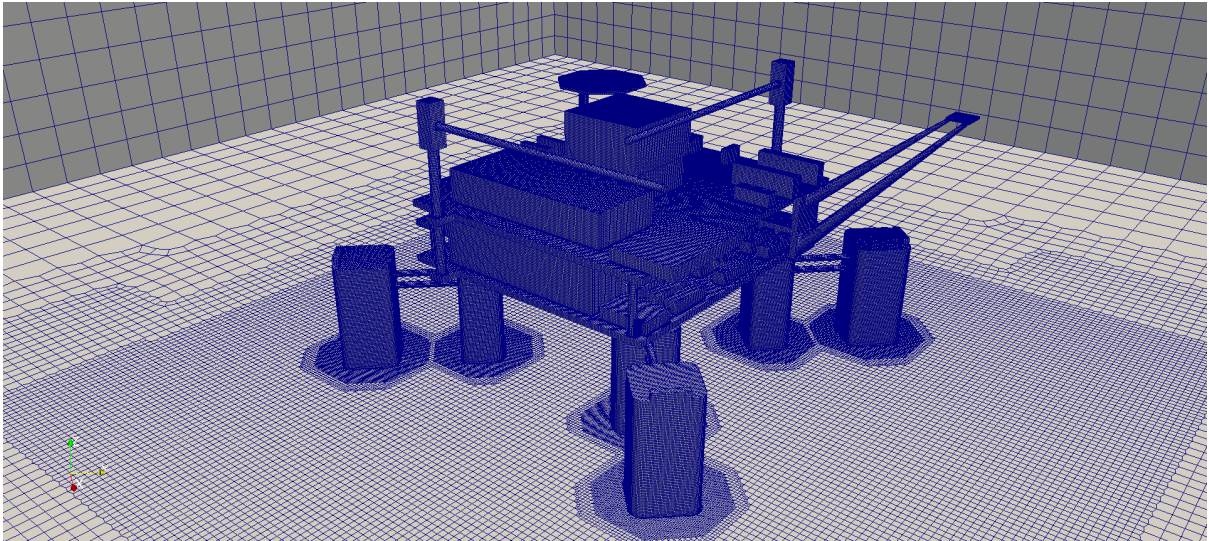


**Figure 4.6: Surface mesh discretization for Test D.**

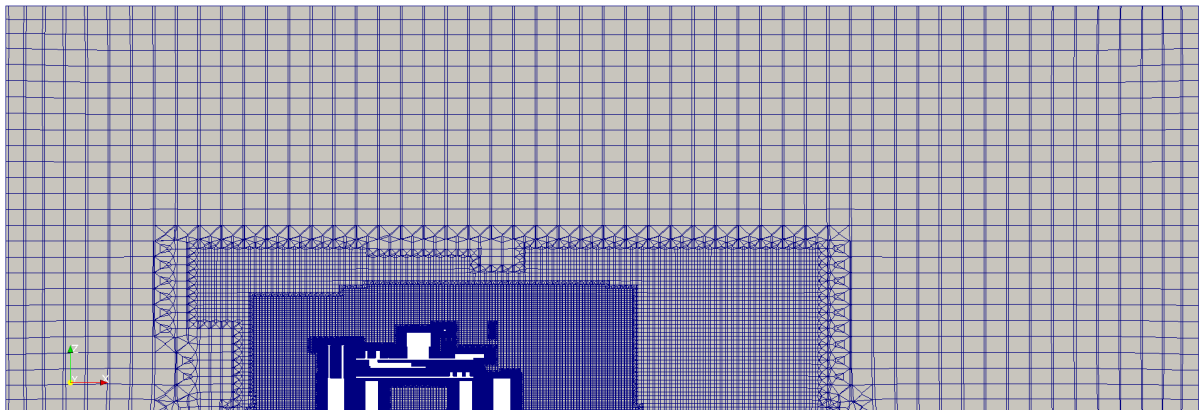


**Figure 4.7: x-z slice of mesh for Test D.**

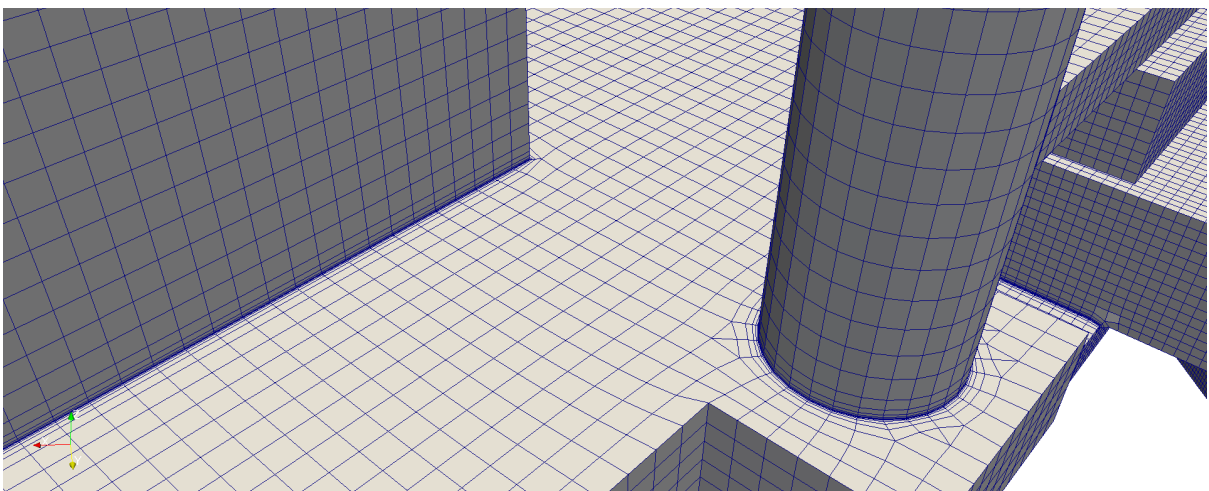


**Figure 4.8: View of the layer refinement.**

The mesh is created in an attempt to reach the compromise between simulation accuracy



and computational time. The total number of cells for Test D is 8 826 740 and their breakdown by topology is given in Table 4.2, while Test J mesh topology is given in Table 4.3, where and the total number of cells is 7 960 877.

**Table 4.2: Test D mesh topology.**

<b>Number of cells</b>	
Hexahedra	8 602 872
Prisms	15 540
Pyramids	14 303
Tetrahedra	10 970
Polyhedra	183 055
<b>Total</b>	<b>8 826 740</b>

**Table 4.3: Test J mesh topology.**

<b>Number of cells</b>	
Hexahedra	7 764 173
Prisms	13 306
Pyramids	12 803
Tetrahedra	9 538
Polyhedra	161 057
<b>Total</b>	<b>7 960 877</b>

Quality assessment of the generated mesh is evaluated using the checkMesh tool in foam-extend. The output for Test D is presented in Table 4.4 and for Test J in Table 4.5.

**Table 4.4: Test D mesh quality.**

<b>Parameter</b>	<b>Average</b>	<b>Maximum</b>	<b>Treshold</b>
Aspect ratio	-	136.17	-
Skewness	-	6.06	4
Non-ortagonality	4.25	83.39	70

**Table 4.5: Test J mesh quality.**

<b>Parameter</b>	<b>Average</b>	<b>Maximum</b>	<b>Treshold</b>
Aspect ratio	-	132.5	-
Skewness	-	3.88	-
Non-ortagonality	4.07	85.03	70

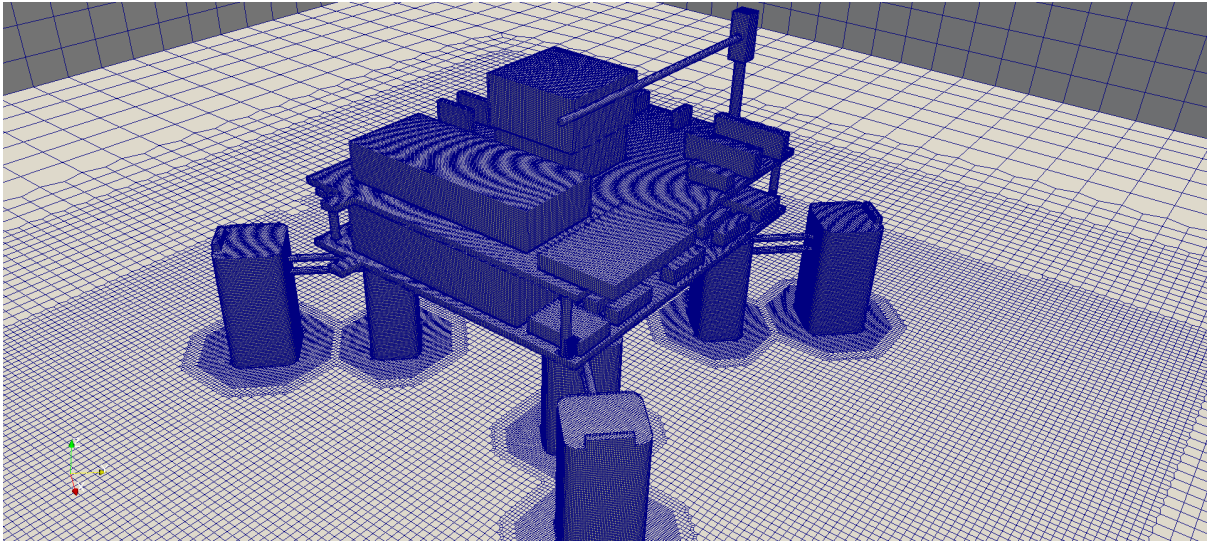


**Figure 4.9: Surface mesh discretization for Test J.**

#### **4.4 Closure**

This section presents the overview of required preprocessing steps for numerical simulation. First, the HOE's PC-Semi submersible platform full and stripped study CAD models are presented, which are obtained from SNAME OC-8 Comparative Wind Load Study. After presenting the geometry, the method of spatial discretization of the mentioned geometry is described. As the models for Test D and Test J have no big differences in geometry, details of the mesh are shown only for Test D, while basic information about the mesh quality are presented in the corresponding tabular form for both cases.

## 5 Numerical Results

### 5.1 Introduction

In this chapter, a comparison is made between computer simulations and experimental values obtained by wind tunnel measurements. There are four different simulations: two different models, Test D and Test J, where two turbulence models are used for both, RANS and LES.

This chapter is divided into seven sections. In the first section, the boundary conditions used in simulations are presented. Next, the setup that is used for simulations is shown. Comparison of atmospheric boundary layer obtained from CFD simulations and prescribed velocity profile is presented in the following chapter. The second and third section contain the results of the Test D for both of turbulence models with convergence graphs and distributions of velocity and pressure. The fourth section contains the results for specific values such as turbulent kinetic energy and flow separation. In the last section the force and moment coefficients for all cases and comparison to the experimental results are presented.

### 5.2 Boundary Conditions

In order to solve the set of partial differential equations for fluid flow, it is necessary to set boundary conditions for each solved physical quantity on each boundary of the numerical domain. Boundaries are listed in Table 4.1, while the role of boundary conditions are described in Subsection 2.4. In this subsection, the type of boundary condition for each physical variable and each boundary are described and listed in Table 5.1.

Due to the same boundary conditions being used for Test D and Test J, only the boundary conditions for Test D are shown. The Dirichlet boundary condition, which is set on the inlet of the domain, defines the constant value of velocity. To achieve the desired wind profile according to the ABL presented in Subsection 3.2, velocity inlet boundary condition is set with `groovyBC` special boundary condition. This boundary condition is basically a mixed boundary condition where values can be specified using functions. It can be used to set a non-uniform boundary condition without additional programming [16]. The value of velocity in  $x$  direction is set according to Eq. (3.1). The constant velocity boundary condition is also set on the `lowerWall` and the `model`, defining them as the stationary parts. The velocity at the outlet is defined by the `InletOutlet` boundary condition. It switches between the von Neumann boundary condition when the fluid flows out of the domain at the boundary, and the Dirichlet when the fluid is flowing into the domain. The velocity at the top is defined with `slip` boundary condition. It uses Dirichlet boundary condition with a zero velocity in normal direction and von Neumann boundary condition in tangential direction. Following a common practice for incompressible simulations, the pressure on the outlet is set to a fixed value of 0 Pa.

In RANS turbulence model, boundary condition for turbulent kinetic energy  $k$  is set to `kqRWallFunction` on the `model` and `lowerWall`, while boundary condition for specific dissipation rate  $\omega$  is set to `omegaWallFunction`.

In simulations with LES turbulence model, Dirichlet boundary condition is set on the wall type boundaries for SGS kinetic energy  $k$ . SGS viscosity `nuSgs` and stress tensor `B` turbulence properties use von Neumann boundary condition on wall type boundaries.

**Table 5.1: Imposed boundary condition for simulations.**

Boundary	Velocity boundary condition	Pressure boundary condition
inlet	groovyBC	von Neumann
outlet	InletOutlet	Dirichlet
lowerWall	Dirichlet	von Neumann
top	slip	von Neumann
model	Dirichlet	von Neumann

### 5.3 Simulation Setup

The influence of wind is simulated using the unsteady solver `pimpleFoam` from `foam-extend`. In order to get convergence of results in shortest possible time, flow solution is first initialized with `potentialFoam` solver and then with steady-state `simpleFoam` solver. The `pimpleFoam` solver is based on the PIMPLE algorithm for pressure velocity coupling in unsteady flows [17].

The Courant number ( $Co$ ) is defined with computational cell size, fluid velocity and the simulation time-step [17]. If  $Co > 1$  the particle moves through one or more cells in each time step. On the other hand, if  $Co < 1$  in each time step, the particles move less than in one time-step. In a transient simulation it is desirable to keep the Courant number as low as possible (ideally around  $Co = 1$ ). Courant number decreases with the decreasing time-step which directly affects the computational time. Thus, time-step should be defined so that the simulation can be performed correctly within a reasonable time. Using a solver based on implicit PIMPLE algorithm allows higher Courant numbers in simulations, so the time step can be increased [17]. In this work the time-step is automatically adjusted in order to be  $Co < 5$ .

The discretization methods for mathematical operators used in simulations are present in Table 5.2. For time derivative terms first order implicit bounded discretization is used for both of turbulence models. Second order convection discretization is used second order, unbounded discretization, while for convection divergence terms in turbulence model equations first-order bounded method is used. Other convection divergence terms are discretized with second order, upwind-biased, unbounded scheme. All diffusion terms for discretization use second order,

unbounded method.

**Table 5.2: Discretization methods in foam-extend for RANS and LES turbulence models.**

Mathematical Operator	Discretization Method
Temporal	Euler
Convection	Gauss upwind / Gauss linear
Diffusion	Gauss linear corrected

The pressure equation is solved with the Geometric agglomerated algebraic multigrid solver for linear solving. The biconjugate gradient stabilized method [2] is used for all equations.

## 5.4 Comparison of Atmospheric Boundary Layer

This subsection shows the comparison of inlet velocity profile obtained from CFD simulations and required velocity profile described in the Section 3.2. The velocity profile is compared at 5 different locations in the domain which are shown in Figure 5.1. Line 1 is located at the inlet boundary. Line 2, line 3 and line 4 are gradually approaching the model and they are in different refinement regions. Line 5 is located in the undisturbed flow away from the model.

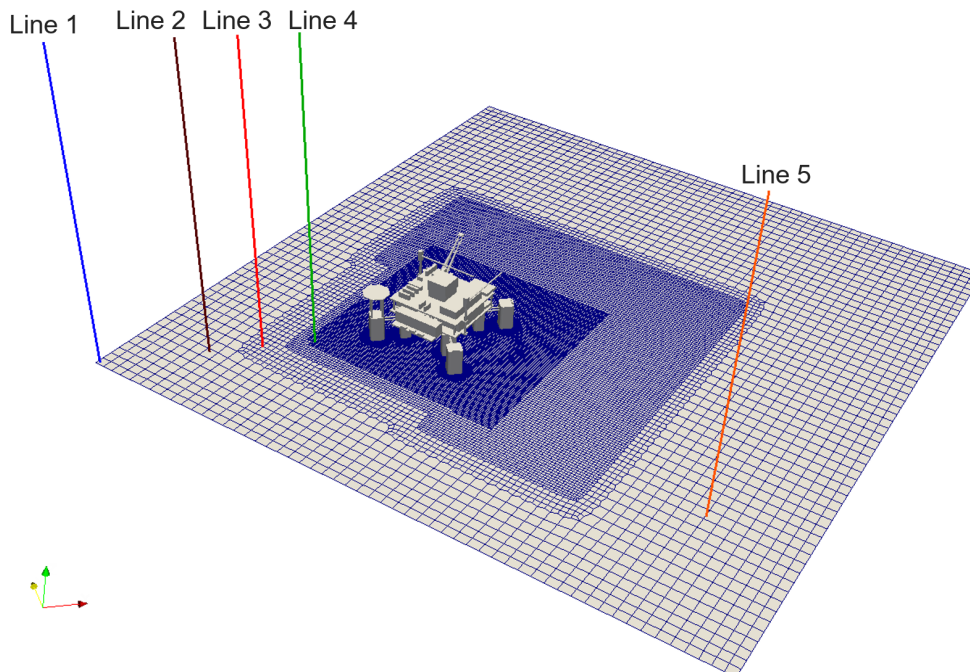


**Figure 5.1: Location of lines for sampling of velocity profiles.**

On Figure 5.2 a comparison of the inlet velocity profile between RANS and LES turbulence models and the target velocity profile is shown.  $x$  axis denotes velocity while  $y$  axis denotes the vertical position. Boundary conditions for inlet velocity are equal for both turbulence models.

The difference between the target and CFD velocity profile appears in the lower section of profile. The difference is due to a relatively coarse mesh in this section with respect to the high velocity gradient. In the upper section of the ABL the velocity profiles fit well but CFD velocity profile has an exception in the edge of refinement.

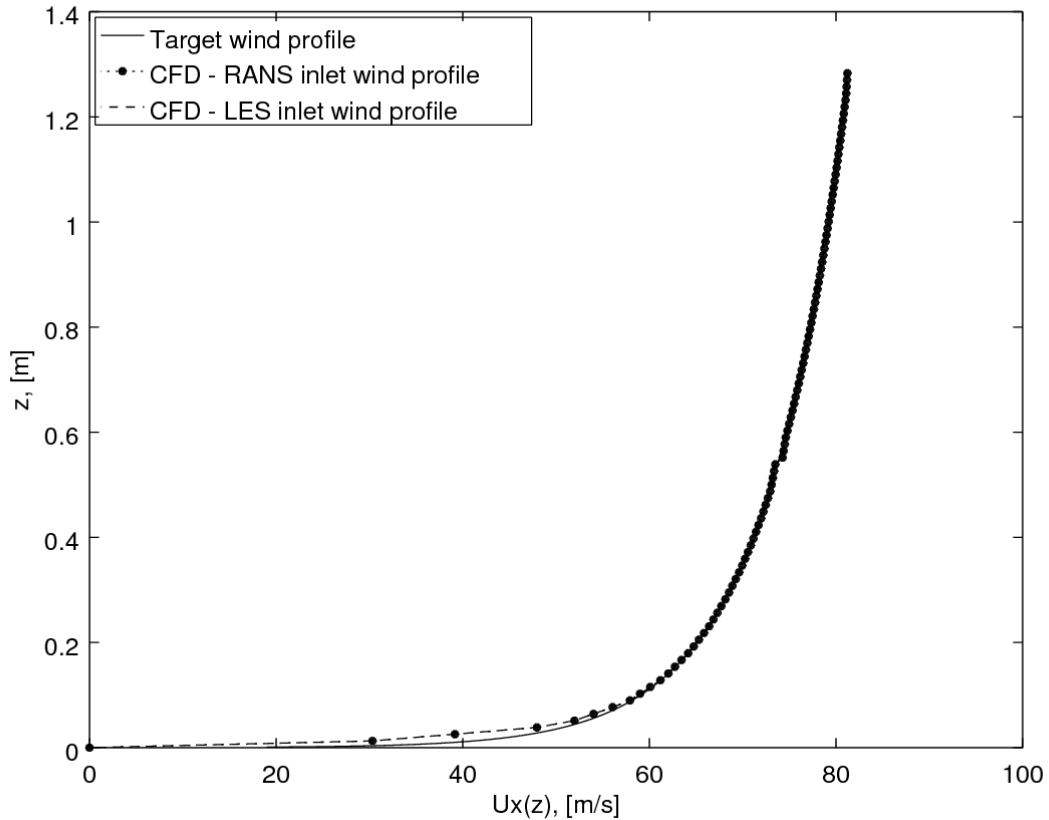


**Figure 5.2: Comparison of the inlet velocity profile with the requested velocity profile.**

Figure 5.3 shows velocity profiles on different domain sections obtained from simulation using RANS turbulence model, where it can be seen that in the lower section velocity profiles deviate from the target profile. Moving away from the inlet towards the model, profiles at Line 3 and Line 4 are significantly different because of the transition from the coarse to finer mesh. LES turbulence model is more sensitive to mesh quality so velocity profiles have bigger deviations which are shown on the Figure 5.4.

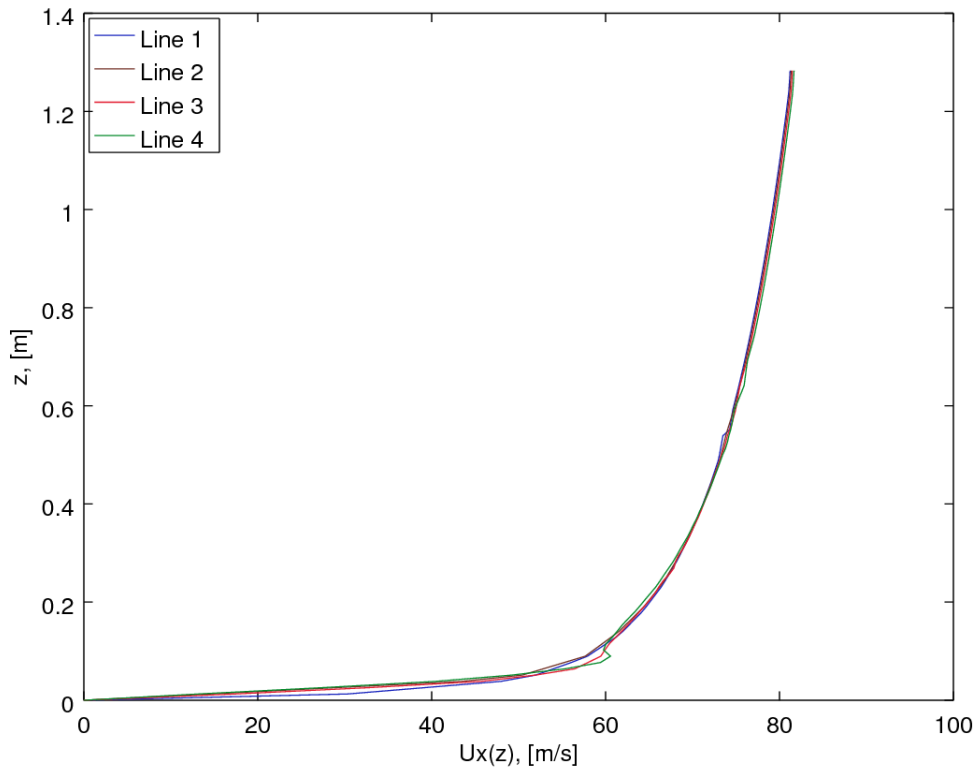


**Figure 5.3: Velocity profile comparison in the model vicinity with a RANS turbulence model.**

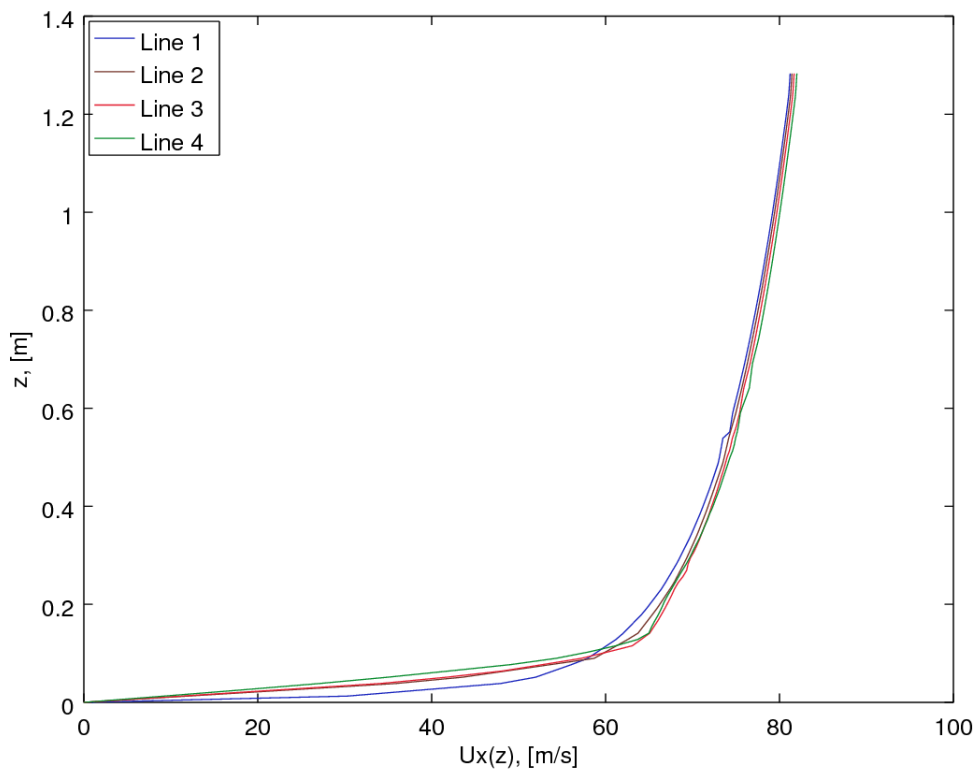


**Figure 5.4: Velocity profile comparison in the model vicinity with a LES turbulence model.**

Velocity profiles in undisturbed flow are presented in Figure 5.5. The appearance of the velocity profile in undisturbed flow for RANS turbulence model is very similar to inlet velocity profile. Small differences appear in the lower section because of the relatively coarse grid. Undisturbed velocity profile obtained in simulations with LES turbulence model significantly deviates from inlet velocity profile and the reason is that the LES turbulence model is more sensitive to mesh quality.

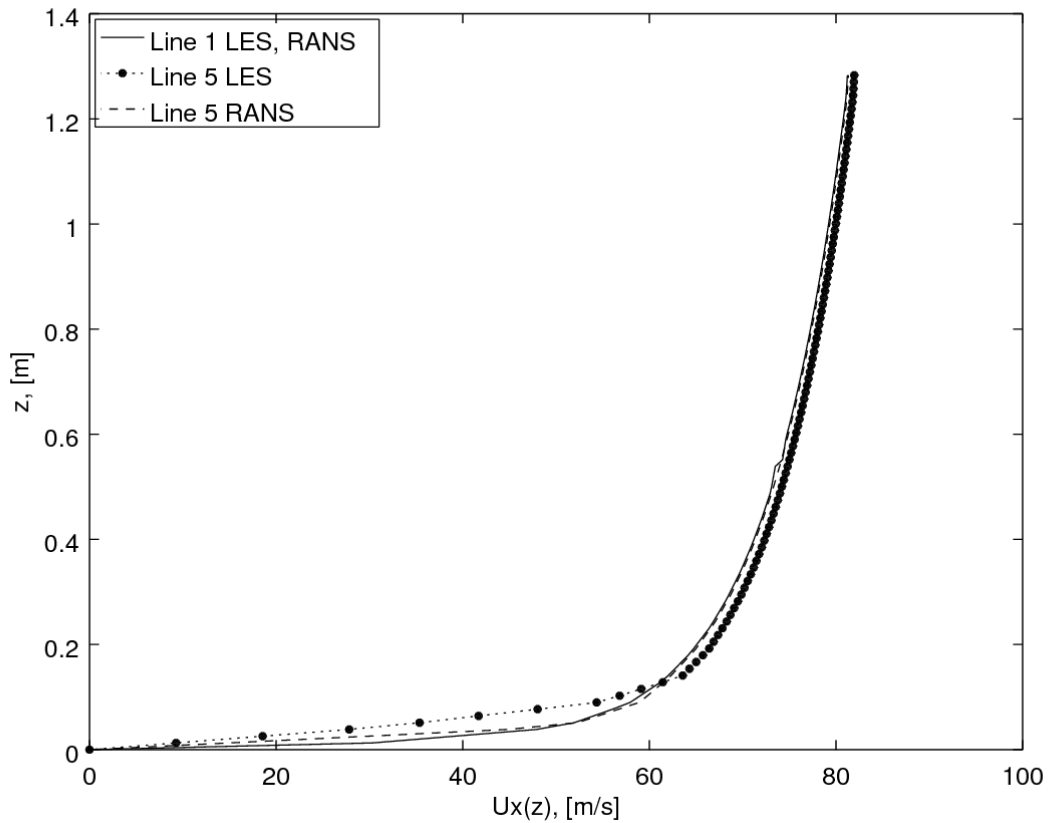


**Figure 5.5: Velocity profile comparison in undisturbed flow.**



## 5.5 Test D results

This section presents the results of simulations for the stripped HOE PC-Semi submersible platform model Test D for the two turbulence models. As mentioned above, Test D is a stripped model without the derrick. All forces and moments values are reported in wind coordinate system, which is the global coordinate system. Body fixed coordinate system is rotated by 135 degrees with respect to the wind coordinate system. For such a coordinated system, the helideck is oriented in the upwind direction.

Figure 5.6 shows the graph of the force history convergence in time for the unsteady solver with RANS turbulence model. Considering that the flow is in direction of the  $x$  axis, the force value in that direction is dominant. Force oscillation is significant with respect to the total force and on the deviations from the experimental values. Figure 5.7 shows the graph of the force convergence for LES turbulence model. The force value computed with LES turbulence model is higher than the force obtained by determining the RANS turbulence model.

In the simulation with RANS turbulence model, the relative amplitude of oscillation of the upwind force  $F_x$  is 3 %, while in the simulation with LES turbulence model the relative amplitude of oscillation of the upwind force  $F_x$  drops to 1.4 %. The force in  $y$  axis direction is perpendicular to flow direction and has no significant effect on the total force.

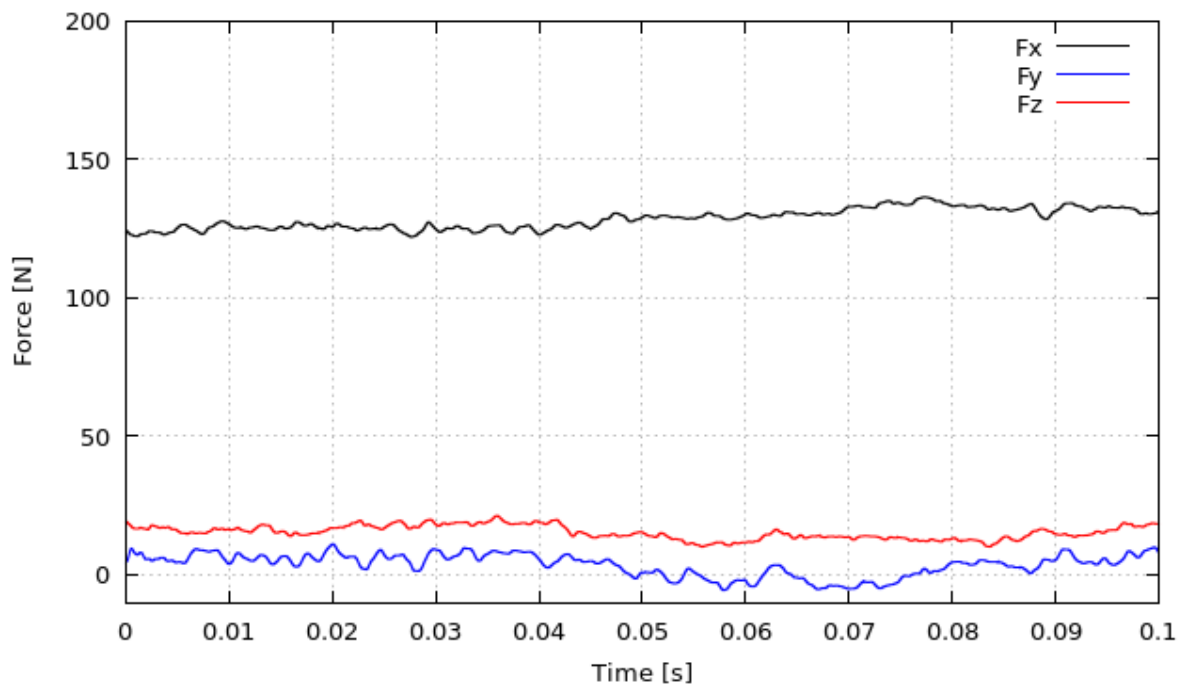
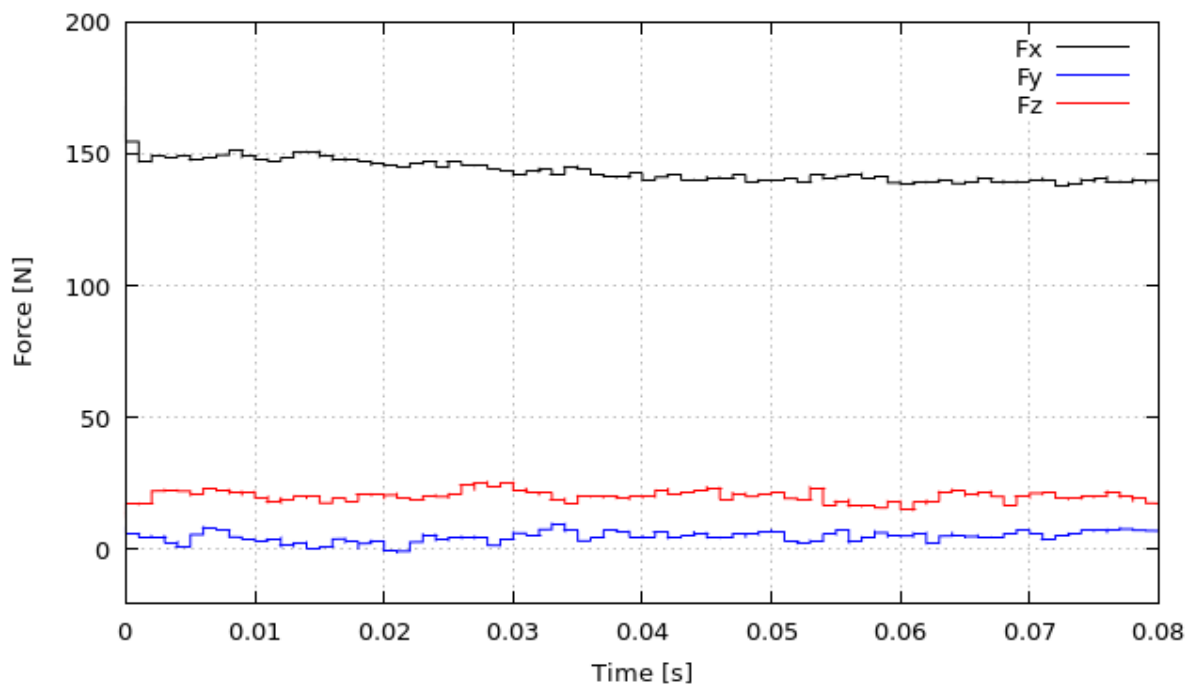


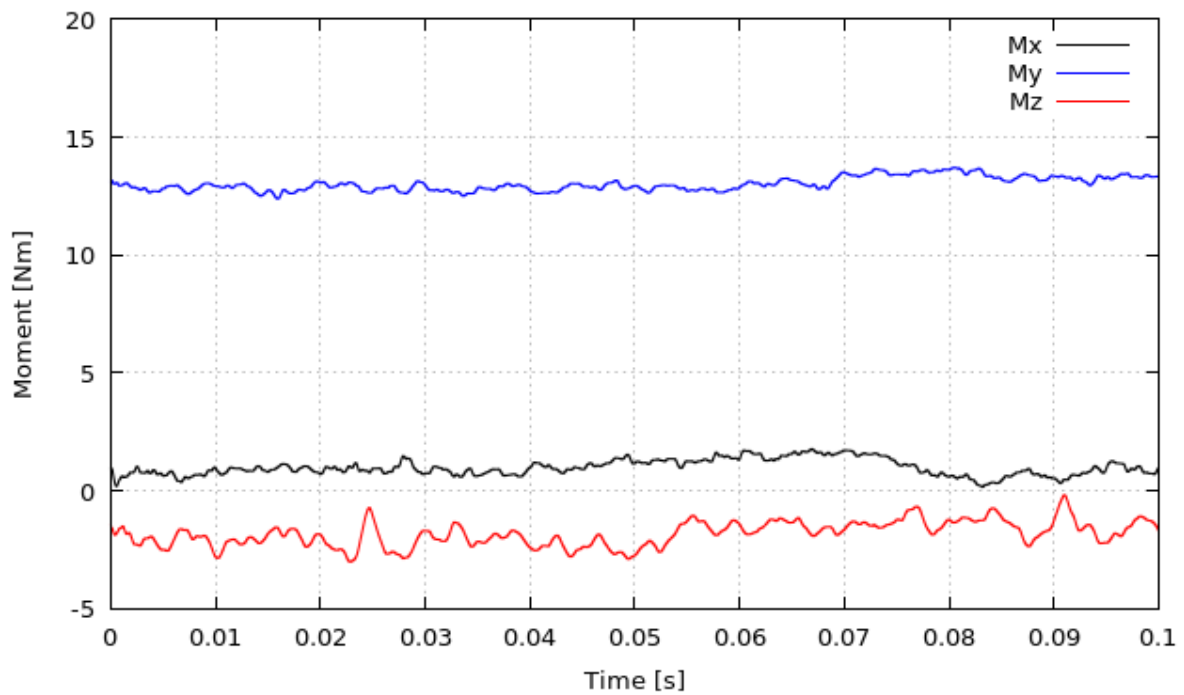
Figure 5.6: Test D force convergence with RANS turbulence model.



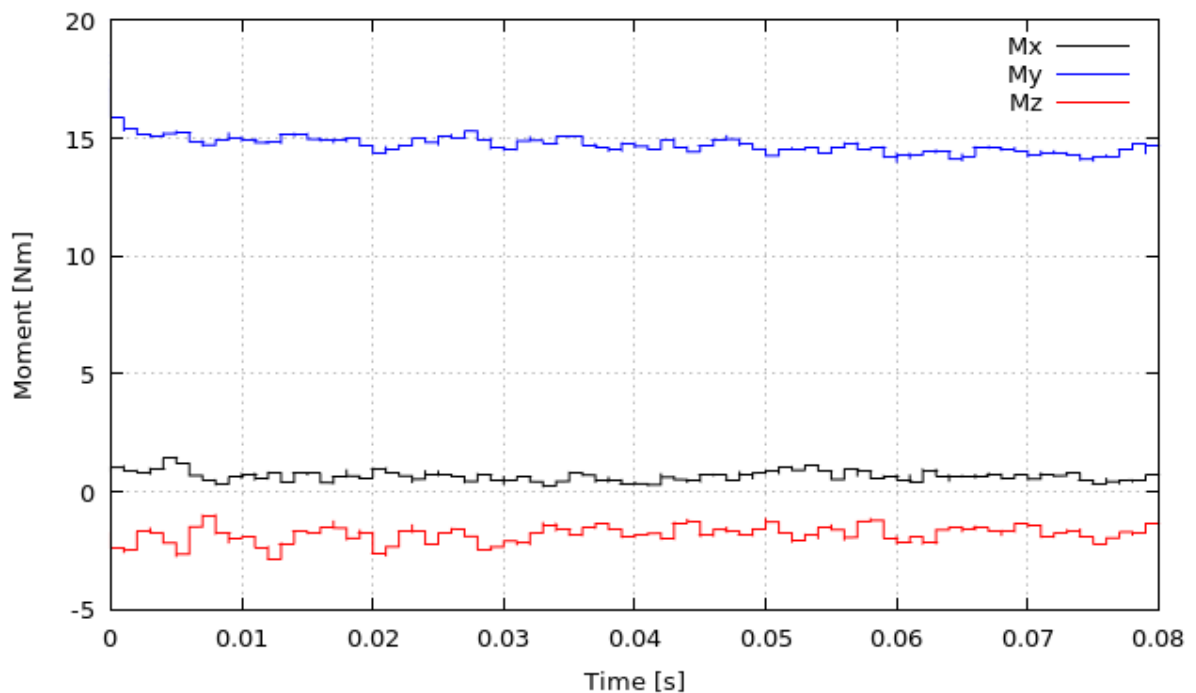
**Figure 5.7: Test D force convergence with LES turbulence model.**

The force value in the  $y$  axis direction has large oscillations that occur due to flow separation. The relative amplitude of oscillation of force  $F_y$  is 250 % with RANS turbulence model, while it is 33 % with LES turbulence model. Forces in  $z$  direction also have large oscillations. The relative amplitude of oscillation of force  $F_z$  is 20 % with RANS turbulence model, while it is 15 % with LES turbulence model.

Moment convergence for RANS turbulence model is shown on Figure 5.8, while moment convergence for LES turbulence model is shown on Figure 5.9. Since forces have a direct impact on the moment value, the moment value in RANS turbulence model is smaller than moment values from the LES turbulence model simulation. The coordinate system is placed in the center of the model with  $z = 0$  at the water level. The value of moment around  $y$  axis is dominant and the relative amplitude of oscillation is 4.5 % with RANS and 3.5 % with LES turbulence model. The moment values around the remaining two axes  $x$  and  $z$  have large oscillations because of flow separation. The RANS turbulence model showed 62.5 % while the LES turbulence model showed 54.5 % of relative amplitude of oscillation of moment  $M_x$ . The relative amplitude of oscillation of moment  $M_z$  is 66.7 % with RANS and 27.7 % with the LES turbulence model.



**Figure 5.8: Test D moment convergence with RANS turbulence model.**



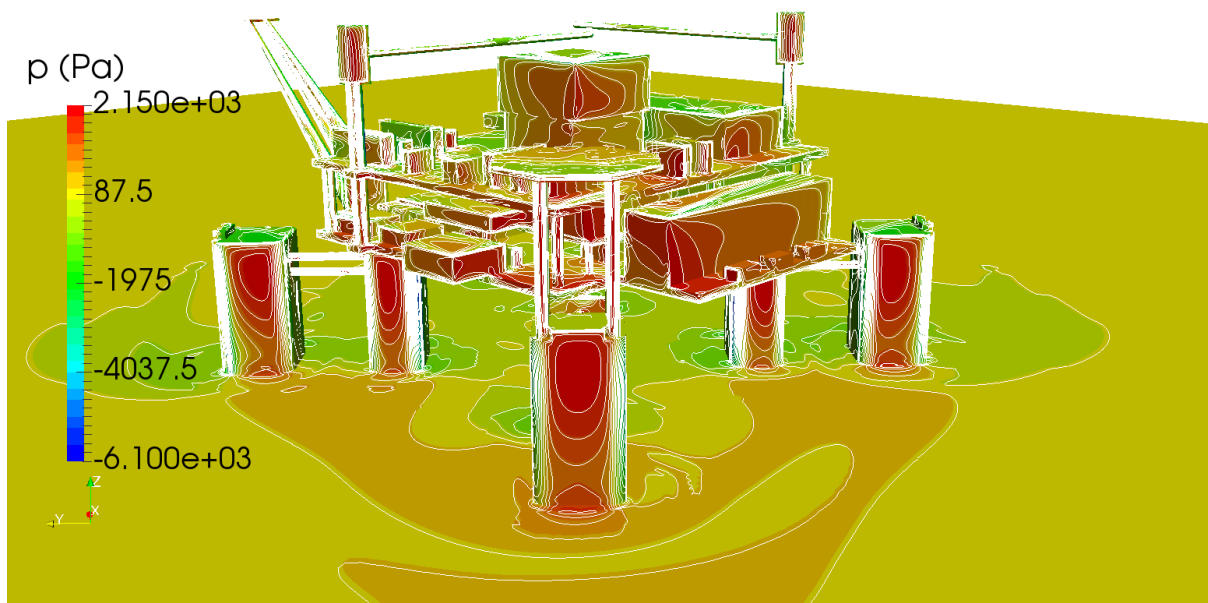
**Figure 5.9: Test D moment convergence with LES turbulence model.**

Table 5.3 presents the values of forces and moments obtained by the CFD analysis on Test D.

**Table 5.3: Test D forces and moments.**

<b>Turbulence model</b>	$F_x$ [N]	$F_y$ [N]	$F_z$ [N]	$M_x$ [Nm]	$M_y$ [Nm]	$M_z$ [Nm]
RANS	$132 \pm 4$	$2 \pm 5$	$16 \pm 4$	$0.8 \pm 0.5$	$13.2 \pm 0.4$	$-1.5 \pm 1$
LES	$139.5 \pm 2$	$6 \pm 2$	$20 \pm 3$	$0.55 \pm 0.3$	$14.5 \pm 0.5$	$-1.8 \pm 0.5$

On Figure 5.10 the pressure distribution on the model for the RANS turbulence model is shown. The highest pressures appears on the upwind surfaces. The distribution of pressure for cubic model is shown in Section 3.3 where it is shown that the highest pressure is expected at 85% of model height. If we look at the first upwind column that does not have any additional front parts that would affect its pressure distribution, it is apparent that the highest pressure is at approximately 75 – 85% of the pillar height. Figure 5.11 shows model pressure distribution for Test D with LES turbulence model.

**Figure 5.10: Model pressure distribution for Test D with RANS turbulence model.**

On Figure 5.12 and Figure 5.13 the pressure distribution contours are displayed at 85% column height. It can be seen that higher pressure appears with the LES turbulent model, which ultimately results in greater forces and moments.

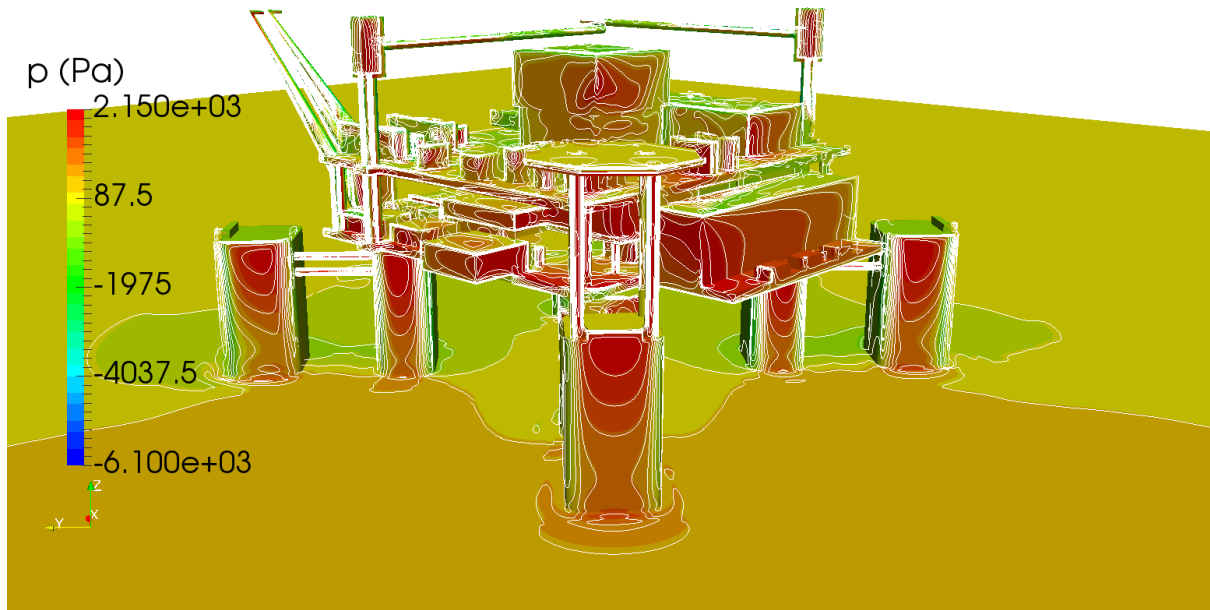


**Figure 5.11: Model pressure distribution for Test D with LES turbulence model.**

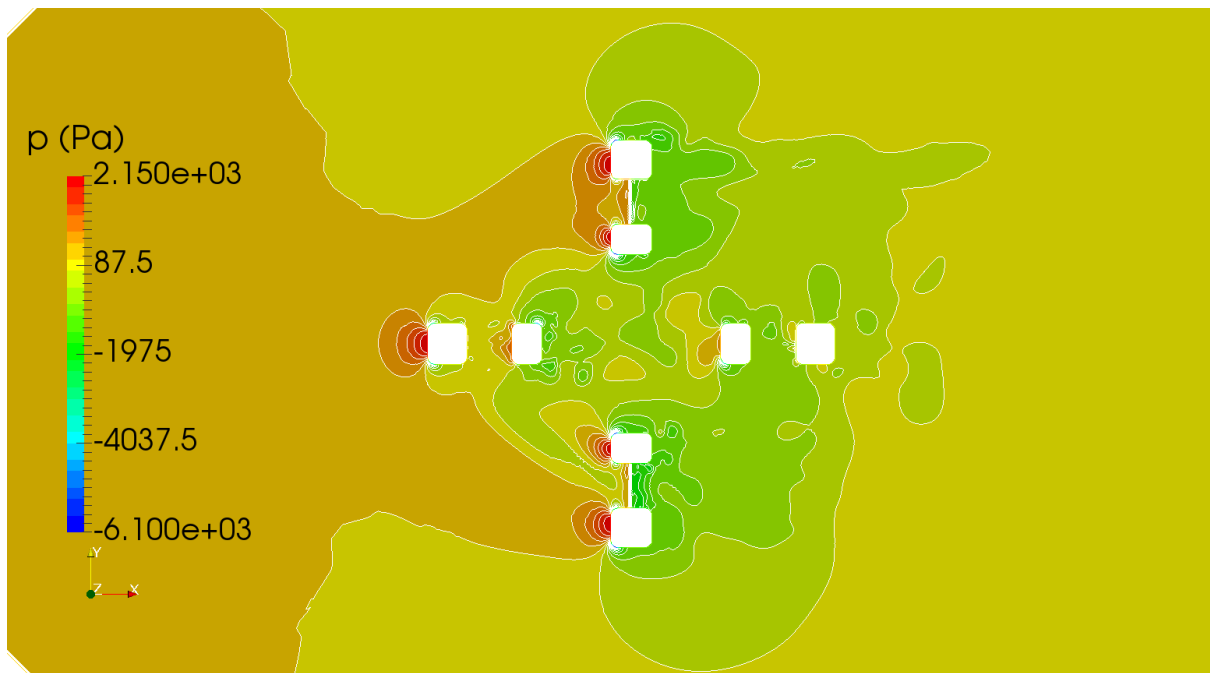


**Figure 5.12: Pressure distribution on plane  $z = 0.085\text{m}$  for RANS turbulence model.**

In order to explain the diagrams in Figure 5.15a - Figure 5.15f more easily, Figure 5.14 shows six different lines on the model where the data is taken from.

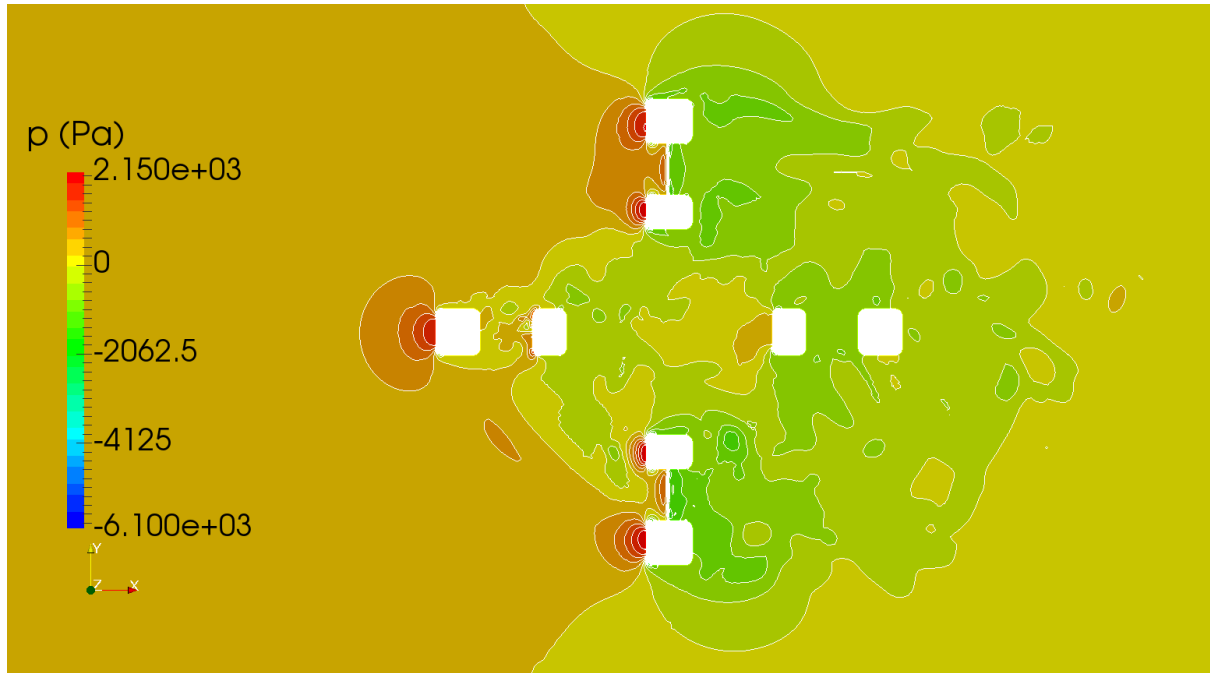


**Figure 5.13: Pressure distribution on plane  $z = 0.085\text{m}$  for LES turbulence model.**

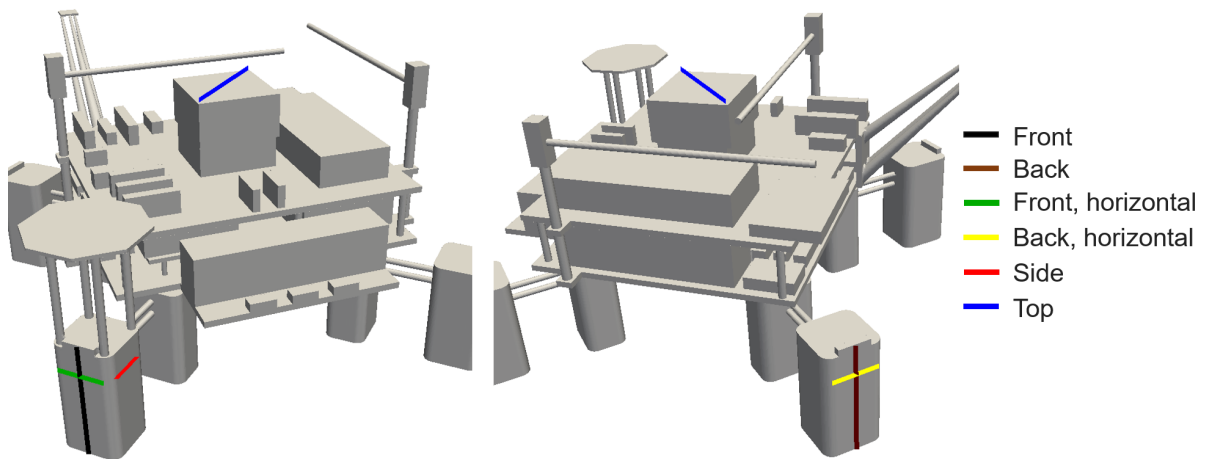


**Figure 5.14: Lines pressure distribution for Test D.**

The pressure distribution shown in Figure 5.15a and Figure 5.15c best matches the pressure distribution shown on figure C. Because of the rounded edges of the pillars, separation occurs on the front surface which results in a sudden drop in pressure as seen on Figure 5.15e. The same kind of behavior is observed on top faces which is shown on Figure 5.15f. Due to the environment influencing the flow there is a premature flow separation and vortex generation which plays a significant role in the LES turbulence model. Figure 5.15b and Figure 5.15d are taken from behind the last pillar. Comparing RANS and LES turbulence model, RANS simulations have smoother pressure distribution.

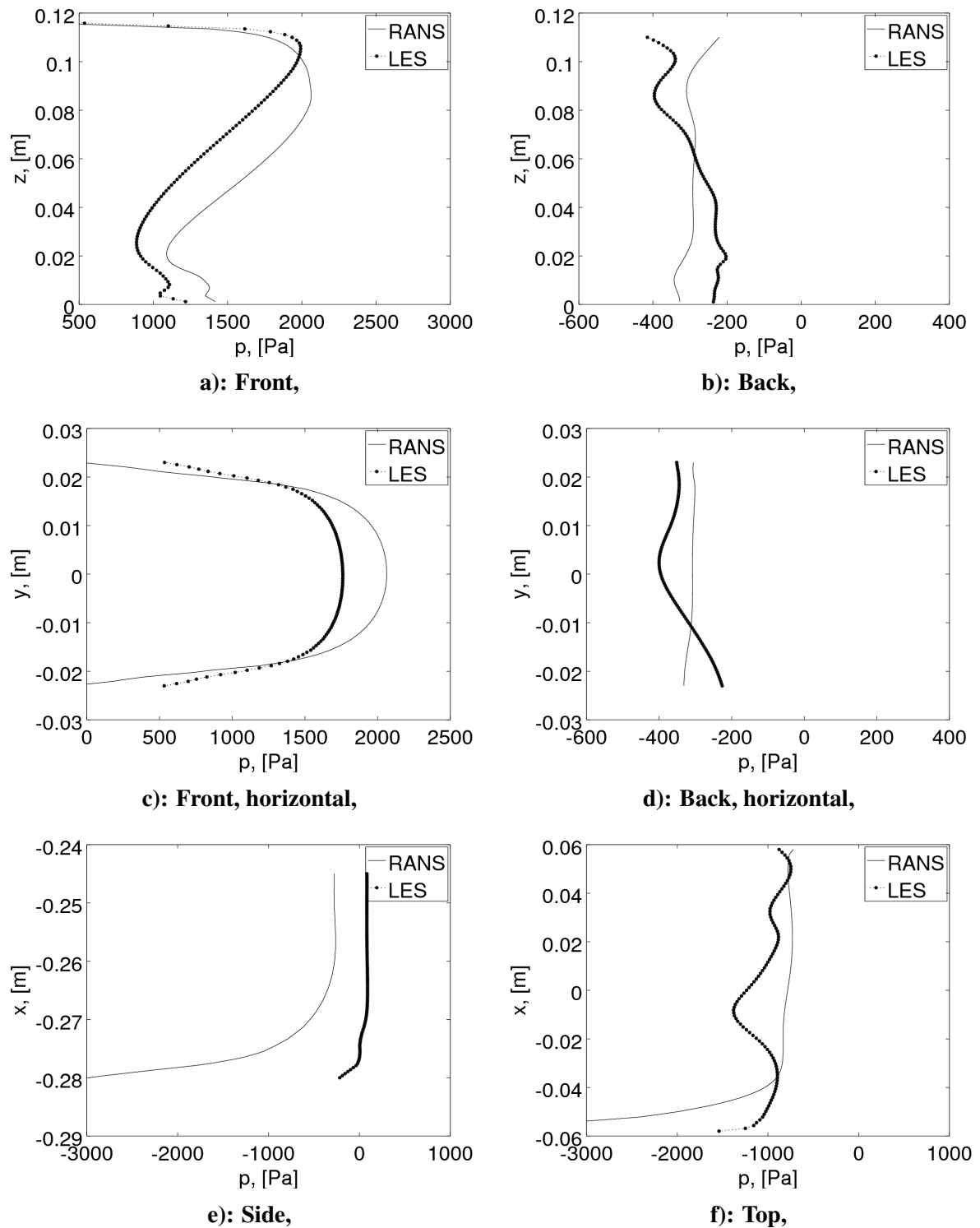


**Figure 5.15: Pressure distribution on different faces for Test D.**

Figure 5.16 and Figure 5.17 show pressure distribution and velocity vectors on planes with  $y = 0$  and  $z = 0$ . It was expected that the highest pressures would occur at "stagnation points" where the velocity value is equal to 0.

Velocity distribution and velocity vectors are shown on Figure 5.18 and Figure 5.19.

Figure 5.20 and Figure 5.21 shows velocity vectors on plane  $y = 0$  and at 85% column height. At this height, the greatest pressure appears. Also, the picture shows the vortices caused by the flow separation from the model.

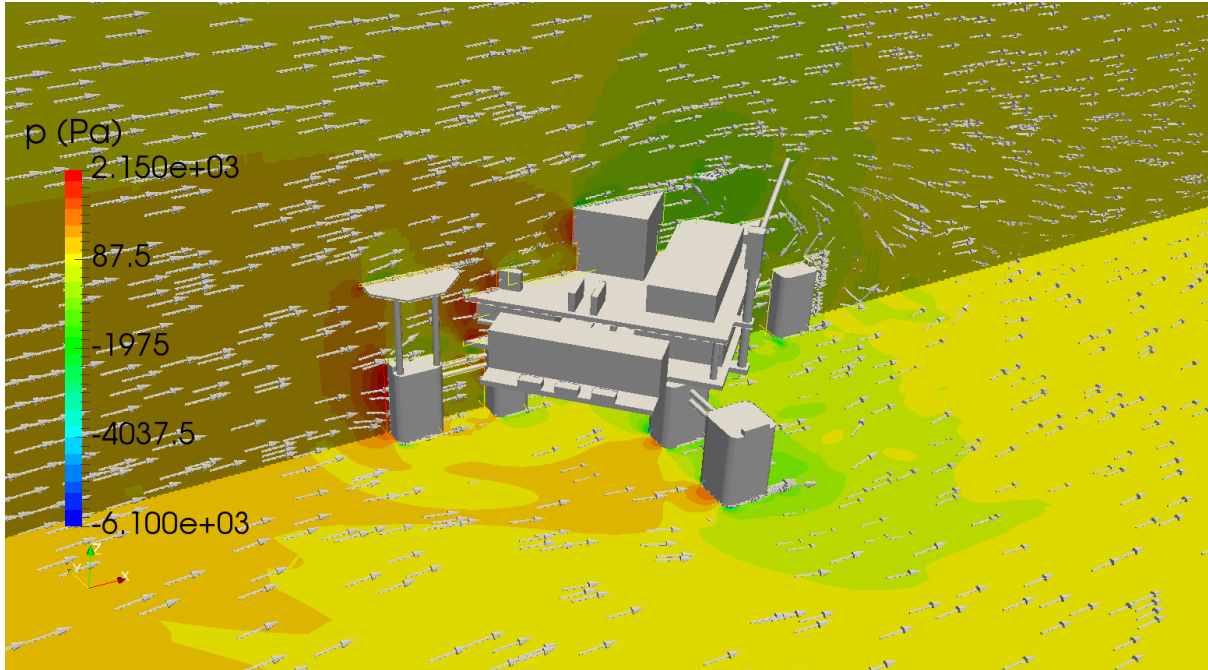


Figure 5.16: Pressure distribution for Test D with RANS turbulence model.

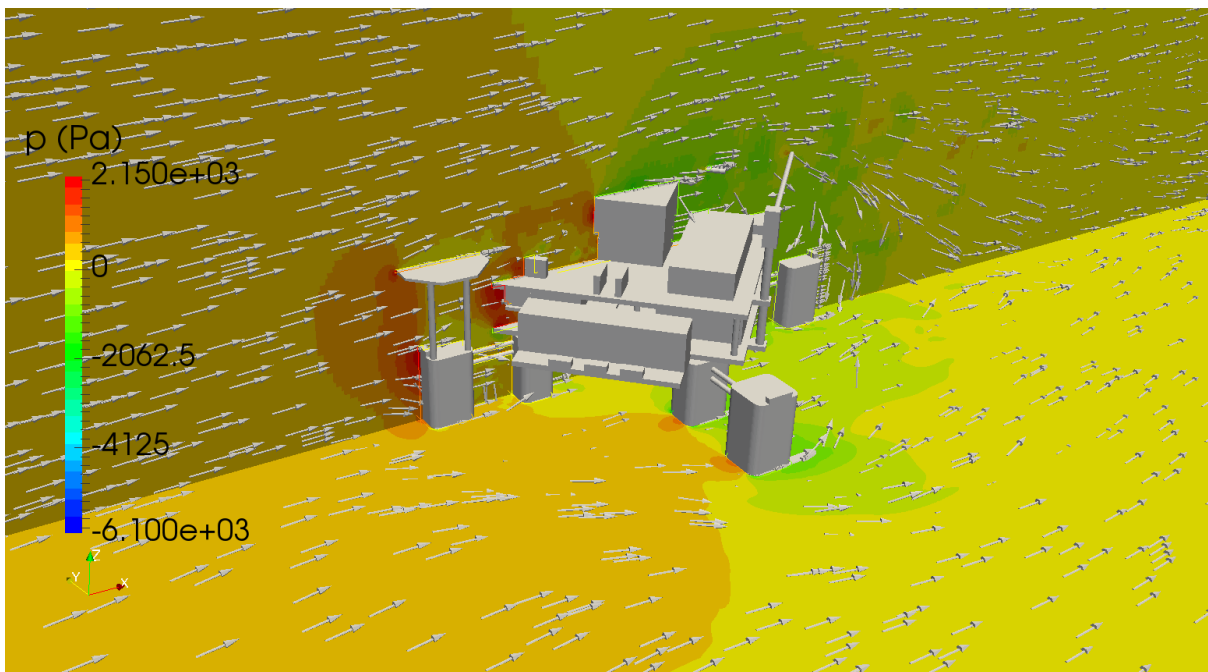
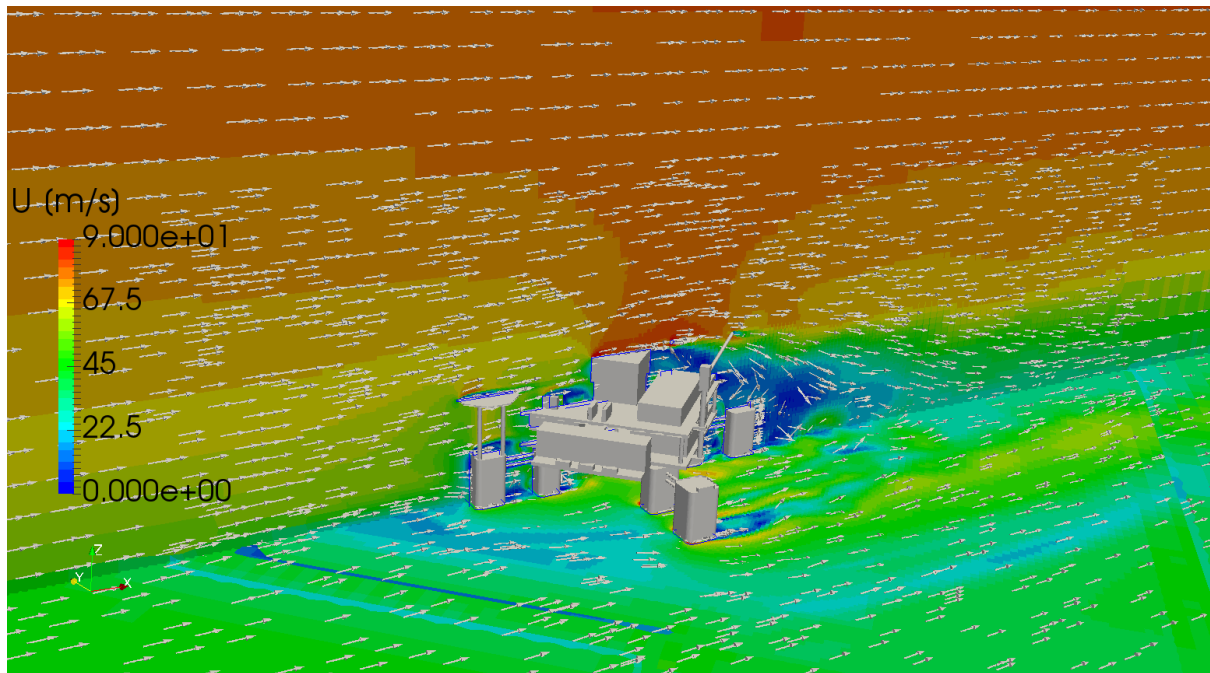
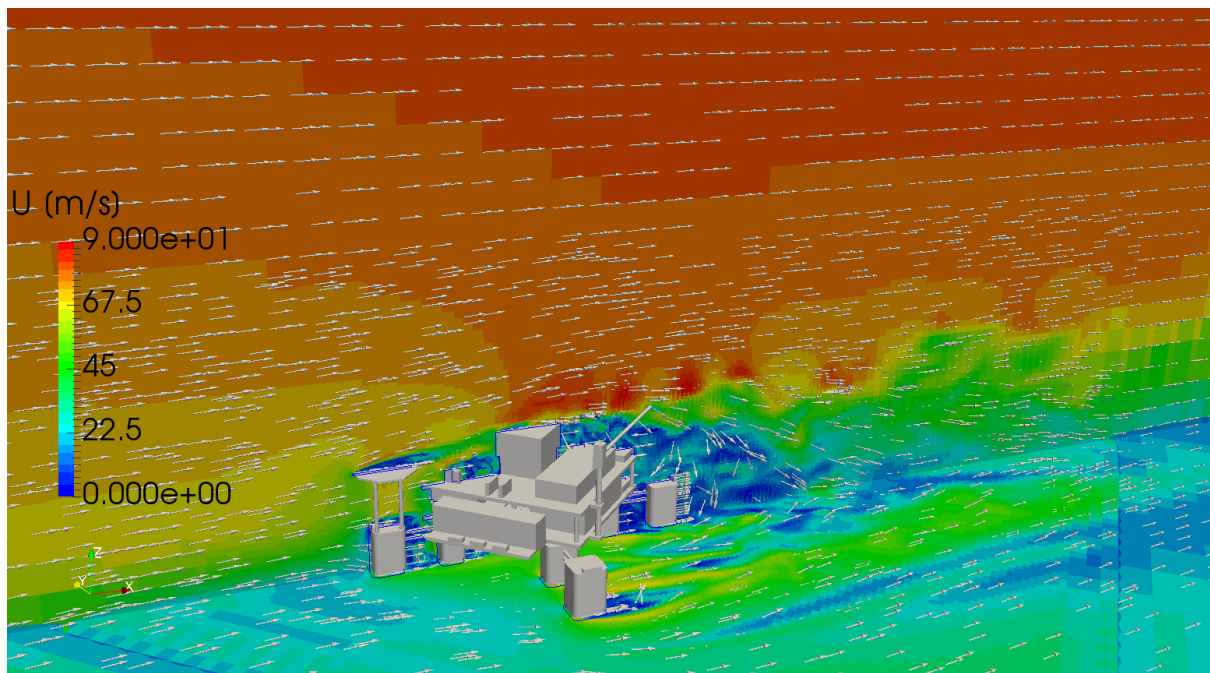


Figure 5.17: Pressure distribution for Test D with LES turbulence model.





**Figure 5.18: Velocity distribution for Test D with RANS turbulence model.**



**Figure 5.19: Velocity distribution for Test D with LES turbulence model.**

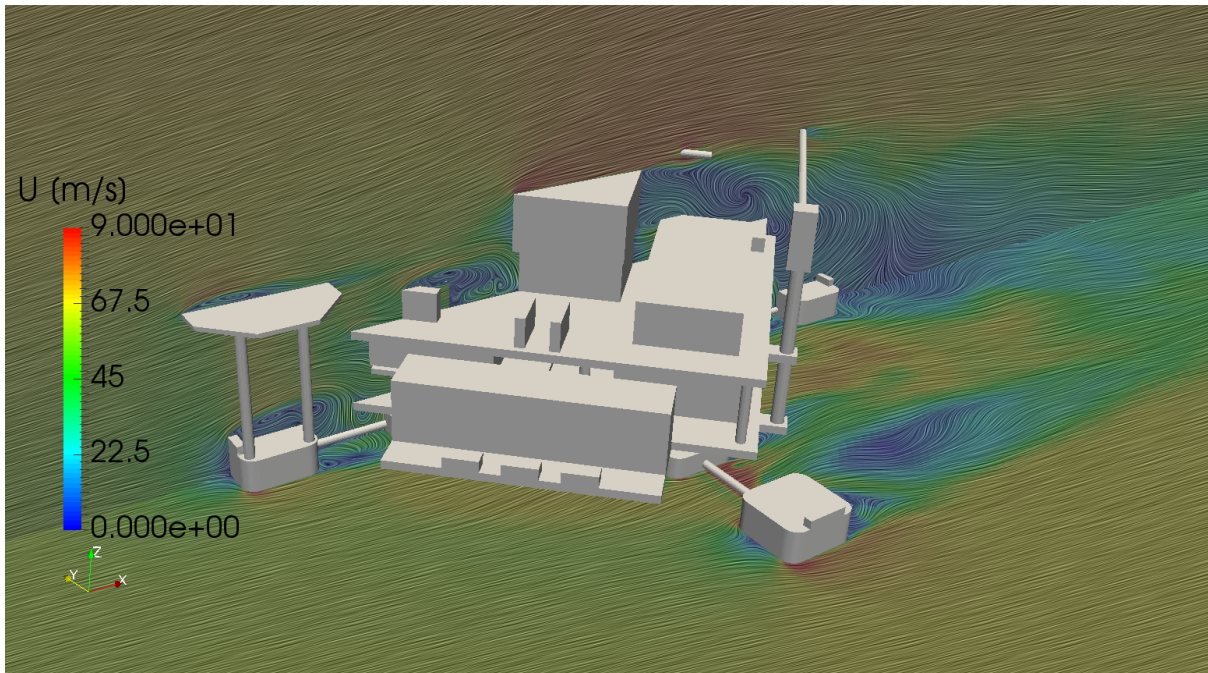


**Figure 5.20: Velocity streamlines at 85% column height for Test D with RANS turbulence model.**

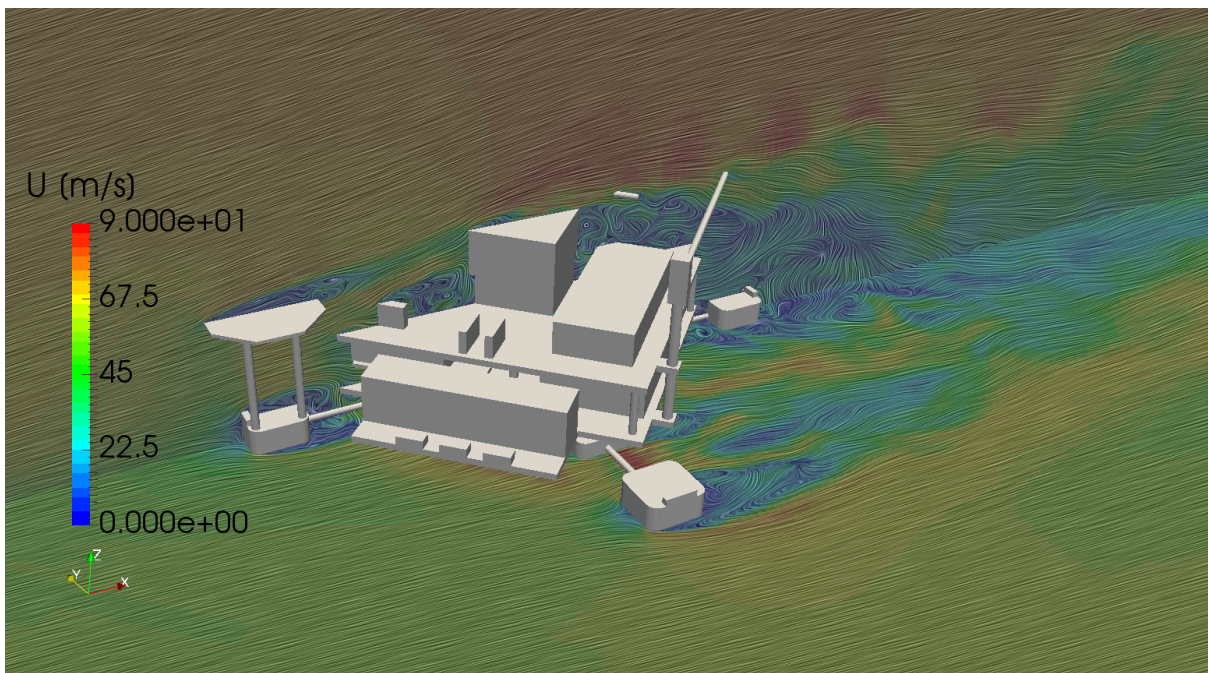


**Figure 5.21: Velocity streamlines at 85% column height for Test D with LES turbulence model.**

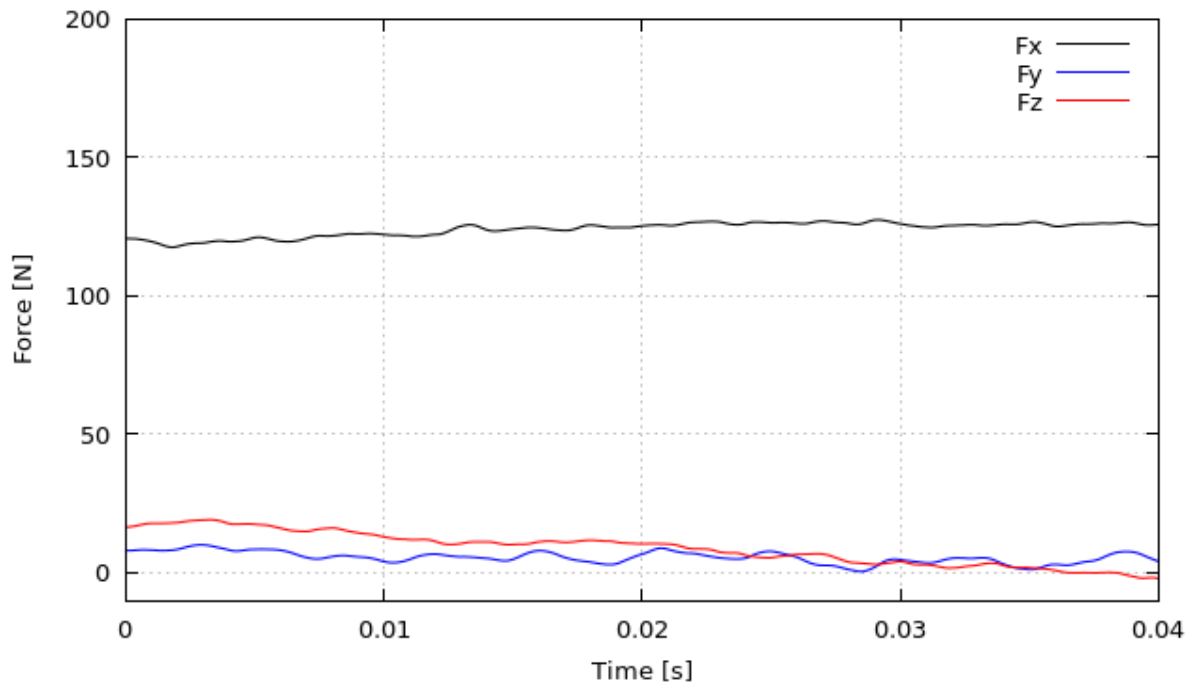
## 5.6 Test J results

This section presents the results of the simulation for stripped HOE PC-Semi submersible platform model Test J for the two turbulence models. As mentioned above, Test J is a stripped model with a removed derrick, flare boom, crane 1, living quarters and a helideck. All forces and moments values are reported in wind coordinate system, which is the global coordinate system. Body fixed coordinate system is rotated by 135 degrees with respect to the wind coordinate system.

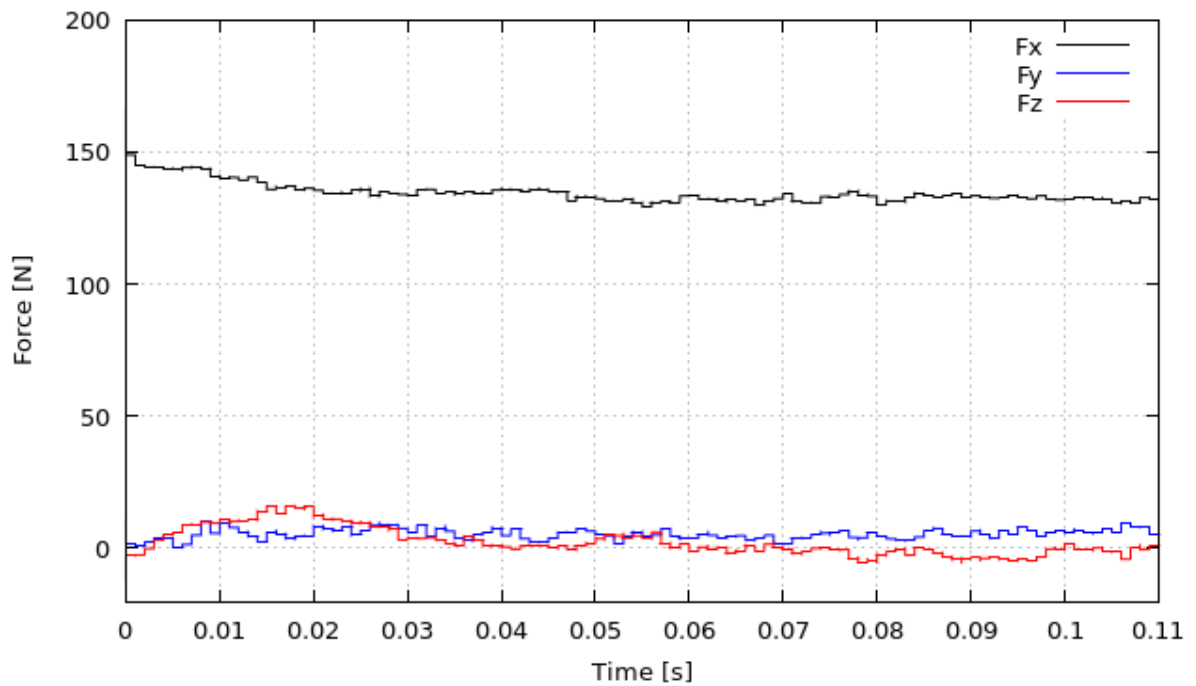
Figure 5.22 presents the graph of force convergence in dependence in time for unsteady solver with RANS turbulence model. Similar to Test D results, the force value in  $x$  direction is dominant and its oscillations have a major impact on the value of the total force that affects the model. Figure 5.23 shows the graph of the force convergence for LES turbulence model. Again the force values computed with LES turbulence model are higher than forces obtained with RANS turbulence model. In the simulation with RANS turbulence model, the relative amplitude of oscillation of force  $F_x$  is 1.6 %, while in the simulation with LES turbulence model the relative amplitude of oscillation is 1.5 %. Comparing to Test D, the force in the  $x$  direction for Test J has better convergence.

Force  $F_y$  with RANS turbulence model for Test J is smaller than for Test D and the relative amplitude of oscillation is 75%. The relative amplitude of oscillation of force  $F_y$  is 40% with LES turbulence model.

While comparing the force value in the  $z$  direction, in Test J values are smaller due to the removed helideck and relative amplitude of oscillation of force  $F_z$  is 100% with RANS turbulence model, while it is 200% with LES turbulence model.



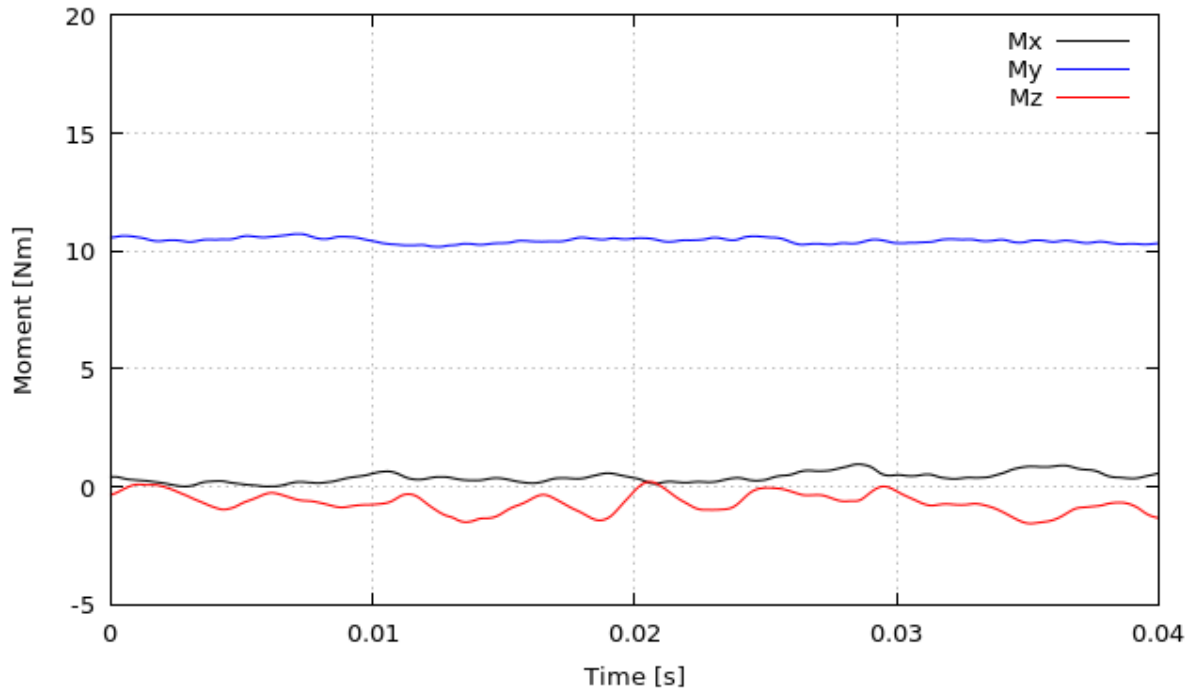
**Figure 5.22: Test J force convergence with RANS turbulence model.**



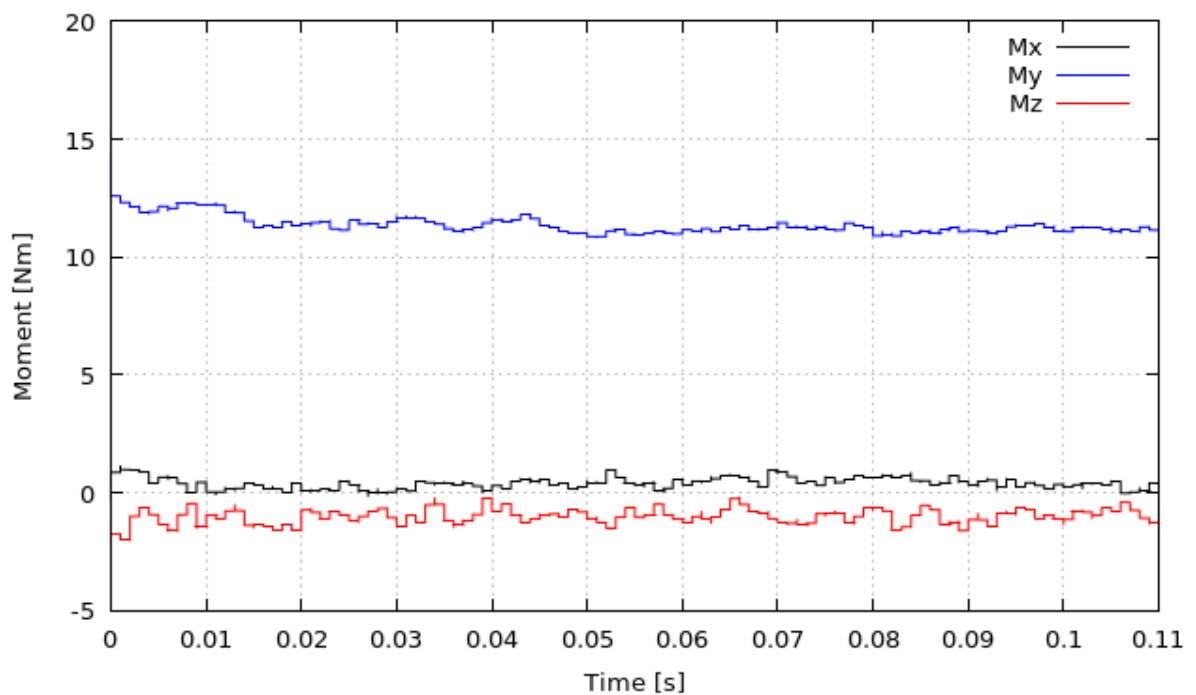
**Figure 5.23: Test J force convergence with LES turbulence model.**

The moment convergence for RANS turbulence model is shown on Figure 5.24 while the moment convergence for LES turbulence model is shown on Figure 5.25. The value of moment around y axis is dominant and the relative amplitude of oscillation is 1.9 % with RANS and 1.8 % with LES turbulence model. Those values are half as low as the values in Test D. The

moment values around the remaining two axes  $x$  and  $z$  have large oscillations because of flow separation. The RANS turbulence model showed 80 % while the LES turbulence model showed 100% of relative amplitude of oscillation of moment  $M_x$ . The relative amplitude of oscillation of moment  $M_z$  is 100 % with RANS and 50 % with LES turbulence model.



**Figure 5.24: Model pressure distribution for Test J with RANS turbulence model.**



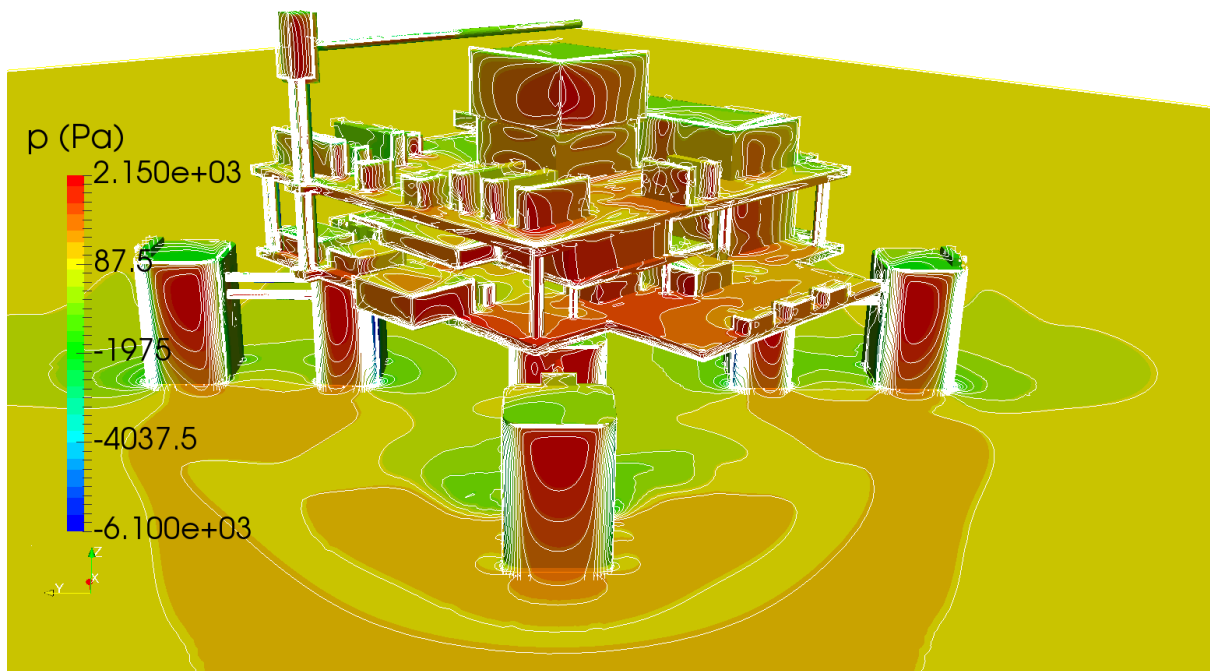
**Figure 5.25: Model pressure distribution for Test J with LES turbulence model.**

Table 5.3 presents the values of forces and moments obtained by the CFD analysis on Test D.

**Table 5.4: Test J forces and moments.**

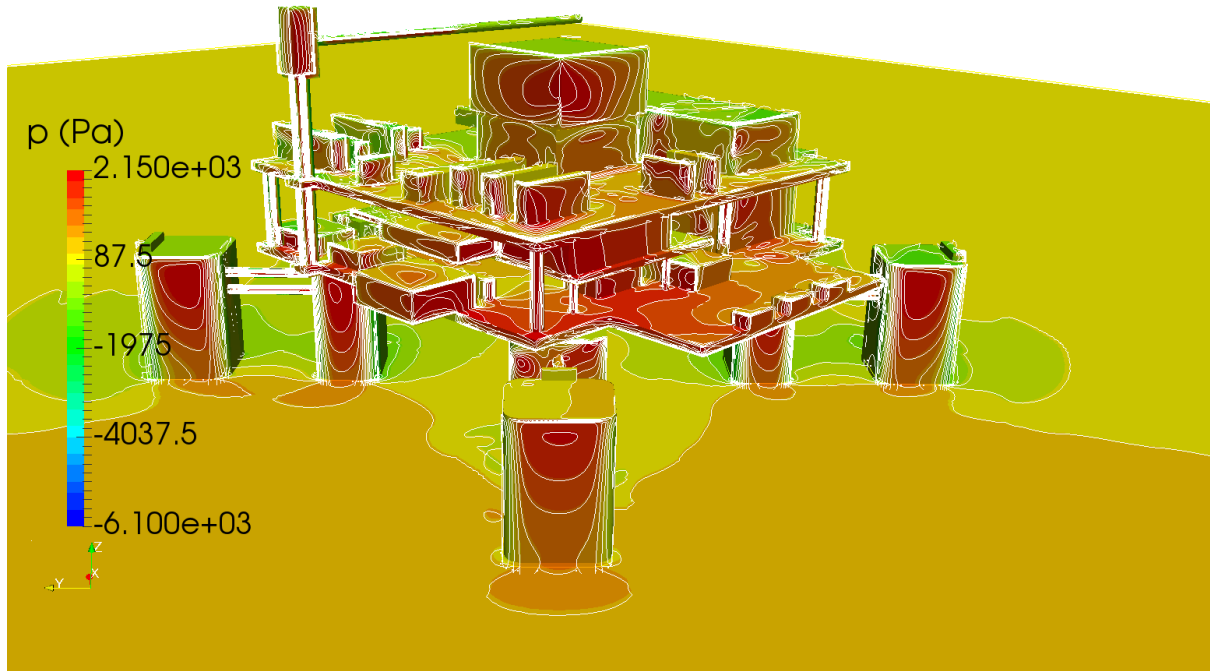
<b>Turbulence model</b>	$F_x$ [N]	$F_y$ [N]	$F_z$ [N]	$M_x$ [Nm]	$M_y$ [Nm]	$M_z$ [Nm]
RANS	$126 \pm 2$	$4 \pm 3$	$5 \pm 5$	$0.5 \pm 0.4$	$10.4 \pm 0.2$	$-1 \pm 1$
LES	$132.5 \pm 2$	$5 \pm 2$	$0 \pm 5$	$0.5 \pm 0.5$	$11.2 \pm 0.2$	$-1 \pm 0.5$

Figure 5.26 and Figure 5.27 present pressure distribution on the model for the different turbulence models. Comparing Test D with Test J it is apparent that the pressure distribution is similar.

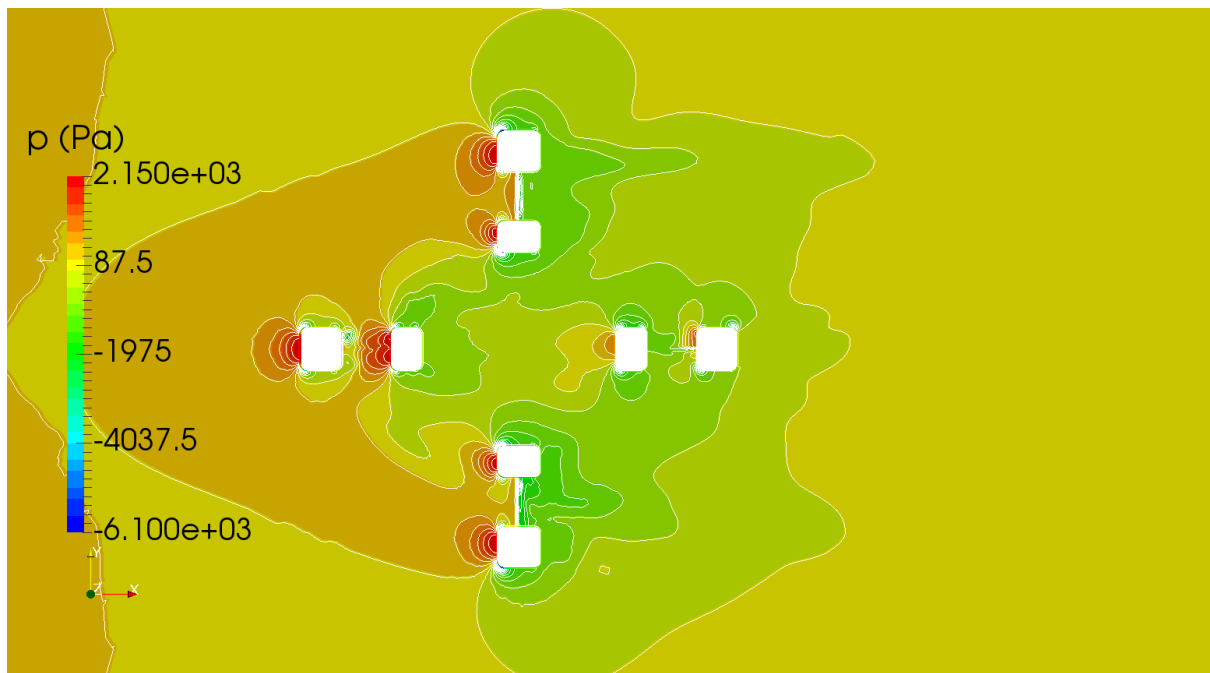


**Figure 5.26: Pressure distribution on model for Test J with RANS turbulence model.**

On Figure 5.28 and Figure 5.29 the pressure distribution contours are displayed at 85% column height. It can be seen that higher pressures appear in the LES turbulence model, which ultimately results in greater forces and moments.

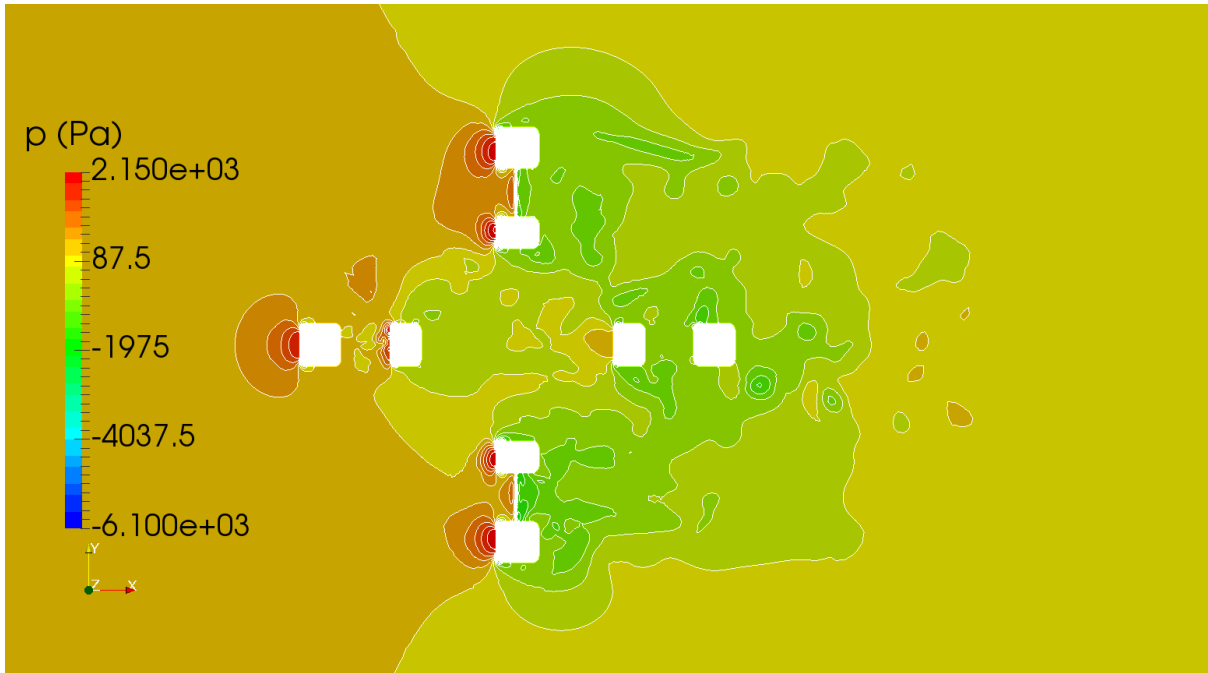


**Figure 5.27: Pressure distribution on model for Test J with LES turbulence model.**

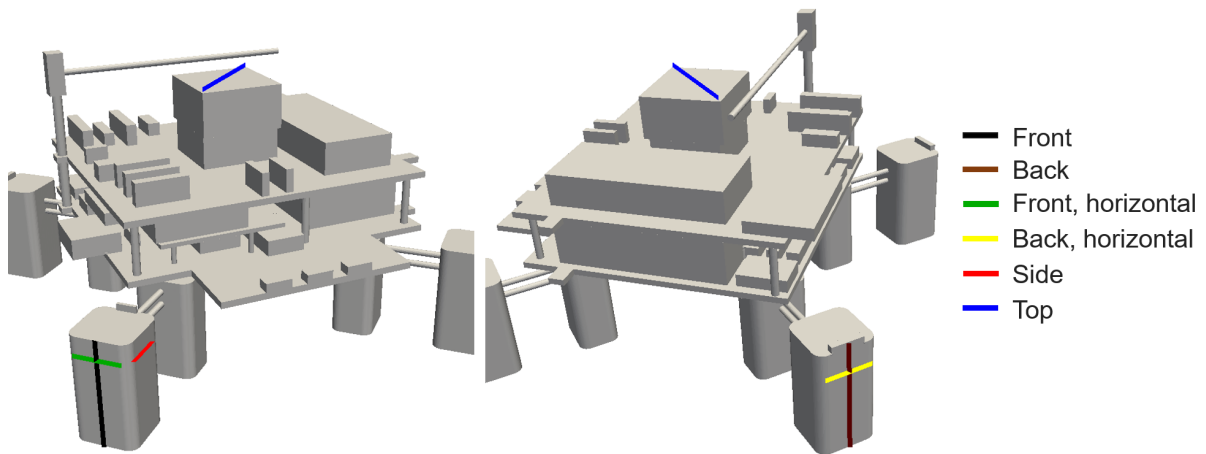


**Figure 5.28: Pressure distribution on plane  $z = 0.085\text{m}$  with RANS turbulence model.**

In order to more easily explain the diagrams in Figure 5.31a - Figure 5.31f, in picture Figure 5.30 are shown six different lines on the model where the data is taken from. The lines are situated in the same place like in Test D.



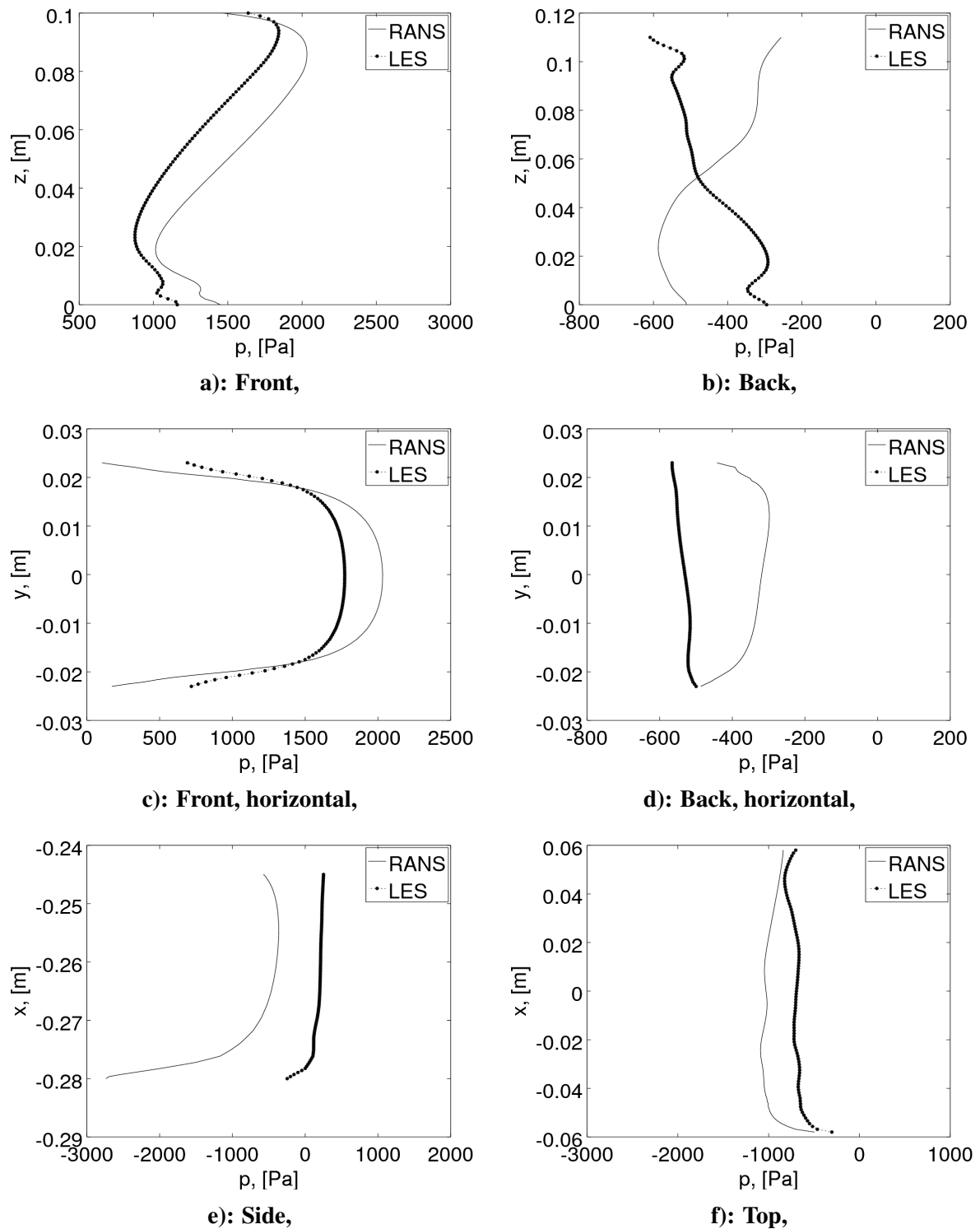
**Figure 5.29: Pressure distribution on plane  $z = 0.085\text{m}$  with LES turbulence model.**



**Figure 5.30: Lines pressure distribution for Test J.**

Comparing the pressure distribution between Test D and Test J there are no major differences except that due to the removed parts there is smoother distribution on the top surface and the pressure on the back surfaces is lower.





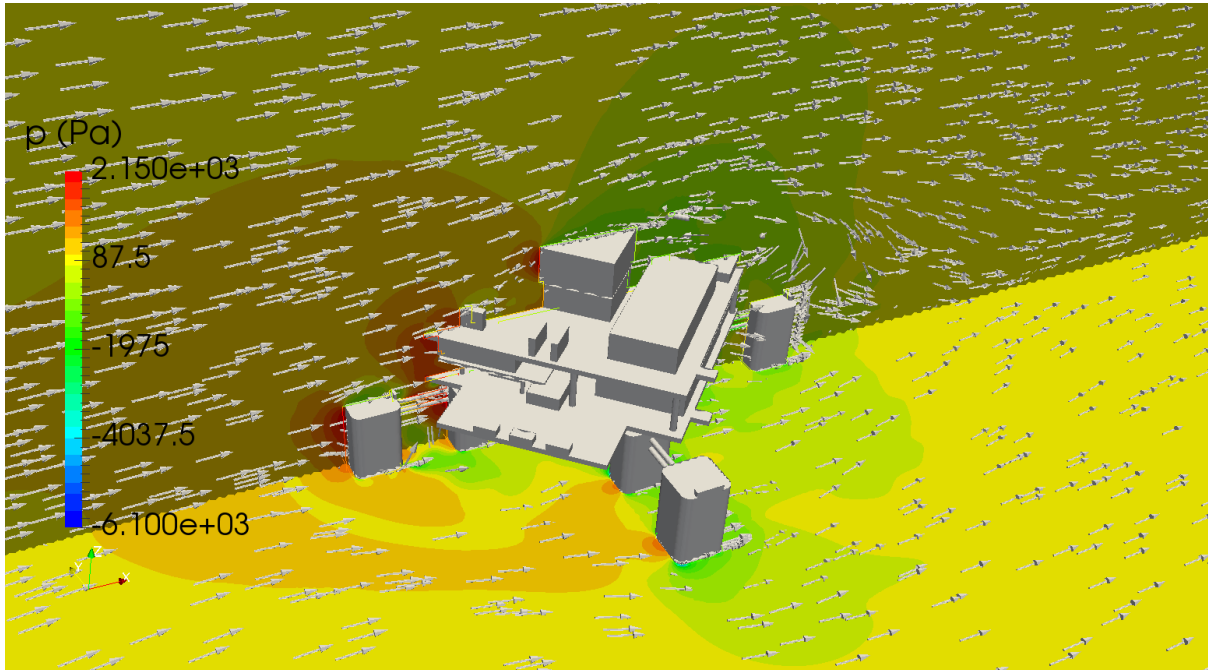
**Figure 5.31: Pressure distribution on different faces for Test J.**

Figure 5.32 and Figure 5.33 show pressure distribution and velocity vectors on planes with  $y = 0$  and  $z = 0$ . It was expected that the highest pressures would occur at "stagnation points" where the velocity value is equal to 0.

Velocity distribution and velocity vectors are shown on Figure 5.34 and Figure 5.35. Results

are taken on plane slice with  $y = 0$  and  $z = 0$ .

Figure 5.36 and Figure 5.37 show velocity streamlines on plane  $y = 0$  and at 85% column height. At this height, the highest pressure appears. Also, the picture shows the vortices caused by the flow separation from the model.



**Figure 5.32: Pressure distribution for Test J with RANS turbulence model.**

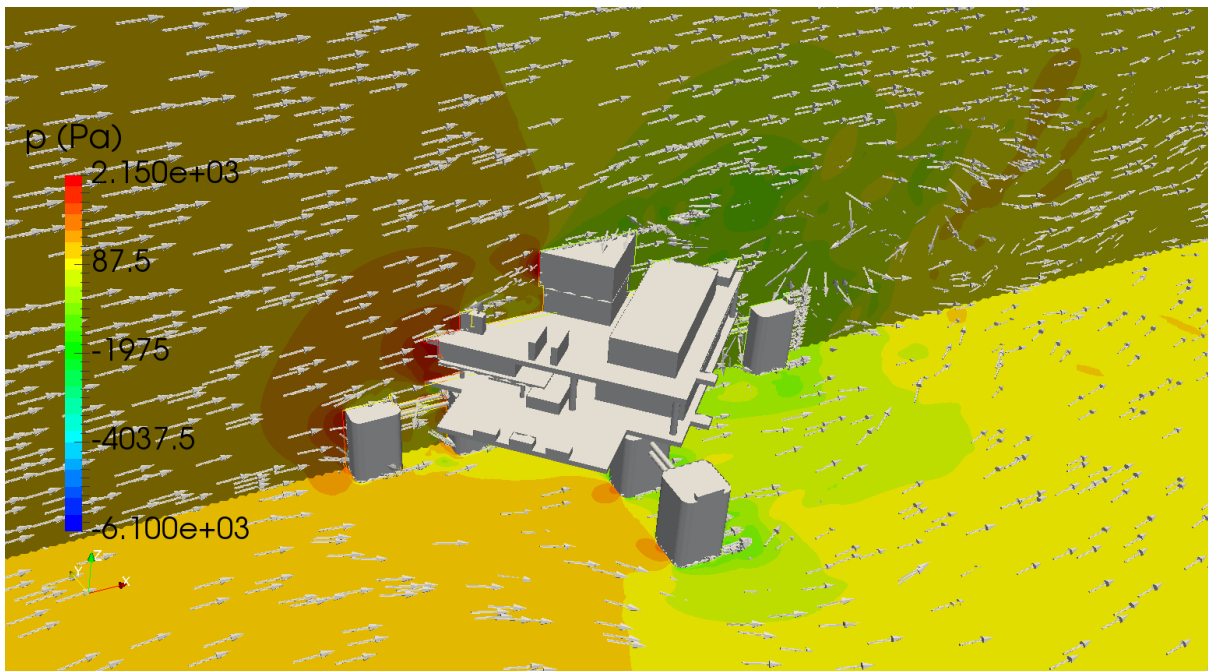


**Figure 5.33: Pressure distribution for Test J with LES turbulence model.**

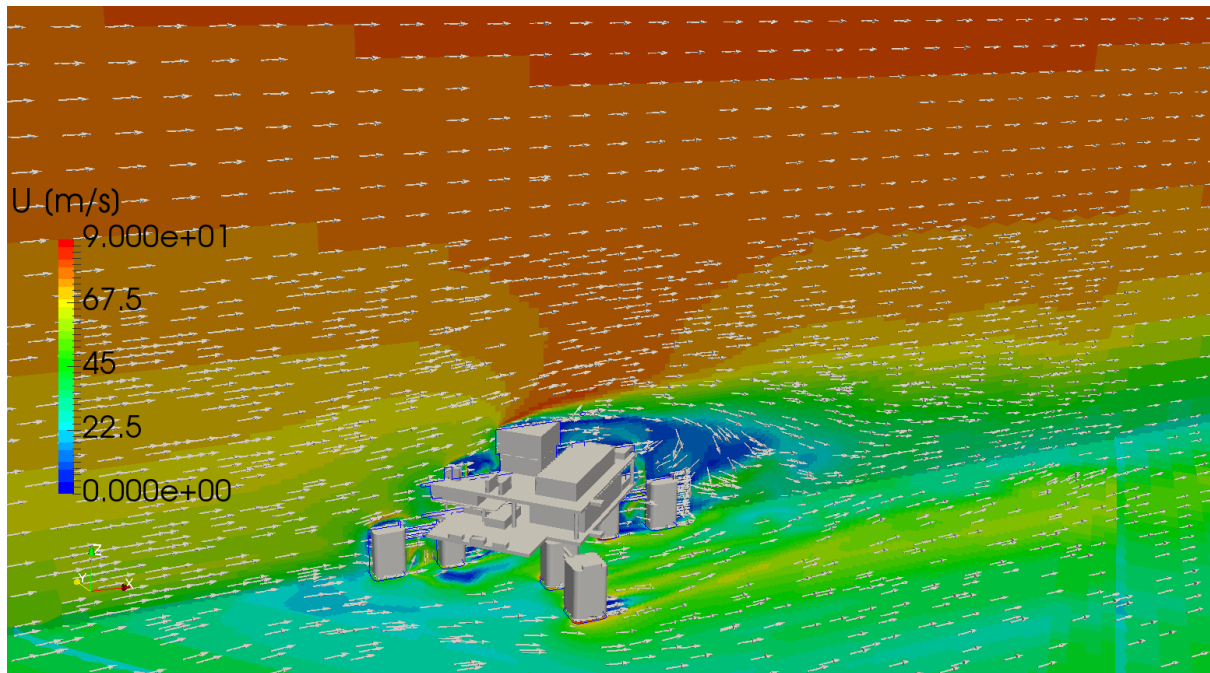


**Figure 5.34: Velocity distribution for Test J with RANS turbulence model.**

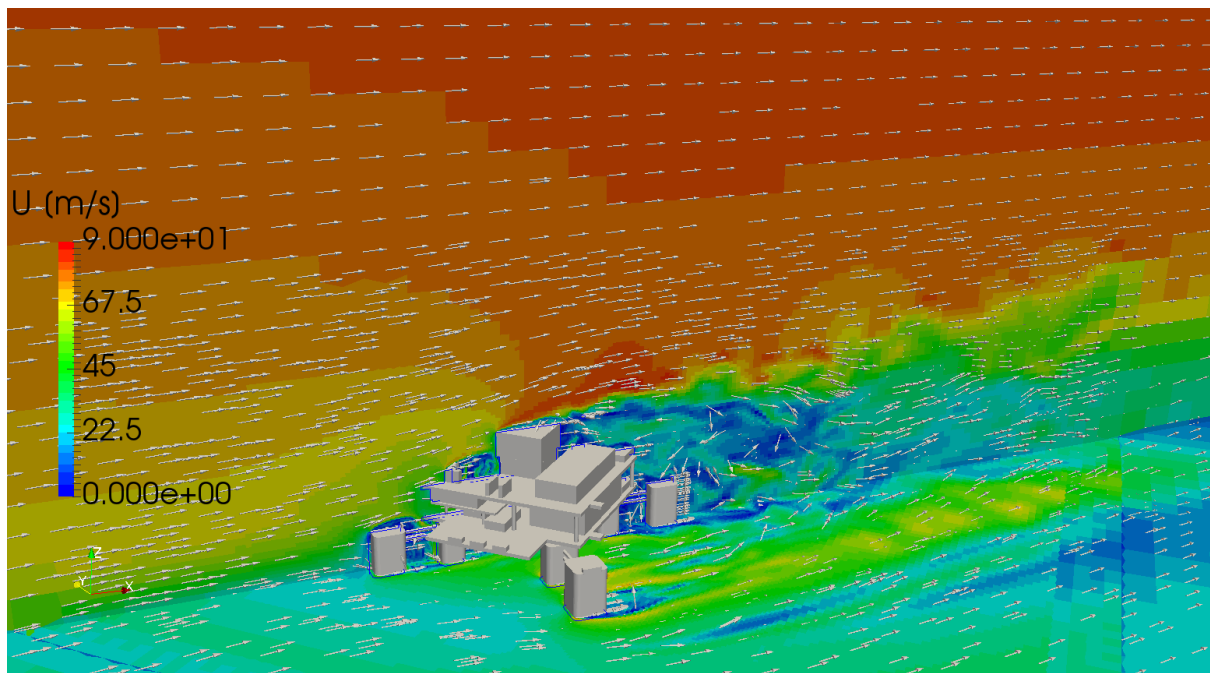


**Figure 5.35: Velocity distribution for Test J with LES turbulence model.**

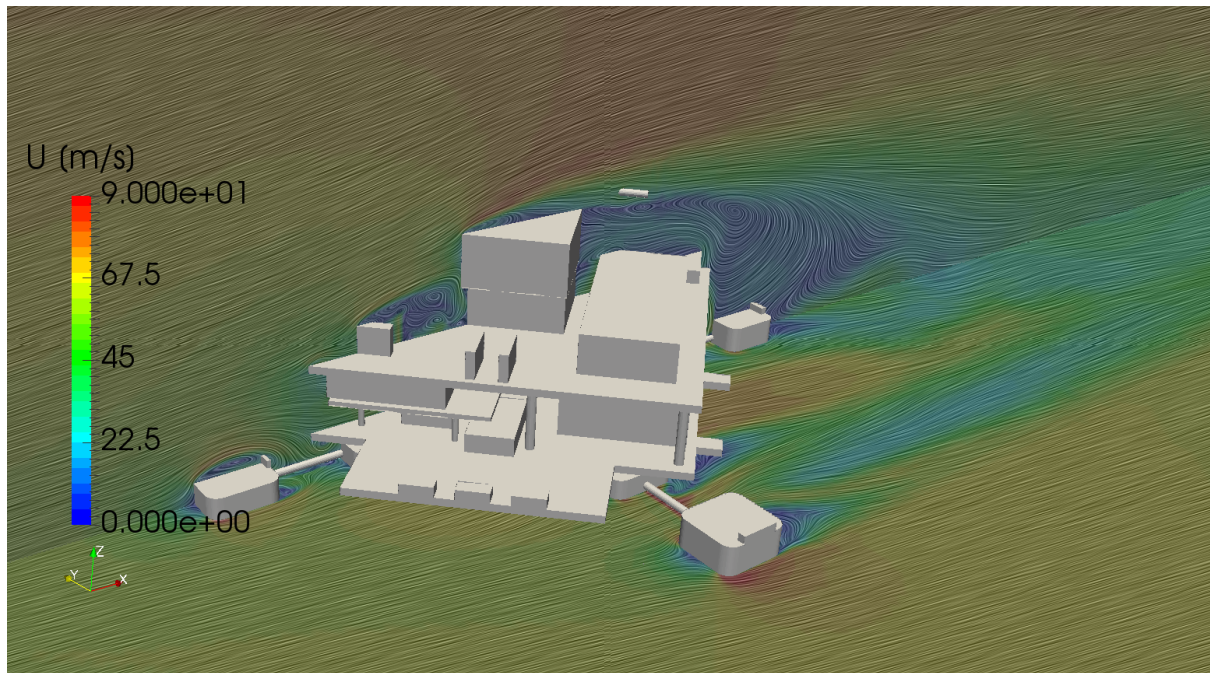


**Figure 5.36:** Velocity streamlines at 85% column height for Test J with RANS turbulence model.

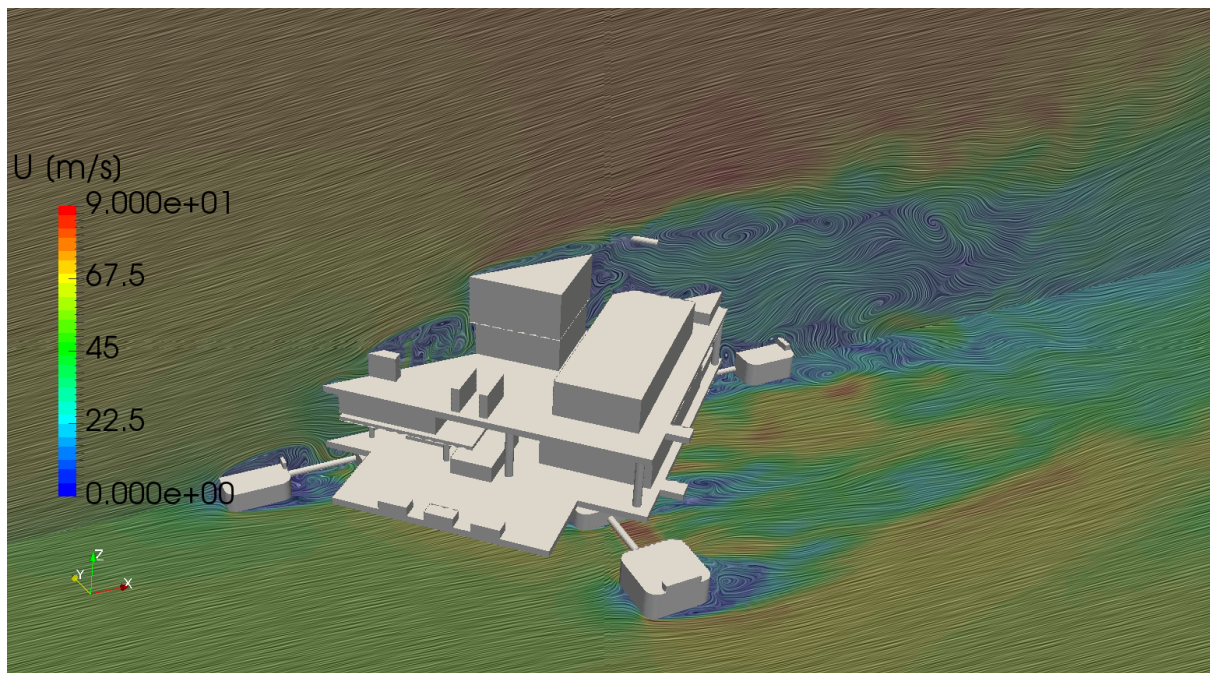
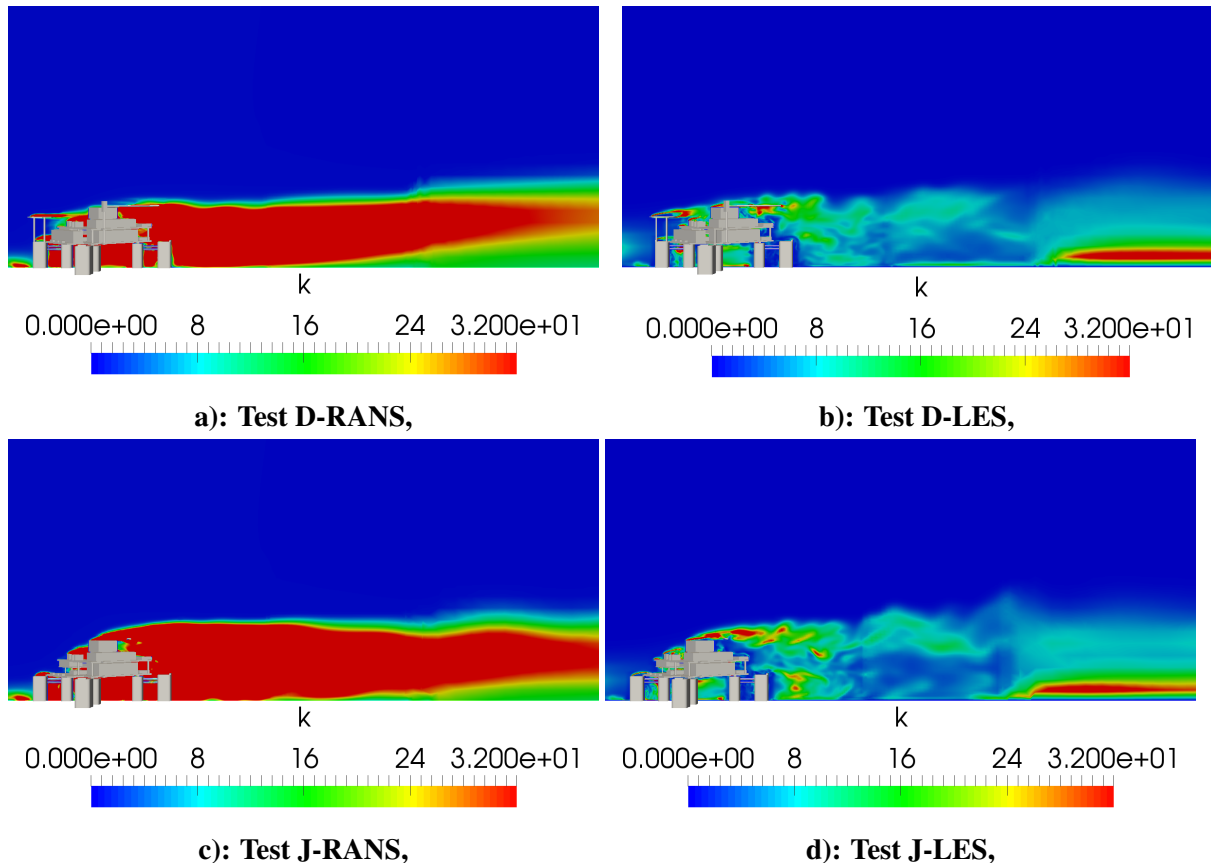


**Figure 5.37:** Velocity streamlines at 85% column height for Test J with LES turbulence model.

## 5.7 Comparison of Test D and Test J results

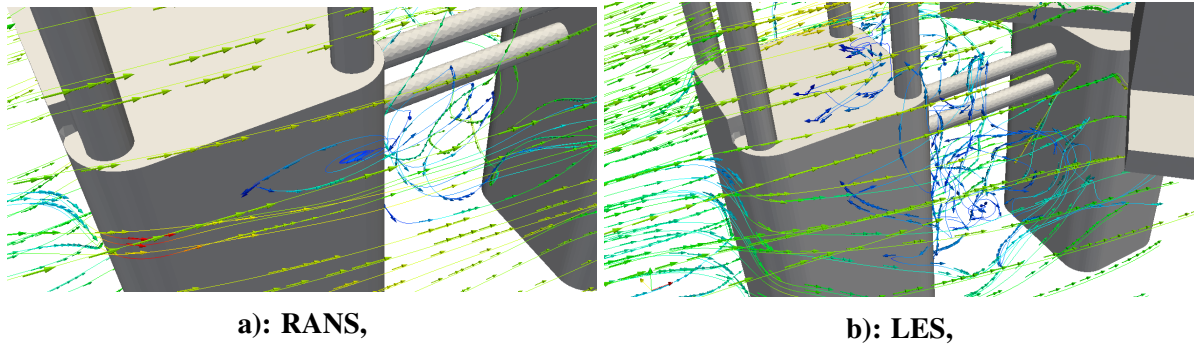
This section shows the comparison of all cases specific values such as turbulent kinetic energy and flow separation. Unlike previous cases, comparing here the Test D and Test J, it is obvious that removing certain parts increases the turbulence intensity.

Figure 5.38 presents turbulent kinetic energy for both turbulence models. It is apparent that there is more turbulence in Test J and the reason is that there is no helideck that in some sense focuses the flow before it has reached the part from which it is separated.



**Figure 5.38: Turbulent kinetic energy.**

Figure 5.39 - Figure 5.41 shows flow separation on different parts of model visualised by streamlines and velocity vectors. Figure 5.39 presents flow separation obtained on front pillar and it is visible that LES turbulence model produces more vortices. The same kind of behavior is visible on Figure 5.40 that shows the flow around flare boom. Figure 5.41 shows flow separation on front pillar in Test J. It seems that the flow is much calmer than in Test D.



**Figure 5.39: Flow separation at the front pillar - Test D.**

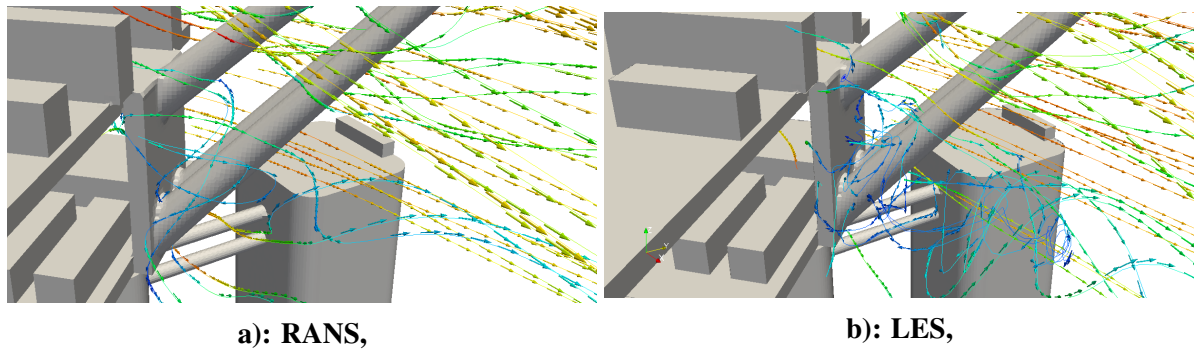


**Figure 5.40: Flow separation at the flare boom - Test D.**

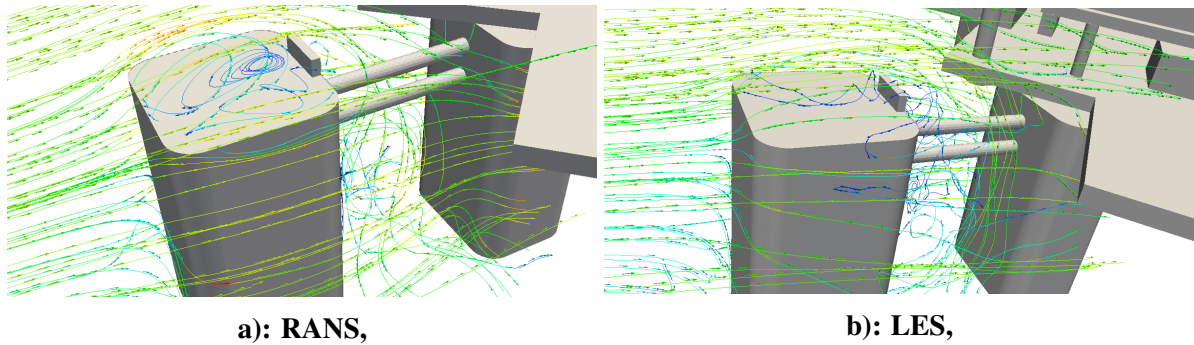


**Figure 5.41: Flow separation on front pillar - Test J.**

Since the computational grid is large, the simulation runs for several days, depending on computer resources. The information about simulation time and computational resources used for simulations can be found in Table 5.5 - Table 5.8.

**Table 5.5: Hardware and simulation time for Test D with RANS turbulence model.**

CPU	i7-6800K at 3.4 GHz
Number of Cores	4
RAM	64 GB DDR4
Time-step [s]	$2.5375 \cdot 10^{-6}$ s
Number of Iterations	38 809
Simulation Time [h]	357.9 hours

**Table 5.6: Hardware and simulation time for Test D with LES turbulence model.**

CPU	i5-4570K at 3.2 GHz
Number of Cores	4
RAM	32 GB DDR4
Time-step [s]	$2.9956 \cdot 10^{-6}$ s
Number of Iterations	26 842
Simulation Time [h]	621.2 hours

**Table 5.7: Hardware and simulation time for Test J with RANS turbulence model.**

CPU	i5-4570K at 3.2 GHz
Number of Cores	4
RAM	32 GB DDR4
Time-step [s]	$4.2965 \cdot 10^{-6}$ s
Number of Iterations	10 498
Simulation Time [h]	212.2 hours

**Table 5.8: Hardware and simulation time for Test J with LES turbulence model.**

CPU	i7-6800K at 3.4 GHz
Number of Cores	4
RAM	64 GB DDR4
Time-step [s]	$4.5549 \cdot 10^{-6}$ s
Number of Iterations	23 174
Simulation Time [h]	244.5 hours

## 5.8 Comparison with experimental results

This section presents the comparison between CFD (Test D and Test J) and experimental values obtained in the wind tunnel. Experimental data was presented at SNAME Maritime Convection, which was held on October 25, 2017 in Huston, TX, USA [13].

Forces and moments are normalized by dividing with dynamic pressure and presented in the following format:

$$C_F \cdot S = \frac{F_x}{q_{ref}} \quad (5.1)$$

$$C_M \cdot S \cdot L = \frac{M_y}{q_{ref}} \quad (5.2)$$

with  $q_{ref} = \frac{1}{2}\rho U_0^2$  being the reference dynamic pressure,  $S$  the projected area, and  $L$  the characteristic body length.  $C_F$  is coefficient which represents the drag force divided with dynamic pressure, while  $C_M$  represents the pitching moment divided with dynamic pressure. It is noted that this data reduction process does not require the definition of a reference area or reference length to calculate coefficients.

Table 5.9 shows the values of coefficient  $C_{F_{exp}}$  obtained experimentally in the wind tunnel and the values obtained by CFD analysis  $C_{F_{RANS}}$  and  $C_{F_{LES}}$ . The differences between experimental and simulations values are presented as well.

**Table 5.9: Force coefficient comparison.**

Model	Wind Tunnel	CFD RANS	CFD LES	RANS difference	LES difference
	$C_{F_{exp}}$	$C_{F_{RANS}}$	$C_{F_{LES}}$	$ \varepsilon_{C_{F_{RANS}}} [ \% ]$	$ \varepsilon_{C_{F_{LES}}} [ \% ]$
Test D	0.11097	$0.09426 \pm 0.003$	$0.09961 \pm 0.0015$	14.47%	9.61%
Test J	0.0764	$0.08997 \pm 0.0015$	$0.09462 \pm 0.0015$	17.77%	23.84%

Table 5.10 presents the values of coefficient  $C_{M_{exp}}$  obtained experimentally in the wind tunnel and the values obtained by CFD analysis,  $C_{M_{RANS}}$  and  $C_{M_{LES}}$ . The differences between experimental and simulations values are presented as well.

**Table 5.10: Moment coefficient comparison.**

Model	Wind Tunnel	CFD RANS	CFD LES	RANS difference	LES difference
	$C_{M_{exp}}$	$C_{M_{RANS}}$	$C_{M_{LES}}$	$ \varepsilon_{C_{M_{RANS}}} [ \% ]$	$ \varepsilon_{C_{M_{LES}}} [ \% ]$
Test D	0.00977	$0.00943 \pm 0.0003$	$0.01028 \pm 0.00036$	3.52%	5.24%
Test J	0.00697	$0.00074 \pm 0.00014$	$0.00079 \pm 0.00014$	6.55%	14.74%

## 5.9 Closure

The goal of this chapter was to present numerical results for for stripped HOE PC-Semi submersible platform models and compare them with experimental results obtained in the wind tunnel. Four different simulations were performed, for two different models and two different turbulence models. Results were presented in terms of pressure, velocity and



turbulence variables. Detailed pressure distributions were presented at 85% of pillar height where the highest pressure is expected. Pressure distribution on different sides of the pillar is also shown in comparison to the expected values.

Comparing the results with experimental values it can be seen that the values of force coefficients deviate much more from the experimental values than the moment coefficients. It is also noted that removing additional parts such as helideck and living quarters directly affects the flow and turbulence properties, and thus the amount of flow separation which ultimately results in greater deviation from the experimental values. The ABL deviation with LES turbulence model is larger than for the RANS turbulence model. If the mesh resolution is increased, this deviation would be smaller, which would also directly affect the values of forces and moments. If we compare the time needed for simulation convergence, LES turbulence model requires more time compared to RANS turbulence model.

## 6 Conclusion

This thesis presents the application of Finite Volume Method (FVM) based CFD software `foam-extend` on the wind load assessment of an offshore oil platform. Large time-step transient solver for incompressible, turbulent flow called `pimpleFoam` is used, which is based on PIMPLE algorithm.

Two different turbulence models are used and compared in this work, RANS and LES. Comparisons between RANS and LES turbulence models were performed on two oil platform models that differed with respect to the complexity of the model geometry. The results are also compared with experimental values obtained in the wind tunnel.

By comparing the results of ABL obtained from CFD simulations and the wind tunnel, better agreement is observed for RANS turbulence model. LES turbulence model has differences in the lower part of ABL due to the low mesh resolution. By increasing the mesh resolution, this deviation would be smaller which would also directly affect the values of forces and moments.

Values of forces and moments obtained from the simulations are compared with the experimental results. The differences for force and moment values are lower with RANS turbulence models, due to the better matching wind profile. On the other hand, the relative amplitude of oscillation for the forces and the moments is lower with LES turbulence model.

It is observed that removing additional parts such as helideck and living quarters directly affects the flow and turbulence properties, and thus the amount of flow separation. For example, by properly positioning helideck, the upper surface of helideck is directing the flow, and because of that, the parts that come behind the helideck do not have a sudden flow separation.

To sum up, better results with the LES turbulence model would be accomplished if the mesh resolution is increased, but it would also increase the computational time. Therefore, it is most important to choose a good compromise between computational time and the quality of the results depending on the problem.

Overall, the results show reasonable accuracy and high level of confidence. Comparable uncertainty between numerical and experimental results shows that similar precision can be expected in the study of the influence of wind on buildings and offshore objects. The application of CFD techniques to predict wind load on offshore objects reveals the suitability of CFD tools for preliminary assessments and detail examination of complex building aerodynamic characteristics.

## References

- [1] Voogt, A., “Overview of SNAME OC-8 Comparative Wind Load Study,” SNAME Maritime Convention in: Houston, TX, USA, 2017.
- [2] Jasak, H., “Numeričke metode u mehanici kontinuuma (Numerical Methods in Continuum Mechanics),” Material for lectures, 2016.
- [3] Maukalled F., Mangani L., Darwish M., “The Finite Volume Method in Computational Fluid Dynamics,” 2016.
- [4] Wilcox, D., Turbulence Modeling for CFD, 2006.
- [5] Menter, F. R., “Two-equation eddy-viscosity turbulence models for engineering applications,” 2006.
- [6] Kozmar, H., “Industrial Aerodynamics (Industrijska aerodinamika),” Material for lectures, 2017.
- [7] “foam-extend project,” <https://sourceforge.net/projects/foam-extend/>, last access 20.12.2017.
- [8] “Huston Offshore,” <http://www.houston-offshore.com/more-info-on-paired-column-semi/>, last access 27.12.2017.
- [9] van Wlree F., Willemsen E., “Wind Loads on Offshore Structures,” 1998.
- [10] “SolidWorks 2016,” <http://www.solidworks.com/>, 2016., last access 11.12.2017.
- [11] Juretić, F., “User Guide - cfMesh v1.1,” 2015.
- [12] Vukčević, V., “Application of computational fluid dynamics in the motion analysis of ships and offshore platforms,” Master’s Thesis, 2006.
- [13] Voogt, A., “Overall Data Comparison and Lessons Learned,” SNAME Maritime Convention in: Houston, TX, USA, 2017.
- [14] “CFD Online,” <https://www.cfd-online.com/>, last access 24.11.2017.
- [15] Jasak, H., “Error analysis and estimation for the Finite Volume Method with applications to fluid flows,” PhD Thesis, 1996.
- [16] “OpenFOAMWiki,” <http://openfoamwiki.net/index.php/Contrib/groovyBC>, last access 04.12.2017.
- [17] Tobias, H., “Mathematics, Numerics, Derivations and OpenFOAM,” Holzmann CFD, Leoben, fourth edition, 2016.